Eidgenössische Technische Hochschule Zürich
Swiss Federal Institute of Technology Zurich

Engineering ultrastrong coupling between a membrane and a transmon

Master's thesis

Yu Liu

yuliuy@ethz.ch

Hybrid Quantum Systems Group
ETH Zürich

Supervisors:
Prof. Dr. Yiwen Chu (HyQu)
Dr. Simon Storz (HyQu)

September 17, 2026

Acknowledgements

I was amazed by how quickly a project can progress when I attended a meeting where Prof. Yiwen brought together different scientists and called for collaboration. The lotus membrane, the theoretical derivations, and the interferometer work would not have been possible without Yiwen's support and organization. I am deeply grateful for the environment she created, in which ideas could quickly turn into concrete experiments and results.

My supervisor, Dr.Simon, has always managed to cheer me up with his sense of humor, while also giving me crucial feedback on my presentations, simulations, and experiments. From him, I learned not only how to approach scientific problems, but also how to collaborate with others and, perhaps more importantly, how to stay calm when things do not work as expected.

Many of my theoretical insights—and many of my theoretical puzzles—came from discussions with Raphael. There were quite a few moments when I felt rather stupid after messing up a derivation, and I am very glad that I could openly share this stupidity with Raphael, discuss it, and eventually understand where things had gone wrong.

I also felt the support of Frederike and Arianne in many small but meaningful moments: when they invited me to join lunch, or when they reminded others to use English so that I could take part in the conversation. I am also grateful to Arne and Andraz for sharing insights about thesis writing and presentation preparation. More generally, I would like to thank everyone in the HyQu group for creating such a supportive and collaborative environment.

I would especially like to thank my startup co-founder, Siyi, who has supported me enormously, both emotionally and on the startup side, while I tried to balance building a company with completing my thesis. Having someone who understood both the pressure of the startup and the demands of the thesis made this balancing act much easier.

Thank you all very much.

Abstract

Superposition is one of the basic properties presented in quantum mechanics but is not applicable to general relativity. Engineering a quantum system to achieve macroscopic quantum states with large delocalization provides a platform to examine the influence of gravity on quantum states, paving the way to unify general relativity and quantum mechanics. Although many experiments have succeeded in building macroscopic superposition states using molecules, nanoparticles, and microwave cavities [1][2][3][4], a controllable and massive system enabling the detection of gravity has not yet been presented. Here, this thesis investigates a possible experimental system with a membrane and superconducting circuit: the deep strong coupling(DSC) regime in a mechanical qubit system where the delocalization state is the ground state of the system. This thesis asks whether a kHz metallized high-(Q) (Si_3N_4) membrane can be capacitively coupled to a superconducting qubit strongly enough to reach the DSC regime while remaining electrostatically stable and experimentally accessible.

The theoretical calculation suggests that the DSC regime cannot be reached for the transmon-membrane system, while it is possible for the Cooper Pair Box-membrane system. An exact Hamiltonian is derived for a voltage-biased membrane-transmon system with consideration of the quadratic (A^2) term. In the adiabatic transmon limit, this quadratic term cancels the mechanical softening produced by the capacitive coupling between the membrane and transmon. Furthermore, for the single-sided parallel-plate geometry considered here, electrostatic pull-in occurs before the corresponding threshold of DSC regime is reached. A Cooper-pair box behaves differently because its ground-state charge-band curvature can remain negative, disabling the canceling effect. Within an ideal two-charge-state model, this leaves a parameter range in which the DSC regime may be reached before pull-in, although a full nonlinear treatment is still required.

The simulation on the transmon-membrane device verifies the infeasibility of the DSC regime. A finite-element workflow using COMSOL was developed to model the membrane mechanics, metallization-induced stress and loss, buckling risk, capacitance matrix, and coupling strength. The final transmon-based wheel-membrane design has a simulated mechanical frequency near 23 kHz and a coupling of approximately 0.775 MHz, below the calculated DSC critical coupling strength near 4.86 MHz.

The simulations and experiments on various membranes show the feasibility of a transmon-membrane device in room temperature and possibly at millikelvin temperatures. Buckling analysis of the membrane indicates that the metallized membrane will not suffer from buckling at 10 mK, given proper residual stress at 293 K. Interferometric measurements of three lotus membranes before and after 20 nm Al deposition show a frequency shift from 1.56 MHz to 1.39-1.41 MHz and geometry-dependent quality factor degradation, while the best metallized mode remains a high quality factor above 10^6. Finally, a gigahertz loop-gap resonator is proposed for cryogenic capacitive readout, demonstrating the possibility to read out such a device.

These results provide a concrete understanding of the membrane, identify the limitations of the transmon architecture, and offer a solid basis for simulating, designing, and fabricating future DSC-reachable devices.

Contents

Chapter 1

Introduction

1.1 Background and motivation

Although the quantum superposition state was discovered earlier, in 1935, Erwin Schrodinger brought the superposition state to a macroscopic object known as Schrodinger cat. The Schrodinger cat is a cat trapped in a special box. The box contains a machine that releases poison, a radiation detector to control the machine, and a source that emits radiation randomly. Once the detector reads radiation from the source, the poison will be released to kill the cat. After starting the machine in the box, we can only open it after an hour.

What makes Schrodinger cat special is that the state of the cat in the box is not deterministic. Before we open the box, whether the cat is alive or dead correlates with a probabilistic emission event. Suppose before we open the box, a radiation event occurs with 50% ; the state of the cat is therefore probabilistic: 50% alive and 50% dead.After we open the box, the state of the cat is clear.

To describe the transition of the cat's state from unknown to known before and after opening the box, one can interpret it as follows: the opening of the box, as an observation, collapses the probabilistic distribution of the alive and dead states of the cat into a deterministic result.

This is called the Copenhagen interpretation of quantum states. It features two beliefs: "measurement collapse states" and "states can be in superposition". This interpretation was invented in the 1920s by Niels Bohr and Werner Heisenberg to describe quantum particles that don't have a specific state unless measured. A typical quantum particle is an electron that exhibits the property of a wave when it is emitted through two separate, thin, and long slits. Unless we put a detector to track one specific position, the particle is present in two positions simultaneously with a certain probability.

To describe such a superposition state, we adopt Dirac notation. In Dirac notation, we use $|alive\rangle$,$|dead\rangle$ to define the cat state and $|1\rangle$,$|0\rangle$ for emitted and not emitted radiation. The state of the box before opening is represented by $|state\rangle$. $\langle state|state\rangle$ shows the probability of the state. The system in the box can be described as:

$$|state\rangle = \frac{1}{\sqrt{2}} |alive\rangle |0\rangle + \frac{1}{\sqrt{2}} |dead\rangle |1\rangle \tag{1.1}$$

If we calculate the probability of the state from eq.1.1, $\langle alive|alive\rangle \langle 0|0\rangle$, and $\langle dead|dead\rangle \langle 1|1\rangle$ represent the alive and dead states with a probability of 0.5. However, there are terms like $\langle alive|dead\rangle \langle 0|1\rangle$ and $\langle dead|alive\rangle \langle 1|0\rangle$.

Eq.1.1 is a typical example of a superposition state. Superposition states are the states that can be a linear combination of the probabilistic distribution of the original states[5]. In dirac

notation, It can be written as $|\phi\rangle = c_1 |\phi_1\rangle + c_2 |\phi_2\rangle$. The superposition state is different from classical states. Calculating the probability of a superposition state results in not only a $\langle\phi_1|\phi_1\rangle$ like state but also an interferometric state $\langle\phi_1|\phi_2\rangle$.

Applying the Copenhagen interpretation to a macroscopic object like a cat goes against the deterministic intuition we have. Schrodinger deliberately brought out the cat to criticize this interpretation. The cat is macroscopic, determined by newton's laws. There is no probabilistic description for a macroscopic object.

The controversy surrounding the existence of "Schrodinger cat" brings up the following question: Can quantum superposition be created with macroscopic objects. Specifically, Such a state is translated to a cat state:

$$|cat\rangle = N(|a\rangle + |-a\rangle) \tag{1.2}$$

if we aim to create a Macroscopic Spatial Superposition, $|a\rangle$ and $|-a\rangle$ are two states with opposite locations. Generally, $|a\rangle$ and $|-a\rangle$ are not limited to position. They can be phase, momentum, or other coordinates.

To this end, researchers have been engineering cat states on large objects, and some of them have demonstrated quantum superposition with a macroscopic object. A similar experiment conducted on an electron was achieved with the C60 molecule in 1999[6]. The C60 particle, which has a complex structure containing 60 atoms, has been shown to be present in two locations. The largest object of a similar nature was reported in a recent study using a nanoparticle containing 7000 atoms[2]. Bild *et al.* prepared cat states in a bulk acoustic resonator with an effective mass of 16.2 μg, corresponding to the collective motion of approximately 10^{17} atoms[7]. Gao et al. demonstrated a superposition state using 10 photonic qubits[8]. More and more experiments are extending the boundary for the size of quantum superposition.

Larger and larger cat states, especially the spatial one, potentially enable the detection of gravity. Such a detection is scientifically important because, theoretically, it is not clear how gravity disturbs the quantum state. Penrose stated that the quantum state should collapse due to gravity[9]. Non-interferometric experiments have excluded the natural parameter-free version of the Diósi–Penrose model[10], but no experiment has yet observed gravity-induced collapse in a controlled spatial superposition. Such an experiment would provide evidence for combining gravity and quantum theory, which is one of the paradoxes that have been studied for centuries.

Experimentally coupling gravity to the cat state remains a challenge. Such an interaction requires a massive but well-resolved positional superposition. Gravity scales with mass and distance. According to the Quantum Gravity Induced Entanglement of Masses protocol proposed by Bose, Sougato et al., for the influence of gravity on two positional states to be read out, one needs to have a large mass of 10 fg and a long delocalization of up to 100 μm [11]. This cannot be done on an electron or C60, whose mass is too small, nor on the HBAR device, where the delocalization is too small. Increasing mass and delocalization together is demanding. Fundamentally, the ground state position variation of an object, zero point fluctuation (x_{zpf}), scales with $\frac{1}{\sqrt{m}}$. Thus an increase in mass decreases the position variation of the object. Also, the delocalization decreases proportionally. In addition, environmental disturbances alter the larger delocalized object more, collapsing the quantum superposition state.

Moreover, precise control and readout of the quantum state are also required to make testing repeatable and observable. One of the experimental protocols to prepare a cat state, expose it to gravity, and read-out the result was discussed by Chiara Marletto and Vlatko Vedral[12]. Engineering the ground state to the superposition cat state requires an interferometer and shielding from heat and electric field disturbances. To read out, one also needs to transfer it back to the detectable basis and ensure that the detection is weak enough not to collapse the

original state. This is challenging to engineer. A useful macroscopic cat-state platform should combine a large participating mass, a large spatial separation, a sufficiently long coherence time, and the ability to prepare and verify the state.

Research has been seeking such a platform. In 2003, Marshall *et al.* proposed using radiation pressure from a single photon to place a micromechanical mirror containing approximately 10^{14} atoms into a spatial superposition[13]. Vlastakis et al. couple a cavity to a transmon, creating a microscopic cat state with a size of 100 photons[14]. To compare experiments with different atoms and setups, the definition of how macroscopic states are defined was presented in [15]. The most macroscopic state, according to this benchmark, is the nanoparticle experiment mentioned above[2]. However, no such an platform has been successfully developed.

Among those methods, mechanical oscillators are a promising approach because they offer a much larger effective mass together with precise local control and repeated readout[16]. Using a mechanical oscillator based on trapped ions, Lo et al. create a cat state with a size that is 56 times larger than the wave packet[17]. Recently, Bild *et al.* prepared cat states in a bulk acoustic resonator with an effective mass of 16.2 μg, corresponding to the collective motion of approximately 10^{17} atoms[7]. However, their physical displacement was only of the order of 10^{-18} m. Matter-wave interferometers achieve a large center-of-mass separation but provide limited control over the particle after propagation, whereas mechanical resonators provide strong control and readout but have so far produced very small absolute displacements.

One possible route to obtaining an easily prepared and readout macroscopic superposition state with large absolute displacement is the deep-strong-coupling regime of the quantum Rabi model. The quantum Rabi model describes the interaction between a single mode oscillator and a two level qubit. For a qubit coupled to a mechanical mode, the idealized Hamiltonian can be written in Rabi model as

$$\omega_{\mathrm{m}} a^{\dagger} a + \frac{\omega_{\mathrm{q}}}{2} \sigma_z + g \sigma_x \left(a + a^{\dagger}\right).$$

The first two terms represent the energy of the resonator and the energy of the qubit. ω_m is the resonator frequency, while ω_q is the qubit frequency. $a^{\dagger}a$ and σ_z are the number operators for the resonator and the two level qubit. The number operator counts how many units of energy the resonator and qubit have. The third term is the coupling term, where σ_x and $a + a^{\dagger}$ are the position operators for the qubit and the resonator. The position operator counts the x position.

The deep-strong-coupling(DSC) regime is conventionally associated with $g/\omega_{\mathrm{m}} \gtrsim 1$, and is generally defined as $g \geq \frac{1}{2}\sqrt{\omega_m \omega_q}$ [18]. We treat $g \geq \frac{1}{2}\sqrt{\omega_m \omega_q}$ as the DSC regime criterion in the following text. In this regime, by displacing the qubit and resonator against each other, the dominant coupling term decreases the total energy. The two qubit states shift the equilibrium position of the oscillator in opposite directions. The ground state can be obtained by extracting the eigenvector that has the smaller eigenvalue:

$$|\Psi_{\pm}\rangle \simeq \frac{|+_x\rangle\,|-\alpha\rangle \pm |-_x\rangle\,|\alpha\rangle}{\sqrt{2}}, \qquad \alpha \simeq \frac{g}{\omega_m}.$$

Using $x = x_{\mathrm{zpf}}(a + a^{\dagger})$, the centers of the two mechanical branches are separated by

$$\Delta x \simeq 4 \frac{g}{\omega_{\mathrm{m}}} x_{\mathrm{zpf}}. \tag{1.3}$$

Here x_{zpf} is the zero point fluctuation. It is the fluctuation of the membrane at ground state

due to the Heisenberg uncertainty principle

$$x_{zpf} = \sqrt{\frac{\hbar}{2m\omega_m}} \tag{1.4}$$

The ground state in the DSC regime is therefore an entangled qubit–oscillator cat rather than a pure mechanical cat by itself. A measurement of the qubit in a suitable basis can project the oscillator into an even or odd mechanical cat state. The advantage of this regime is that the cat-like branch structure appears in an eigenstate of the system instead of only during a short transient evolution. In addition, increasing a low-frequency resonator could enable higher delocalization.

Coupling strength in the DSC regime has been achieved in several experimental setups. A cat state in the DSC regime was produced by quantum simulation in a superconducting circuit [19]. Using a superconducting flux qubit coupled to an LC resonator, Yoshihara et al. demonstrate the transition spectrum of the DSC regime [20]. However, these experiments use a GHz level oscillator. The delocalization factor $\frac{g}{\omega_m}$ is thus small.

Increasing delocalization motivates the use of low frequency oscillators. There are two types of mechanical oscillators that possess low frequencies at the kHz level: the membrane and the levitated nanoparticle. A 100 kHz membrane with a quality factor on the order of 10^8 was reported [21]. Dania et al. achieved a quality factor of 10^{10} for a 1 kHz levitated nanoparticle[22] in ultra high vacuum to a level of 10^{-11} Bar.

Compared with the levitated nanoparticle, the membrane offers an experimentally easier integration with the superconducting circuit. A usual way to trap the nanoparticle involves using a Paul trap, which employs several AC charged rods to produce a trapping field for a charged nanoparticle. Operating the Paul trap produces a high voltage AC electric field that unavoidably leaks out to the peripheral region. A nearby superconducting circuit would be significantly disturbed due to RF crosstalk and heating[23]. The membrane is suspended during fabrication. No external electric field is needed to suspend it.

The membrane also addresses the sample preparation issue at cryogenic temperatures for the levitated nanoparticle. To enable quantum operation, one needs to cool the superconducting circuit down to millikelvins in a high vacuum. Loading and maintaining a nanoparticle during the cooling and vacuum process is challenging [24]. The pump will force the particle out of its equilibrium state and cause the loss of the particle. The trap electric rod also undergoes thermal contraction and may potentially change the trapping field during cooldown; its shape will require sophisticated design to accommodate[25]. For membranes, the above problem doesn't exist.

We therefore adopt membranes as the low frequency oscillator, a superconducting qubit as the two level system. This fills up the first two terms in the quantum Rabi model. For the coupling term, we can engineer flux coupling or capacitive coupling as the coupling mechanism. In flux coupling, the change of the oscillator causes a flux change in the superconducting circuit. In capacitive coupling, the oscillator induces a charge change in the circuit. For the simplicity of implementation, we take capacitive coupling. A parallel capacitor between the membrane and the qubit is enough to transduce the movement of the membrane to charge on the qubit. For flux coupling, external B field modulation requires extra ferromagnetic material on the membrane [26]. Capacitive coupling provides a comparatively easy fabrication geometry based on a controlled vacuum gap.

The core question we want to ask is whether a low-frequency membrane can couple strongly enough to a high frequency qubit, forming a controllable, position separated ground state. This motivates us to pose the following research questions.

1.2 Research objectives and contributions

This thesis aims to answer three questions:

- Given a capacitive coupling structure, does the coupling between the membrane and the superconducting circuit provide a large enough tuning range to enter DSC?
- What are the considerations and risks to avoid in device design?
- How do we read out this device?

This thesis will present the theoretical calculation of the capacitive coupling scheme between the membrane and superconducting qubits, membrane simulation methods, device design and simulation, optical measurement results of the metallized membrane, and the proposal for future cryogenic readout of the mechanical spectrum of the membrane.

We obtain evidence showing that it is unable to enter the DSC regime using capacitive coupling between the membrane and the transmon qubit. The membrane pull-in occurs before achieving DSC critical coupling. The difference in the Hamiltonian in the copper pair box(CPB) seems to eliminate the infeasibility of entering. This provides a suggestion for future architectural design.

We have simulated a variety of membrane designs and tested buckling, thermal conductivity, and quality factors. Simulation and optimization show that a high quality factor membrane can be built with metallization and that it can survive in a cryogenic environment. This resolution addresses some concerns about the fabrication of the device and enables further discovery on device characterization.

We have also demonstrated methods for reading out the mechanical spectrum of the membrane at cryogenic temperatures, enabling the cryogenic detection of the membrane mechanical spectrum.

1.3 Thesis structure

This thesis will introduce the theory of membranes, superconducting circuits, and coupling mechanisms in chapter.2. With the general understanding of the device, we start to derive the theoretical limits of coupling in chapter.3. In chapter.4, we show the device design of the membrane and qubit with simulation support. A preliminary experimental result on the influence of metallization is presented in chapter.4.2. We finally provide a proposal on the cryogenic readout of the mechanical spectrum in chapter.5. A summary of the thesis is presented in chapter.6.1.

For a detailed simulation procedure, The methods in membrane simulation chapter in the Appendix B present how we can credibly simulate the membrane and transmon qubit.

Chapter 2

Components for metallized membrane-qubit electromechanics

The capacitive coupling membrane-qubit device consists of a membrane oscillator, a superconducting qubit, and packaging that combines the components. To achieve a sufficiently large coupling for creating a macroscopic cat state of the membrane-qubit device, we need to understand which design enhances coupling. In a top-down level, we need to know which parameters of the membrane and qubit are related to the coupling and in what sense. Then we start by asking how to achieve the physical parameters of the membrane and qubit based on their geometry and fabrication processes.

In this chapter, we will discuss the latter question only. We introduce the membrane we study, its eigenfrequency, and quality factor. Then, we introduce the transmon regime of the superconducting qubit. The packaging and calculation of the coupling mechanism will be discussed partly at the end.

To complete the picture of coupling, the next chapter will discuss a detailed derivation of the coupling Hamiltonian for the transmon and cooper pair box.

2.1 The high Q fractal Si_3N_4 membrane resonator

In the membrane-qubit device, the membrane resonator is a thin layer tied to a frame, acting as a mechanical oscillator. An example of a membrane is a drum. When the performer hits the thin layer, the surface of the drum vibrates and produces sound at a specific tone. Unlike the musical usage of drums, the use of a membrane oscillator prefers a high quality factor and a low frequency to gain sensitivity for force[27]. Towards this direction, the membrane's geometry was altered. Phononic crystals, a periodic structure with holes or protruding edges[28], and fractal-like geometry, a multi-stage structure[29], were invented to reduce the loss at the hundreds of kHz level in membranes. The membrane we choose is the fractal one presented in [21]. Because the fractal-like geometry allows a large center pad in the oscillator to couple to the qubit. In this section, we will introduce the geometry of the membrane and how the geometry of the membrane relates to hundreds of kHz frequency and 10^8 quality factor.

Depicted in figure.2.1, the wheel-shaped Si_3N_4 fractal structure membrane is the target membrane we chose. Three groups of white tethers consist of a fractal pattern: the thin trampoline that connects the frame to the center part, the surrounding wheel-shaped branches, and the branch that clamps the wheel-shaped membrane to the membrane frame(not shown). We name them the branches of the first, second, and third stages of the membrane. Branches in neighboring stages are hierarchical. A specific rule governs that by shrinking and rotating, one can

have tethers of different stages coincide with each other. The initial long and thin tether set the initial length and width. The next tethers reduce the length by $r0 = 0.45$ and increase the width by $\frac{1}{2cos(86.5)}$. Until the fractal structure connects the frame, the membrane structure suspends above the Al_2O_3 substrate in black. The size of such a device is usually at the millimeter level, which sets the fundamental resonance frequency to hundreds of kHz, according to the sinusoidal equation : $v = \frac{1}{2L}v_s$[30]. L, v_s represents the tether length and the speed of sound in the membrane. For prestressed silicon nitride, the speed of sound is around 600 m/s.

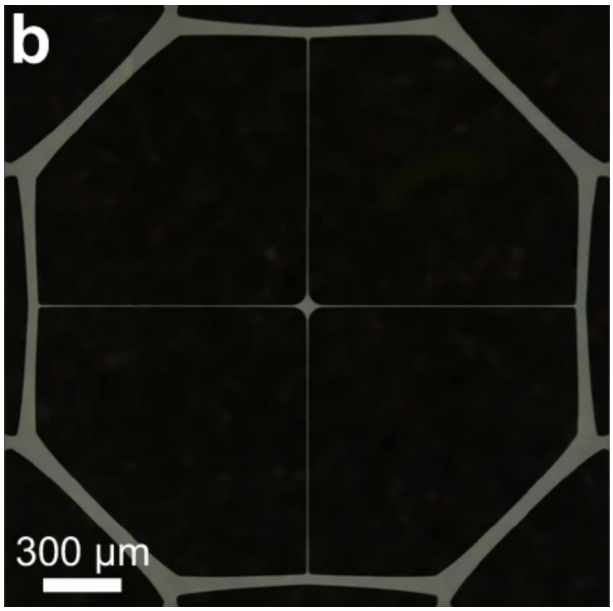

Figure 2.1: Microscopic image of the Wheel membrane extracted from ref.[21]. The white part is Si_3N_4. The black part is Si. The silicon nitride membrane suspend on top of the silicon substrate. Eight legs of membrane connect the substrate.

We chose the fractal structure to enable soft-clamping of the membrane to the frame, leading to a high quality factor of the membrane. Soft-clamping is a membrane clamping design that does not fix the oscillating membrane firmly to the frame. Therefore, the membrane curvature does not exponentially decay near the connection point, but along the whole membrane. In figure.2.1, the point where four fundamental tethers connect to other tethers is flexible. No hard confinement was enforced on it. Going a stage further, The connection point is still flexible. Only at the point where the membrane connects to the frame are the mechanics limited by the frame. So, the center part of the membrane is softly clamped to the frame. More importantly, the amplitude of deflection decreases from stage to stage. The dissipation of deflection correlates with the high dilution factor of such a membrane. The dilution factor is a measurement of the proportion of lost energy in one oscillation, contributing to the quality factor of the membrane by $Q = D_Q Q_{int}$. D_Q is the dilution factor; Q_{int} is the intrinsic quality factor of the material, also known as the loss tangent of the material.

Fractal structure based soft-clamping requires specific geometric design laws. Figure.2.2 depicts one fractal membrane design for the illustration of the laws of the fractal membrane. The parameters that define the geometry present in tab.2.1.

The first law is that the length of the tether decreases by a factor of r0 when going to the next stage. The second law is that the tether width follows the equation $w_{i+1} = \frac{w_i}{2\cos\theta}$ for two successive tether levels. The third law is that the angle for the tether between successive tether levels is θ.

Table 2.1: Summary of Tether and Center Pad Design Parameters

Symbol	Description	Unit
pad_l	Length of the center pad	μm / mm
l_0	Length of the fundamental (first-level) tether	μm / mm
r_0	Length ratio between successive tether levels	—
θ	Angle between tethers at the joint	rad / °
w_0	Width of the fundamental tether	μm / mm

Those laws ensure a balanced fractal structure. The first law defines fractal geometry. It may help to block the center mode from the edge due to a boundary conditions mismatch. The second law ensures that there is a balanced force at the point where one branch splits into two. Otherwise, the membrane will be torn. The third law defines the symmetry of the device. If the angle is not set, the branches could connect to each other differently. Altogether, a fractal structure is enabled.

Getting back to the design of the wheel membrane, the fractal laws remain, while the connection rules change slightly. We connect all of the branches at the second stage. To comply with the change, part of the branches at the third level is removed. Branches at the fourth level join the frame or are deleted. The connection of the tether in the second stage forms a wheel like shape; thus, we call it a wheel membrane.

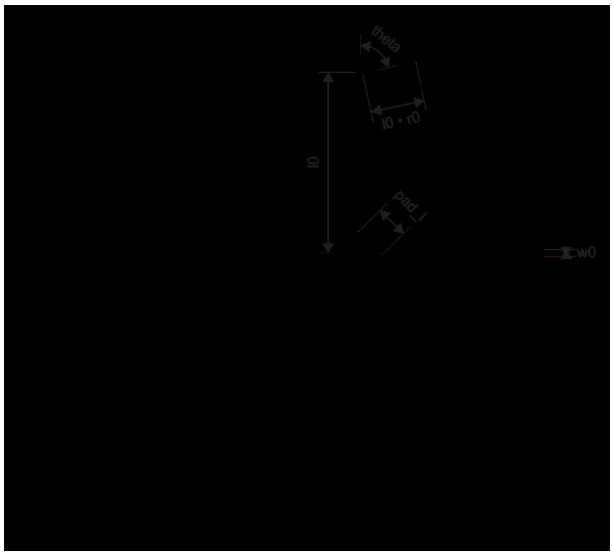

Figure 2.2: Schematic of hierarchical structure membrane with construction parameters indicated. only the relation between first and second tether is shown. The construction rule like length contraction ratio, theta angle also apply to the rest of tethers.

The high quality factor of hierarchical membranes demands high tensile stress materials. Tensile stress increases the kinetic energy and reduces the bending energy. The dilution factor is therefore high. The detailed equation can be seen in the discussion of the quality factor later.

To achieve GPa tensile stress, a patterned Si_3N_4 thin film that grows on an Al_2O_3 substrate is used. By low pressure chemical vapor deposition (LPCVD) at 800 degrees and the cooling process, tensile stress builds up due to the mismatch of Si_3N_4 and Al_2O_3 contraction. To release the membrane, KOH wet etching or dry SF_6 etching is used. The Al_2O_3 will be eroded,

suspending the Si_3N_4 thin layer.

The use of High tensile stress material defines the frequency of the membrane, together with the size of the membrane, mass, and cross-section geometry. A qualitative but informative equation from the wave equation shows this:

$$m_{eff}\omega_m^2 = k = \frac{\sigma A}{L} \tag{2.1}$$

where m_{eff} is the effective mass of the membrane, ω_m is the angular frequency , k is the spring constant, defined by the prestress value σ, the cross-sectional area A, and the length of the tether L. We can change the frequency,by changing those parameters.

The goal of membrane design in this chapter is to inversely map the required eigenfrequency, effective mass, and quality factor to the geometry of the membrane. To gain intuition, we will use a simple string and mass model in the following session. We abstract the membrane to the model of a block of mass m_c connected by two strings with a spring constant k, mass m_l, and length L as shown in figure.2.3. The deflection angle θ is assumed to be very small to allow for the relation $sin(\theta) = \theta$.

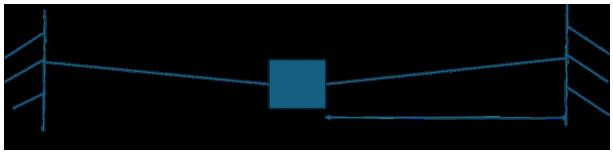

Figure 2.3: The simple model to show the 2D string model. The center block and two line represents pad and tether of the membrane. The two vertical lines represents the wall. The distance of tether here is L/2.

2.1.1 Eigen-frequency and mode shape

To analytically study the membrane eigenfrequency, a general formula is required for the mechanics of the 2D string model in figure.2.3. Ref[30] provides a good explanation, and it is worthwhile to show it here again:

$$EI\frac{\partial^4 z}{\partial x^4} - \sigma A\frac{\partial^2 z}{\partial x^2} + \rho A\frac{\partial^2 z}{\partial t^2} = F(x) \tag{2.2}$$

where E is the Young's modulus, I is the second moment of area (or moment of inertia), σ denotes the tensile prestress, A and ρ are the cross-sectional area and mass density of the string, respectively, and F represents the external force. z is the wave function superimposed by different modes and can be written as:

$$z_n(x,t) = \sum a_n(t)u_n(x)$$

where $u_n(x)$ is the mode shape and $a_n(t)$ is the time dependent amplitude of the mode. High tensile stress material implies that σA is much larger than EI. This magnitude difference suggests that the first term of equ.2.2 can be ignored.

Considering the intrinsic eigenmode without any external force, we can simplify Eq.2.2 to:

$$-\sigma\frac{\partial^2 z}{\partial x^2} + \rho\frac{\partial^2 z}{\partial t^2} = 0$$

Expanding z with amplitude and mode shape, we have

$$-\frac{\partial^2 u}{\partial x^2} + \frac{\rho}{\sigma}\omega^2 u = 0$$

If we include the boundary conditions $u_0(0) = 0$ and $u_l(L) = 0$ in the equation, we will have the mode shape and the eigenfrequency equation as follows:

$$u = \sin(\frac{n\pi}{L}x) \tag{2.3}$$

$$v = \frac{\omega_m}{2\pi} = \frac{n}{2L}\sqrt{\frac{\sigma}{\rho}} \tag{2.4}$$

For such a 2D string model, the mode shape is sinusoidal. If we have 4 tethers sharing a small enough pad , we add one more degree of freedom, writing the mode shape and frequency as:

$$u = \sin(\frac{n_x\pi}{L}x)\sin(\frac{n_y\pi}{L}y) \tag{2.5}$$

$$v = \frac{\omega_m}{2\pi} = \frac{\sqrt{n_x^2 + n_y^2}}{2L}\sqrt{\frac{\sigma}{\rho}} \tag{2.6}$$

Degeneracy modes occur for groups of n_x and n_y combinations fulfilling condition $\sqrt{n_x^2 + n_y^2} = N$.

The membrane eigenfrequencies depend on its length, material density, and the magnitude of the tensile stress, according to the tensile stress dominated 2D string. Eq.2.4 indicates such a relation. Estimation can therefore be made of the fundamental mode frequency given those parameters. Taking L as 2 mm, ρ as 3100 kg/m^3, and σ as 1 GPa, the fundamental mode frequency is 141.99 kHz.

The 2D string model provides a good estimation of the frequency when the center pad is small. However, when the center pad is large, Eq. 2.2 breaks down because we cannot ignore the bending term in the center pad region due to stress decay. The center pad, which has a larger area, shares the same tensile stress as the thin tether, according to newton's third law. With a larger cross-sectional area, the stress of the center pad is significantly smaller. The bending term that curves the edge of the membrane also increases the moment of inertia. Together, the first term of the equation.2.2 is manifested.

In addition, the 2D string model struggles to consider the soft-clamping effect. The 2D string clamp firmly attaches to the wall; therefore, it is not a soft-clamping model. The membrane frequency is overestimated in 2D string model. The frequency estimation of 141.99 kHz is 50% higher than the frequency of the soft-clamped membrane reported in [21]. This is because soft-clamping prolongs the effective length of the string, thus decreasing the frequency according to eq.2.1.

To account for the soft-clamping effect in the 2D string model, we use the effective mass shown in eq.2.1 $m_{eff}\omega_m^2 = k$. The effective mass translates the soft-clamping conditions into a correction of the mass. We define m_{eff} as the average contribution of the membrane mass according to the mode shape. The definition of membrane effective mass can be seen in [30]:

$$m_{eff} = \int dV \rho(r)|\boldsymbol{r_n(x)}|^2 \tag{2.7}$$

No matter what shape the mode takes, their contribution appears in the effective mass. The Soft-clamping condition is a modification to the mode shape. It can also be corrected.

We can recalculate the eigenfrequency estimation of the soft-clamped 2D string using effective mass. For the 2D string model, calculating the normalized model shape $r_n(x)$ gives $\frac{m_{eff}}{m_s} = \frac{1}{2}$. For a cantilever, $\frac{m_{eff}}{m_s} = \frac{1}{3}$. We can assume that the 3D membrane with the pad is composed of four cantilevers with one pad, the total effective mass can be written as $m_{eff} = m_p + \frac{4}{3}m_c$. The $k = \frac{F}{z}$ can be written as $\frac{4\sigma A}{L}$. Assuming a stress of 1.03 GPa, the center pad of $45 * 45$ μm^2, the tether length is 1 mm, the thickness is 100 nm, and the width is 5 μm. The frequency is

$$w_m = \sqrt{(\frac{\sigma A}{m_{eff} L}} = 2\pi(101.879kHz) \tag{2.8}$$

The correction is comparable to the fundamental mode frequency of the soft-clamped membrane. Notice that the above estimation assumes the effective mass of the membrane can be linearly combined with its components. This method may not be accurate and is infeasible for estimating the phononic bandgap of the membrane.

The actual effective mass of a soft-clamped membrane requires FEM simulation to verify because the existence of the center pad and hierarchical structure complicates the boundary conditions and wave equation. The center pads are larger than the tethers. It is therefore a 2D object rather than 1D, having more degrees of freedom. Soft-clamping allows little movement around the clamping point. If the clamping is not hard, the membrane could rotate, twist in-plane. The 2D string model is a good approximation if the geometry of the membrane resembles the string, but it may not capture the behavior of a multistage fractal structure with a large pad.

Starting from the effective mass of the membrane, we can tune the frequency of the membrane through length, effective mass, and other parameters. We primarily change the length. The effective mass of the membrane is not as tunable as the length because the mode shapes are not easy to change. Most of the effective mass contribution comes from the center pads and the tethers of the third stage, which is almost flat when moving. The effective mass will thus not differ by an order of magnitude. We can also alter stress. This change in the fabrication process is required and is beyond the scope of this thesis.

2.1.2 Dissipation dilution and mechanical Q factor

The dilution factor and intrinsic quality factor of the fractal membrane control the quality factor. To see this, the analytical expression for the quality factor of a tension dominated membrane is [31]:

$$Q = D_Q Q_{int} = \frac{E_{total}}{E_{bending}} Q_{int} \tag{2.9}$$

The final Q value is the product of D_Q and Q_{int}, the intrinsic quality factor of the material and the dilution factor. Physically, The intrinsic quality factor reflects the intrinsic loss of the material, usually written as the ratio between the imaginary and real parts of the Young's modulus. This loss is diluted by the dilution factor D_Q in the fractal membrane. The fractal geometry preserves the total energy mostly as lossless kinetic energy. The dilution factor is the ratio between the total energy and the bending energy. It represents the intrinsic loss of the geometry. The products of these two terms measure how kinetic energy transfers to loss through fractal geometry and silicon nitride, giving the total quality factor. The typical value for the intrinsic quality factor of Si_3N_4 is 2500(298K)[21]. For Al, the intrinsic quality factor

is 480(10mK)[32]. The dilution factor can reach thousands, producing quality factors above millions.

Ref.[31] presents a general representation of the quality factor, assuming that the material does not squeeze or expand when stretched or compressed.

$$D_Q = \frac{E_{total}}{E_{bending}} = 1 + \frac{\int 2e_{ij}\langle \Delta e_{ij}(t)\rangle \, dV}{\int \langle \Delta e_{ij}(t)\Delta e_{ij}(t)\rangle \, dV} \tag{2.10}$$

$\langle\cdot\rangle$ is the time average. With the total deformation field as $\tilde{U}_i = U(x, y, z, t)$, the strain tensor is defined as e_{ij}.

$$\tilde{e}_{ij} = \frac{1}{2}\left(\frac{\partial \tilde{U}_i}{\partial x_j} + \frac{\partial \tilde{U}_j}{\partial x_i} + \frac{\partial \tilde{U}_l}{\partial x_i}\frac{\partial \tilde{U}_l}{\partial x_j}\right) \tag{2.11}$$

The strain tensor can be decomposed into the summation of a static tensor and a time dependent tensor. e_{ij} is the static deformation caused by the prestress. Δe_{ij} is the time-dependent part that changes when the membrane oscillates.

$$e_{ij}(t) = e_{ij} + \Delta e_{ij} \tag{2.12}$$

According to eq.2.10, the dilution factor depends on the curvature and the surface gradient of the membrane. For a deflection motion where the membrane moves only in the z direction, the time-dependent strain tensor Δe_{ij} has a major contribution in the form of $\frac{\partial U_z}{\partial x}\frac{\partial U_z}{\partial y}$, which is proportional to the surface curvature. Due to the flatness of the membrane at the quantization position, the static strain tensor is dominated by $\frac{\partial U_z}{\partial x} + \frac{\partial U_z}{\partial y}$, which is the surface gradient. Using the mode shape $\sin(kx)$, the gradient is proportional to k, which is also proportional to stress. Increasing stress and reducing the curvature thus increase the dilution factor. To have a dilution factor significantly larger than 1, e_{ij} should have the same sign in the integration region to avoid cancelation. $\langle \Delta e_{ij}(t)\rangle$ should be small.

The prestressed fractal structure membrane, which dissipates the curvature near the clamping point by soft clamping, can thus achieve a very high quality factor. The hard clamping imposes a hard boundary condition and enforces an exponential decay of the deflection near the clamping point, where the curvature increases exponentially. By releasing the clamping condition, the fractal structure dissipates curvature. The hierarchical quality factor membrane can reach 10^8, while the quality factor for the hard-clamped square membrane usually reaches 10^6.

To compute the quality factor of the fractal membrane in FEM software, we estimate equ.2.10 using the following formula[21]:

$$D_Q = \frac{\frac{12\rho\Omega_m^2}{Eh^2}(1-\nu^2)\int w^2 \, dx \, dy}{\int \left[\left(\frac{\partial^2 w}{\partial x^2} + \frac{\partial^2 w}{\partial y^2}\right)^2 + 2(1-\nu)\left(\left(\frac{\partial^2 w}{\partial x \partial y}\right)^2 - \frac{\partial^2 w}{\partial x^2}\frac{\partial^2 w}{\partial y^2}\right)\right] dx \, dy}, \tag{2.13}$$

where w,ν,E,h,ρ represent the shape function of the mode, the Poisson ratio,the young's modulus,the height of the membrane, and the density of the membrane. This equation is nothing but an expansion of eq.2.10 representing the ratio between kinetic energy and bending energy.

Tuning the device curvature and surface gradient to enable a high quality factor is not the primary design goal. The quality factor is reported to be over 10 million for the wheel membrane [21], which affords a decoherence time at the millisecond level given by $\tau = \frac{f}{Q}$. This is more than enough for operations at the microsecond level on qubits.

The design goal is to check if there is any possibility that the quality factor drops significantly during the entire process. Nevertheless, optimization of device geometry to improve quality has been conducted.

2.1.3 Metallization influence

The metallization process, which makes the membrane conductive, potentially degrades the quality factor of the membrane. In metallization, we deposit a thin film of Al on the surface of the membrane by e-beam evaporation or sputtering. During the sputtering process, Al atoms are accelerated and struck against the membrane, forming a highly stressed solid interface. Evaporation is a gentler process. Al vaporizes and condenses on the surface, forming a less stressful interface. Both methods introduce aluminum to the top of the silicon nitride. Ignoring the surface loss, Aluminum thin film is more than five times lossier than silicon nitride. Considering fabrication impurities, surface defects, oxidation, and clamping loss, the quality factor may degrade by a factor of more than 10.

Metallization changes the stress distribution and effective mass of the membrane, which directly alters the eigenfrequency and modes of the membrane. The internal stress accumulated on Al is contractive[33] with a value of -230 MPa for 70 nm thick layer. Such an additive layer on top of the silicon nitride membrane modifies the effective stress of the membrane. The spring constant, according to eq.2.1, increases slightly. The addition of metal thickens the membrane, increasing the effective mass. Together, the frequency of the membrane decreases because the increase in the effective mass of the membrane overcomes the increase in the spring constant .

Another effect of stress redistribution is buckling. Buckling is the sudden bending or distortion of the membrane when a disturbance appears. Observing Equ.2.2, an imaginary solution appears when we have a sign change in stress. An area with compressive stress may indicate a sign change in the formula, resulting in an unstable solution. The mode function changes drastically around the buckling region, causing external energy loss or breakdown of the device. However, if compressive stress dominates in some principal stress direction, The abrupt sign change may not happen. Compressive stress distribution across the membrane itself cannot predict buckling. It is a risk indicator for the design.

The influence of metallization on the mode shape has a temperature dependency. When the temperature changes, aluminum undergoes thermal contraction, affecting the stress inside. From 293 K to 10 mK, internal stress was recorded to increase from -50 MPa to 250 MPa in the silicon substrate[34]. Simulating the composite material with different stresses effectively returns the modes and quality factors at different temperatures. We can monitor whether the cooling process risks the membrane by causing buckling.

The design goal is to validate the resilience of the designed membranes in metallization and cooling.

2.2 Superconducting qubits

In the membrane-qubit device toward the DSC regime, we use the superconducting qubit. A superconducting qubit is an artificial atom that operates at millikelvin temperatures[35]. The artificial atom is made of a circuit containing capacitors, inductors, and Josephson junctions, a nonlinear tunneling inductor. The circuit, made with superconducting materials such as aluminum, allows charge, flux, or electric field to oscillate. The energy of each oscillation can be quantized at millikelvin, forming an energy diagram like that of an anharmonic oscillator. The

superconducting qubit stores its 0 and 1 information in the ground state and the excited state of the oscillator.

Superconducting qubits have many types. The types we choose are charge qubit and phase qubit, namely Cooper pair box(CPB) and transmon. They all use capacitors and josephson junctions only. The CPB uses the charge basis, where the 0 and 1 states of the qubit correspond to 0 charge or 1 charge in the circuit. The charge lives on a circuit island. A microwave excitation can change or superimpose the number of charges on the island, changing the qubit state. Charge on the island is sensitive to the electrical environment. Therefore, the decoherence time, the time the qubit state takes to decay, is short for CPB. To eliminate charge noise, the transmon has a small Josephson junction and a larger capacitor to ensure that the Josephson energy is large. The basis is the phase of collective charges, making them inert to charge noise. The typical decoherence time of the qubit can exceed 50 μs, with some samples reaching hundreds of microseconds[35].

In this session, we will show the circuit model of the superconducting qubits and how the qubit frequency and anharmonicity are tuned.

2.2.1 Grounded qubit and floating qubit

Superconducting transmon qubits generally come in two flavors: grounded and floating. In a grounded qubit—most famously the cross-shaped "Xmon"—the Josephson junction connects a single metal island directly to the surrounding ground plane, acting like a single electrical node where each arm can easily plug into a readout resonator, a control line, or a neighbor[36]. A floating qubit, by contrast, uses two separate metal pads that form a dipole pair without touching the ground plane, meaning the qubit mode lives between the two pads rather than against the ground [37]. While grounded qubits are much easier to wire and scale up on a flat 2D chip, floating qubits are naturally insulated from noisy ground loops and lossy substrate seams, creating a classic trade-off between easy wiring and cleaner protection against noise.

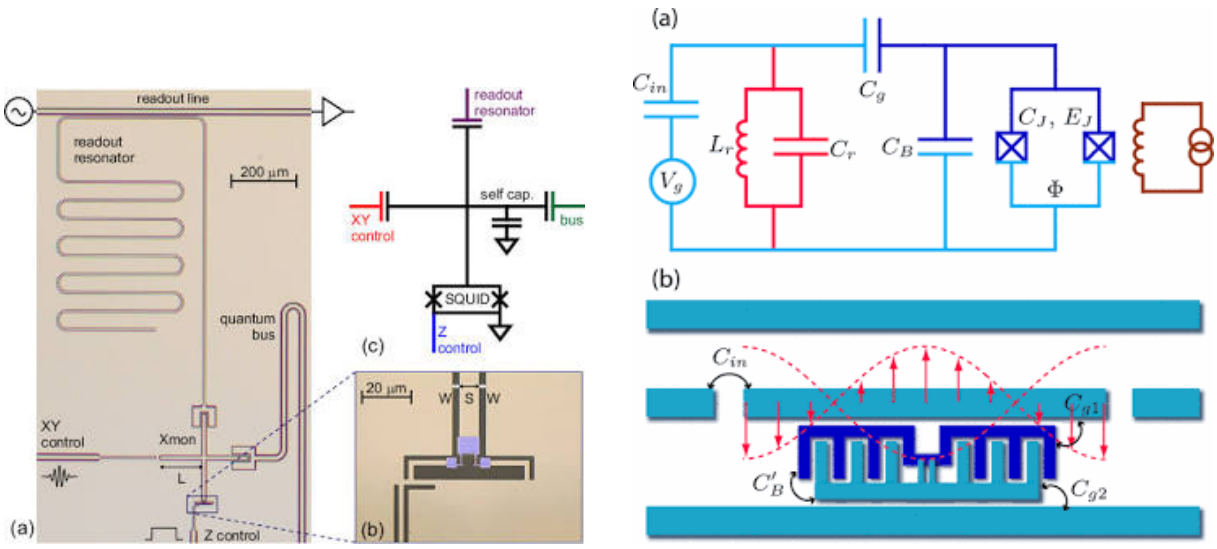

(a) xmon **(b)** transmon

Figure 2.4: Schematics of the grounded qubit and the floating qubit

2.2.2 The circuit model and the qubit Hamiltonian

We can abstract the qubit Hamiltonian using the lumped circuit model. Fig.2.5.(c) demonstrates the circuit representation, where C_s is the capacitor. L_J,C_J represents the inductance and capacitance of the Josephson junction. The energy diagram of the LC resonator and transmon is visualized in Fig.2.5.(b) and (d).

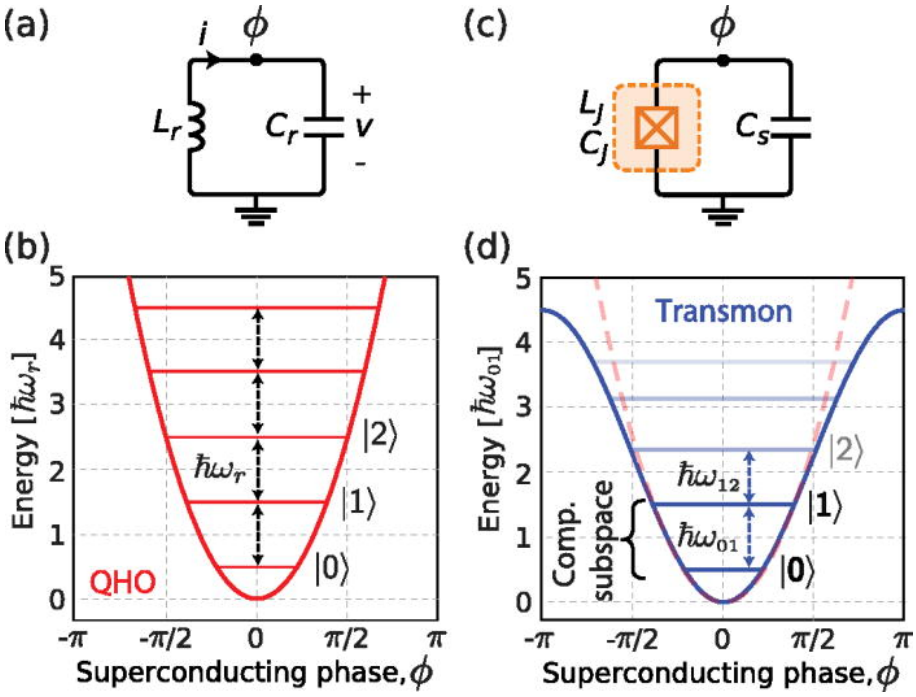

Figure 2.5: The circuit diagram and the energy diagram of LC resonator and transmon. Extracted from [35]

The Hamiltonian of the CPB and transmon originates from the equation:

$$H = E_j \cos(\theta) + E_c(n - n_g)^2 \tag{2.14}$$

where E_j is the Josephson junction energy and E_c is the capacitance energy that charge accumulates when passing through it.

To distinguish the CPB regime and Transmon regime, we take the charge basis with $|n\rangle = Ae^{i\phi n}$. Expanding $\cos\theta$ as $\frac{1}{2} \cdot (e^{i\theta} + e^{-i\theta})$, the Hamiltonian can be rewritten as:

$$H = \frac{1}{2}E_J(|n\rangle\ \langle n-1| + |n-1\rangle\ \langle n| + E_c(n - n_g)^2\,|n\rangle\,\langle n| \tag{2.15}$$

Here, E_c is the prefactor of the quadratic function. If we plot it against n, E_c controls how wide the quadratic function opens, which is the curvature. Notice that for every n, there is a quadratic function. If we scan n_g, Whenever n_g is an integer, we obtain a point where the corresponding quadratic function touches the x-axis. Plotting eq.2.15, we obtain a forest of quadratic functions bending upward. They have multiple crossover points, like those in the top-left diagram in fig.2.6. E_j is the prefactor of a cross coupling, which avoids two function crossings. Together, on a charge basis, the energy diagram can be visualized as follows:

At small $\frac{E_j}{E_c}$, achieved by a small capacitor, we enter the charge qubit regime[38]. The quadratic potential defines the charge state. The coherence time of the charge qubit is usually

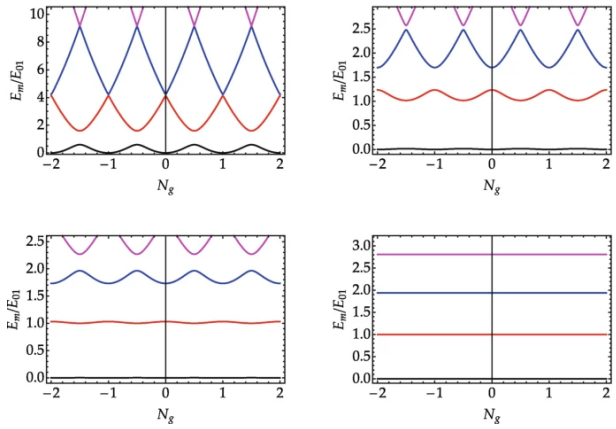

Figure 2.6: The Energy diagram-biased changed plot extracted from [37]. From top to down, left to right, the Ej/Ec ratio is 1,5,10,50.

low because the charge can be easily affected by defects in the material, noise in the microwave, etc.

At large $\frac{E_j}{E_c}$, typically achieved by extra shunt capacitance between the two islands, we enter the Transmon regime[37]. Here, the qubit states become collective charge states delocalized across many charge configurations, and charge noise is exponentially suppressed. As a result, transmons routinely reach coherence times exceeding 100 µs [35].

The Hamiltonian of the transmon requires further treatment. By expanding the cos potential[35], we have:

$$E_J \cos(\phi) = \frac{1}{2}E_J\phi^2 - \frac{1}{24}E_J\phi^4 + \mathcal{O}(\phi^6). \tag{2.16}$$

After the quantization, we obtain:

$$H = \omega_q a^\dagger a + \frac{\alpha}{2}a^\dagger a^\dagger aa. \tag{2.17}$$

Where $\omega_q = \sqrt{8E_JE_C} - E_C$,$\alpha = -E_C$. The Hamiltonian of the transmon looks like a harmonic oscillator with an additional anharmonicity term. High anharmonicity allows for precise control, while it introduces charge noise by decreasing $\frac{E_J}{E_C}$.

The calculation of E_c differs for different types of transmons. One type of transmon uses a single phase of collective charge at a circuit island by grounding one port of its Josephson junction[39]. The other uses the differential phase of collective charge at two islands by floating two pads of the qubit[40]. We name the two transmons the grounded transmon and the floating transmon, respectively.

The grounded transmon connects all the capacitors in parallel; therefore, its E_c is:

$$E_c = \frac{e^2}{2}(C_J + \Sigma_i C_i) \tag{2.18}$$

The floating qubit connects the other capacitors in series; therefore, its E_c is:

$$E_c = \frac{e^2}{2}(C_{shunt} + \frac{C_B C_T}{C_B + C_T}) \tag{2.19}$$

Where, C_{shunt} is the capacitance between two qubit pads. C_B and C_T are the single pad to ground capacitance. In a complex circuit, it can be expressed as

$$E_C = \frac{e^2}{2}\mathbf{d}^T\mathbf{C}_{\text{dyn}}^{-1}\mathbf{d}$$

d is the differential charge mode:

$$\mathbf{d} = \begin{pmatrix} 1 \\ -1 \\ 0 \end{pmatrix}$$

The node for the vector is (PadB,PadT,readout,...). C_{dyn} is the capacitance matrix.

Tuning the qubit frequency requires tuning of E_c and E_J. Usually, the maximum anharmonicity of the qubit ranges from 100 to 300 MHz. The qubit frequency can reach $3-6$ GHz[35].

The design goal of the qubit is to alter the frequency and anharmonicity within a feasible range to maximize coupling to the membrane while keeping the qubit decoherence rate in an acceptable value.

2.3 Device to enable coupling between membrane and superconducting circuit

After understanding the membrane and superconducting circuit, we look at packaging to couple those components. Ref.[41] demonstrates a capacitive readout of membrane movement using a voltage-biased membrane and transmon. The coupling scheme uses a parallel plate capacitor made with two parallel metal plates. One plate comes from the capacitor pad of the qubit. The other pad comes from the center pad of the membrane. If we bias the membrane pad with voltage, the oscillation of the membrane dynamically attracts the charge on the qubit pad. It converts the motion of the membrane to a charge and phase change on the qubit.

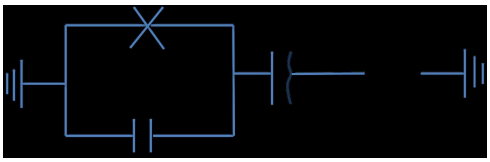

Figure 2.7: Simplified circuit diagram for a transmon coupling to membrane. The membrane is voltage biased at value of Vg, that drives the charge variation on the transmon circuit.

2.3.1 Parallel plate capacitance and motional modulation

The transduction rate from mechanical motion to charge can be derived from the capacitance equation for the parallel plate capacitor. The dependence on the area of the pads and the effective gap can be seen:

$$C = \frac{\epsilon A}{d + x} \tag{2.20}$$

where ϵ is the dielectric constant.A is the area of the center pad of the membrane. d represents the distance between the membrane and the qubit pad. The transduction from motion to capacitance is the gradient of C with respect to x :

$$\frac{dC}{dx} = -\frac{\epsilon A}{(d + x)^2} \tag{2.21}$$

When a constant voltage is applied, the change in capacitance is transduced into a change in charge.

$$\frac{dQ}{dx} = -\frac{\epsilon V_0 A}{(d + x)^2} \tag{2.22}$$

To increase the amount of charge number changed by a unit movement of the membrane, namely coupling g, larger pads and a smaller distance between the gaps are needed. Let's say that g is proportional to $\frac{dC}{dx}$, with a detailed proof in the next section. Eq.2.25 indicates the proportionality between C and A, C and the inverse of d^2, suggesting decreasing the gap distance and increasing the pad size for higher coupling. The amplitude of the applied bias voltage serves as a conversion prefactor between capacitance and charge, indicated by $Q = CV$.

Noting that we cannot tune the transduction to an arbitrary value because we need to maintain qubit anharmonicity and fabrication feasibility. Large pads provide a higher capacitance, which decreases E_c of the qubit. Low E_c indicates low anharmonicity , imposing challenges to quantum control. In addition, The smaller the distance between the membrane and the pad, the harder it is to fabricate precisely. The typical value of capacitance is 400 fF.

From an energy perspective, the presence of phonons shifts the frequency of the qubit mode. Assuming the coupling is much smaller than the energy difference between the qubit(GHz) and the mechanical resonator(20 kHZ), the phonon number has a cross-Kerr interaction with the qubit [41]:

$$H_{int} = (\hbar\omega_t - \lambda_m c^\dagger c)a^\dagger a \tag{2.23}$$

where $\lambda_m \simeq 8Ag^2\frac{\omega_m^2}{\omega_q^4}$. A, g, ω_m, ω_q represent the anharmonicity of the qubit, the coupling strength, the frequency of the resonator, and the frequency of the qubit. A large frequency gap limits the coupling of single phonons to the energy change of the membrane.

The above transduction assumes that all of the energy can be transferred to a single pad of a qubit through a parallel capacitor. However, this is not true for qubits such as transmons that work in differential mode, where the energy is not defined by a single pad. According to eq.2.19, the effective capacitance seen by the transmon when adding capacitance to one of the pads is reduced by a factor of $\frac{C_{T/B}}{C_B+C_T}$. We name this reduction factor β.

Rigorously, we have [42]:

$$\beta = \frac{\mathbf{d}^T\mathbf{C}_{\text{dyn}}^{-1}\mathbf{e}_B}{\mathbf{d}^T\mathbf{C}_{\text{dyn}}^{-1}\mathbf{d}} = C_\Sigma\left[(\mathbf{C}_{\text{dyn}}^{-1})_{BB} - (\mathbf{C}_{\text{dyn}}^{-1})_{BT}\right] \tag{2.24}$$

The reduction factor β is the effective transduction of $\frac{dC}{dX}$ to the actual differential mode if coupled to a single pad of the qubit. Therefore:

$$\frac{dC}{dx} = -\beta\frac{\epsilon A}{(d+x)^2} \tag{2.25}$$

One relation that will be useful later is:

$$\beta^2\frac{C_m}{C_\sum} = (\frac{C_T}{C_B+C_T})^2\cdot(\frac{C_m}{\frac{C_BC_T}{C_B+C_T}}) = \beta\frac{C_m}{C_B} \leq 1 \tag{2.26}$$

where C_m is the parallel plate capacitance, C_Σ is the total capacitance of the differential mode transmon.

2.3.2 Method to calculate coupling

Proved in chapter.3, the coupling strength can be expressed as:

$$\boxed{g = \beta \frac{V_g}{e} \frac{\partial C_g}{\partial x} \sqrt{\frac{E_C \omega_q}{2 m_{\text{eff}} \omega_m}}.} \tag{2.27}$$

where V_g is the pull-in voltage expressed as

$$V_{Pl} = \sqrt{\frac{8kd^3}{27\epsilon_o A}} \tag{2.28}$$

Calculation of the coupling requires a qubit simulation to get E_C, ω_q and β, a membrane simulation to get m_{eff}, ω_m and $\frac{\partial C_g}{\partial x}$, a definition of gap distance to obtain V_g. Instead of simulating the whole device, we adopt a theoretical approach: obtaining the parameters required for coupling calculation from the simulation and compositing them. The coupling is therefore the byproduct of those simulations.

The calculation of specific terms, like $\frac{\partial C_g}{\partial x}$ and E_C, uses a first-order-like estimation rather than the full simulation. For $\frac{\partial C_g}{\partial x}$, we integrate the eigenmode shape from the mechanics simulation to get an effective distance, thus giving an effective capacitance. Without electrostatic simulation, Electrostatic fringing-field effects and boundary-induced non-uniformities are omitted, but they are well known to alter the effective pull-in limits in compliant membrane capacitors[43]. For the extraction of E_C, we use a lumped-element framework to obtain the capacitance matrix and translate it to the energy of the circuit. However, the capacitance matrix fails to consider energy modulation like Kerr nonlinearities and dispersive shifts caused by geometry. The participation ratio method(EPR) is required to incorporate geometrically dependent full-wave distributed electromagnetic eigenmodes into the effective Hamiltonian parameters[44].

2.3.3 Flip-chip bonding of membrane and superconducting circuit

To define the distance between the membrane and the qubit, Flip-chip bonding is the technique. Flip chip bonding uses four micrometer level height pillars at the corners of the qubit chip to provide support. With special glue applied at the interface between the pillars and the two chips, the device is fastened, as well as the gap. The pillar provides good control over the distance of μm.

Although misalignment modulates the capacitance of the parallel plate capacitor, the influence on the capacitance can be calibrated. The effective capacitance value is $\frac{\epsilon_0 A}{d}$, where A is the projected area. If a 1 degree tilt occurs towards the membrane, A changes to $cos(1)A = 0.99985A$. d drops by $\frac{sin(1)L}{2} = 0.0087L$, where L is the length of the capacitor plate along the tilt direction. The capacitance, therefore, changes only slightly, indicating that misalignment is not harmful to such a device. Unless the tolerance induces the breakdown of the device, it can be accepted.

2.4 Conclusion

We have understood the basics of the membrane, transmon qubit, and packaging. We inspect the geometry of the hierarchical membrane, its frequency, and quality factor. We also know about the superconducting qubit and the parallel plate capacitor. Next, we will start deriving the hamiltonian of the system.

Chapter 3

Derivation of the electromechanical coupling Hamiltonian and feasibility of DSC regime

This chapter derives the coupling between a voltage-biased membrane and a superconducting charge circuit. The derivation proceeds in four steps. We first obtain the exact circuit Hamiltonian, then expand it about the static mechanical equilibrium, quantize the membrane and the superconducting mode, and finally determine how the electrostatic stability condition constrains the achievable coupling. Keeping these steps separate is useful because the membrane displacement enters the Hamiltonian through three distinct quantities: the gate capacitance $C_g(x)$, the offset charge $n_g(x)$, and the charging energy $E_C(x)$.

3.1 Exact circuit Hamiltonian

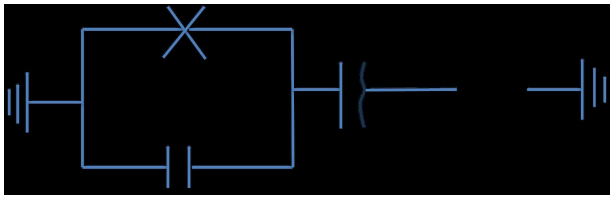

Figure 3.1: Simplified circuit model of the voltage-biased membrane coupled to a superconducting charge circuit.

Let x denote the physical displacement of the membrane, m_{eff} its effective mass, and ω_m its mechanical angular frequency in the absence of the dc electrostatic force. The superconducting island is described by the node flux Φ, with Josephson phase

$$\varphi = \frac{2\pi\Phi}{\Phi_0}. \tag{3.1}$$

The gate capacitor $C_g(x)$ connects the island to an ideal voltage source held at V_g. All capacitances that do not depend on displacement are collected into C_J. The Lagrangian is therefore

$$\mathcal{L} = \frac{m_{\text{eff}}\dot{x}^2}{2} - \frac{m_{\text{eff}}\omega_m^2 x^2}{2} + \frac{C_J\dot{\Phi}^2}{2} + \frac{C_g(x)}{2}\left(\dot{\Phi} - V_g\right)^2 + E_J\cos\varphi. \tag{3.2}$$

The canonical momenta are

$$p = \frac{\partial\mathcal{L}}{\partial\dot{x}} = m_{\text{eff}}\dot{x} \tag{3.3}$$

and

$$\begin{aligned} Q &= \frac{\partial \mathcal{L}}{\partial \dot{\Phi}} \\ &= C_J\dot{\Phi} + C_g(x)(\dot{\Phi} - V_g) \\ &= C_\Sigma(x)\dot{\Phi} - C_g(x)V_g, \end{aligned} \tag{3.4}$$

where

$$C_\Sigma(x) = C_J + C_g(x). \tag{3.5}$$

Solving Eq. (3.4) for the node voltage gives

$$\dot{\Phi} = \frac{Q + C_g(x)V_g}{C_\Sigma(x)}. \tag{3.6}$$

The Legendre transformation $H = Q\dot{\Phi} + p\dot{x} - \mathcal{L}$ then yields

$$H = \frac{p^2}{2m_{\text{eff}}} + \frac{m_{\text{eff}}\omega_m^2 x^2}{2} + \frac{\left[Q + C_g(x)V_g\right]^2}{2C_\Sigma(x)} - E_J\cos\varphi - \frac{C_g(x)V_g^2}{2}. \tag{3.7}$$

The last term is essential: it is the electrostatic potential appropriate to a capacitor connected to an ideal voltage source.

We now introduce the Cooper-pair-number operator $n = -Q/(2e)$, the charging energy

$$E_C(x) = \frac{e^2}{2C_\Sigma(x)}, \tag{3.8}$$

and the dimensionless gate charge

$$n_g(x) = \frac{C_g(x)V_g}{2e}. \tag{3.9}$$

Equation (3.7) becomes

$$\boxed{H = 4E_C(x)\left[n - n_g(x)\right]^2 - E_J\cos\varphi + \frac{p^2}{2m_{\text{eff}}} + \frac{m_{\text{eff}}\omega_m^2 x^2}{2} - \frac{C_g(x)V_g^2}{2}.} \tag{3.10}$$

3.2 Expansion about the mechanical equilibrium

We expand the gate capacitance about $x = 0$ using the convention

$$C_g(x) = C_0 + C_1 x + \frac{C_2}{2}x^2 + O(x^3), \tag{3.11}$$

so that $C_1 = (\partial C_g/\partial x)_0$ and $C_2 = (\partial^2 C_g/\partial x^2)_0$. The offset charge then has the expansion

$$\begin{aligned} n_g(x) &= n_{g0} + n_{g1}x + \frac{n_{g2}}{2}x^2 + O(x^3), \\ n_{g0} &= \frac{C_0V_g}{2e}, \qquad n_{g1} = \frac{C_1V_g}{2e}, \qquad n_{g2} = \frac{C_2V_g}{2e}. \end{aligned} \tag{3.12}$$

Similarly,

$$E_C(x) = E_{C0} + E_{C1}x + \frac{E_{C2}}{2}x^2 + O(x^3). \tag{3.13}$$

This notation makes the three displacement-dependent contributions explicit:

1. $n_g(x)$ produces the desired charge–displacement interaction;
2. $E_C(x)$ modulates the charging energy itself;
3. $-C_g(x)V_g^2/2$ produces a static force and an electrostatic spring shift.

To isolate the charge–displacement coupling, define $\widetilde{n} = n - n_{g0}$ and first approximate $E_C(x) \simeq E_C$. Expanding the charging term to second order gives

$$\begin{aligned} 4E_C\big[n - n_g(x)\big]^2 = 4E_C\widetilde{n}^2 - 8E_C n_{g1} x\widetilde{n} \\ + 4E_C n_{g1}^2 x^2 - 4E_C n_{g2} x^2\widetilde{n} + O(x^3). \end{aligned} \tag{3.14}$$

The leading interaction is therefore

$$H_{\text{int}} = -8E_C n_{g1} x\widetilde{n}. \tag{3.15}$$

The accompanying positive quadratic term,

$$H_{A^2} = 4E_C n_{g1}^2 x^2, \tag{3.16}$$

is the circuit analogue of an A^2 or diamagnetic term. It follows from the same square $4E_C[n - n_g(x)]^2$ that the linear coupling is produced.

The voltage-source term expands as

$$-\frac{C_g(x)V_g^2}{2} = -\frac{C_0 V_g^2}{2} - \frac{C_1 V_g^2}{2}x + O(x^3). \tag{3.17}$$

The constant term is irrelevant to coupling, and the linear term merely shifts the static equilibrium. The quadratic term changes the mechanical spring constant and is responsible for electrostatic softening and, eventually, pull-in.

If the displacement dependence of E_C is retained, the first-order Hamiltonian contains the additional term

$$H_{E_C}^{(1)} = 4E_{C1} x\widetilde{n}^2. \tag{3.18}$$

This interaction is physically distinct from Eq. (3.15); it can be neglected because its matrix elements is much smaller than the offset-charge coupling. The scale is roughly $\widetilde{n}/2n_{g1} \approx 10^{-11}$.

3.3 Quantization in the transmon regime

The mechanical displacement is quantized as

$$x = x_{\text{zpf}}(a + a^\dagger), \qquad x_{\text{zpf}} = \sqrt{\frac{\hbar}{2m_{\text{eff}}\omega_m}}. \tag{3.19}$$

It is convenient to define the zero-point modulation of the gate charge,

$$\eta \equiv n_{g1} x_{\text{zpf}} = \frac{V_g C_1 x_{\text{zpf}}}{2e}. \tag{3.20}$$

For $E_J/E_C \gg 1$, the transmon can be approximated by a weakly anharmonic oscillator,

$$H_q \simeq \hbar\omega_q b^\dagger b - \frac{E_C}{2} b^{\dagger 2} b^2, \tag{3.21}$$

with charge operator

$$\widetilde{n} \simeq i n_{\mathrm{zpf}}(b^\dagger - b), \qquad n_{\mathrm{zpf}} = \left(\frac{E_J}{32E_C}\right)^{1/4}. \tag{3.22}$$

The approximate transmon relation

$$n_{\mathrm{zpf}}^2 = \frac{\hbar\omega_q}{16E_C} \tag{3.23}$$

will be useful below.

Substitution of Eqs. (3.19) and (3.22) into Eq. (3.15) gives

$$H_{\mathrm{int}} = -i\hbar g(a + a^\dagger)(b^\dagger - b), \tag{3.24}$$

where

$$\boxed{g = \frac{8E_C}{\hbar}\,\eta n_{\mathrm{zpf}} = \frac{4E_C}{e\hbar} V_g C_1 x_{\mathrm{zpf}} n_{\mathrm{zpf}}.} \tag{3.25}$$

Here g is an angular frequency. Using Eq. (3.23), it may also be written as

$$\boxed{g = \frac{V_g}{e}\frac{\partial C_g}{\partial x}\sqrt{\frac{E_C\omega_q}{2m_{\mathrm{eff}}\omega_m}}.} \tag{3.26}$$

With the reduction ratio β considered, using Eq. (2.25), we have:

$$\boxed{g = \beta\frac{V_g}{e}\frac{\partial C_g}{\partial x}\sqrt{\frac{E_C\omega_q}{2m_{\mathrm{eff}}\omega_m}}.} \tag{3.27}$$

In the following discussion, we assume $\beta = 1$.

3.3.1 The quadratic term and oscillator squeezing

Introduce dimensionless mechanical quadratures

$$X = \frac{a + a^\dagger}{\sqrt{2}}, \qquad P = \frac{i(a^\dagger - a)}{\sqrt{2}}. \tag{3.28}$$

The bare mechanical Hamiltonian and the quadratic charging term are

$$\begin{aligned} H_m + H_{A^2} &= \frac{\hbar\omega_m}{2}(P^2 + X^2) + 8E_C\eta^2 X^2 \\ &= \frac{\hbar}{2}\left[\omega_m P^2 + (\omega_m + D)X^2\right], \end{aligned} \tag{3.29}$$

where

$$D = \frac{16E_C\eta^2}{\hbar}. \tag{3.30}$$

The corresponding squeezed frequency is

$$\Omega_m = \sqrt{\omega_m(\omega_m + D)}. \tag{3.31}$$

With the canonical rescaling

$$X = sX_\Omega, \qquad P = \frac{P_\Omega}{s}, \qquad s = \sqrt{\frac{\omega_m}{\Omega_m}}, \tag{3.32}$$

Eq. (3.29) takes the standard form

$$H_m + H_{A^2} = \frac{\hbar\Omega_m}{2}\left(P_\Omega^2 + X_\Omega^2\right), \tag{3.33}$$

and the coupling becomes $g_\Omega = gs$.

3.3.2 Adiabatic response of the transmon

Because $\omega_m \ll \omega_q$, the qubit may be treated in the Born–Oppenheimer approximation: for each slowly varying value of X_Ω, the qubit remains in its instantaneous ground state. In the harmonic-transmon approximation, second-order perturbation theory gives

$$\Delta E_{q,0}^{(2)}(X_\Omega) = -\frac{2\hbar(gs)^2}{\omega_q} X_\Omega^2. \tag{3.34}$$

The effective mechanical Hamiltonian is consequently

$$H_{m,\mathrm{eff}} = \frac{\hbar}{2}\left[\Omega_m P_\Omega^2 + \left(\Omega_m - \frac{4g^2s^2}{\omega_q}\right) X_\Omega^2\right]. \tag{3.35}$$

Equations (3.25), (3.23), and (3.30) imply

$$\frac{4g^2}{\omega_q} = D. \tag{3.36}$$

The coefficient of X_Ω^2 therefore reduces to

$$\begin{aligned} \Omega_m - \frac{4g^2s^2}{\omega_q} &= \Omega_m - D\frac{\omega_m}{\Omega_m} \\ &= \frac{\omega_m^2}{\Omega_m}. \end{aligned} \tag{3.37}$$

Since the physical oscillator frequency is the square root of the product of the two quadrature coefficients, Eq. (3.35) gives

$$\omega_{m,\mathrm{eff}} = \sqrt{\Omega_m \frac{\omega_m^2}{\Omega_m}} = \omega_m. \tag{3.38}$$

Thus, within the harmonic-transmon and adiabatic approximations, the positive A^2 term cancels the softening produced by virtual qubit excitation. This statement applies only to the offset-charge part of the Hamiltonian. It does not cancel the fixed-voltage spring shift in Eq. (3.17), the modulation of $E_C(x)$, or corrections due to transmon anharmonicity and higher levels.

If the A^2 term were omitted, the quadratic coefficient in Eq. (3.35) would vanish at

$$g_c = \frac{1}{2}\sqrt{\omega_q \omega_m}. \tag{3.39}$$

Equation (3.39) is a soft-mode instability threshold of the A^2-free bilinear model. It should not be identified with the general definition of the deep-strong-coupling regime, which instead requires g to be comparable to one or both bare subsystem frequencies.

3.3.3 Comment on gauge and Hilbert-space truncation

Gauge choice and Hilbert-space truncation are separate issues. Before a finite-level truncation, unitary transformations between equivalent circuit representations leave physical predictions unchanged. After truncation, however, nominally equivalent representations can produce different results. Yoshihara *et al.* show this explicitly for a flux-qubit–LC circuit: the inductive representation admits a useful two-level Rabi description, whereas a naively truncated capacitively transformed Hamiltonian does not [45]. The present calculation therefore starts from the full node-charge Hamiltonian in Eq. (3.10); a two-level approximation should be used only after its convergence against additional transmon levels has been checked.

3.4 Pull-in limit for a parallel-plate membrane

To show how the pull-in limits can be derived from the hamiltonian eq.3.10, we can take the effective potential energy under adiabatic approximation of qubit:

$$U_{eff} = \frac{1}{2}kx^2 + E_{q,0}(x) - \frac{C_g(x)V_g^2}{2} \tag{3.40}$$

$E_{q,0}(x)$ is the ground state energy for qubit, which can be ignored. The pull-in limits fulfill the following:

$$\frac{\partial U}{\partial x} = 0 \qquad \frac{\partial^2 U}{\partial x^2} = 0 \tag{3.41}$$

To calculate the pull-in limits, we abandon the linearization of C_g around d, rather, we assign C_g as:

$$C_g(x) = \frac{\epsilon_0 A}{d - x} \tag{3.42}$$

With 3.41 as the condition to solve we have:

$$x_{Pl} = \frac{d}{3} \qquad V_{Pl} = \sqrt{\frac{8kd^3}{27\epsilon_o A}} \tag{3.43}$$

We now estimate the largest coupling permitted by electrostatic stability. For a single-sided parallel-plate capacitor with undeformed gap d, area A, and zero-displacement capacitance

$$C_m = \frac{\epsilon_0 A}{d}, \tag{3.44}$$

the first derivative at $x = 0$ is

$$C_1 = \frac{C_m}{d}. \tag{3.45}$$

The static pull-in voltage is

$$V_{\mathrm{PI}} = \sqrt{\frac{8kd^3}{27\epsilon_0 A}} = \sqrt{\frac{8m_{\mathrm{eff}}\omega_m^2 d^2}{27C_m}}, \tag{3.46}$$

where $k = m_{\mathrm{eff}}\omega_m^2$.

Combining Eqs. (3.26) and (3.46), and using the standard convention $E_C = e^2/(2C_\Sigma)$, gives

$$\boxed{g \le g_{\mathrm{PI}}^{(\mathrm{tr})} = \sqrt{\frac{2C_m}{27C_\Sigma}}\sqrt{\omega_q\omega_m}.} \tag{3.47}$$

Relative to the A^2-free soft-mode threshold in Eq. (3.39),

$$\frac{g_{\mathrm{PI}}^{(\mathrm{tr})}}{g_c} = \sqrt{\frac{8C_m}{27C_\Sigma}} < \sqrt{\frac{8}{27}} \simeq 0.544. \tag{3.48}$$

Consider β:

$$\frac{g_{\mathrm{PI}}^{(\mathrm{tr})}}{g_c} = \sqrt{\frac{8C_m\beta^2}{27C_\Sigma}} \tag{3.49}$$

The pull-in constraint, therefore, prevents a single parallel-plate transmon device from reaching this instability threshold even before the stabilizing A^2 term is included. Differential electrodes, non-parallel geometries, and tension-induced nonlinearities require a separate stability analysis and need not obey Eq. (3.47) with the same numerical prefactor.

3.5 Cooper-pair-box regime

The same circuit behaves differently in the Cooper-pair-box (CPB) regime, where charge dispersion is not exponentially suppressed. Near the degeneracy point $n_g = N + 1/2$, retain the two charge states $|N\rangle$ and $|N+1\rangle$. Up to an irrelevant common energy, their Hamiltonian is

$$H_{\mathrm{CPB}} = \frac{\epsilon}{2}\sigma_z - \frac{E_J}{2}\sigma_x, \qquad \epsilon = 8E_C\left(N + \frac{1}{2} - n_g\right). \tag{3.50}$$

At the bias point, a small displacement produces

$$\delta n_g = \frac{V_g C_1}{2e} x_{\mathrm{zpf}}(a + a^\dagger). \tag{3.51}$$

and we define the zero-point gate-charge modulation

$$\eta = n_{g1} x_{\mathrm{zpf}} = \frac{V_g}{2e}\left.\frac{\partial C_g}{\partial x}\right|_0 x_{\mathrm{zpf}}. \tag{3.52}$$

Consequently,

$$H_{\mathrm{int}}^{(\mathrm{CPB})} = -\hbar g_{\mathrm{CPB}}\sigma_z(a + a^\dagger), \tag{3.53}$$

where the overall sign depends on the definition of σ_z, and

$$\boxed{g_{\mathrm{CPB}} = \frac{2E_C}{e\hbar} V_g C_1 x_{\mathrm{zpf}}} = 4\frac{E_C \eta}{\hbar} \tag{3.54}$$

At exact charge degeneracy the energy eigenbasis is rotated by $\pi/2$, so this longitudinal charge-basis interaction becomes transverse in the qubit energy basis.

For a parallel-plate capacitor, $C_1 = C_m/d$. If the same capacitor also sets the bias point,

$$\frac{C_m V_g}{2e} = N + \frac{1}{2}, \tag{3.55}$$

then Eq. (3.54) reduces to

$$\boxed{g_{\mathrm{CPB}} = \frac{2E_C x_{\mathrm{zpf}}}{\hbar d}(2N+1).} \tag{3.56}$$

This has the same charge-state-dependent structure as the electromechanical coupling used by Martinetz *et al.* for a nanoparticle coupled to a CPB [23].

Applying the pull-in bound in Eq. (3.46) to Eq. (3.54) gives

$$\boxed{g_{\mathrm{CPB}} \le g_{\mathrm{PI}}^{(\mathrm{CPB})} = \frac{2e}{C_\Sigma}\sqrt{\frac{C_m\omega_m}{27\hbar}}.} \tag{3.57}$$

For comparison with the A^2-free threshold in Eq. (3.39), the condition $g_{\mathrm{PI}}^{(\mathrm{CPB})} \ge g_c$ becomes

$$\boxed{\omega_q \le \frac{16e^2 C_m}{27 C_\Sigma^2 \hbar}.} \tag{3.58}$$

At the CPB degeneracy point, $\hbar\omega_q \simeq E_J$. For $C_\Sigma = 3.1\,\mathrm{fF}$ and $C_m = 3.0\,\mathrm{fF}$, Eq. (3.58) gives

$$\frac{\omega_q}{2\pi} \lesssim 7.17\,\mathrm{GHz}, \tag{3.59}$$

while $E_C/h \simeq 6.25\,\mathrm{GHz}$. Therefore, a reported device with $E_J/h = 6.15\,\mathrm{GHz}$ does cross this particular threshold under the single-sided parallel-plate assumptions [46].

3.5.1 Why the CPB differs from the transmon

The distinction can be seen directly from the qubit ground-state energy as a function of gate charge. In the two-charge-state approximation, let $\delta n_g = n_g - (N + 1/2)$. Including the common charging-energy contribution, the CPB ground energy is

$$E_g^{(\mathrm{CPB})}(\delta n_g) = E_C + 4E_C\delta n_g^2 - \frac{1}{2}\sqrt{E_J^2 + (8E_C\delta n_g)^2}. \tag{3.60}$$

Near the degeneracy point,

$$E_g^{(\mathrm{CPB})} = \mathrm{const.} + \left(4E_C - \frac{16E_C^2}{E_J}\right)\delta n_g^2 + O(\delta n_g^4). \tag{3.61}$$

The first contribution in parentheses is the positive A^2 term, whereas the second is the softening caused by virtual qubit excitation. In the CPB regime, $E_J < 4E_C$ can make the total curvature negative, so the cancellation is incomplete. In contrast, the transmon ground band is exponentially flat as a function of n_g; its positive and negative contributions cancel to high accuracy in the harmonic limit. Figure 3.2 illustrates this physical difference.

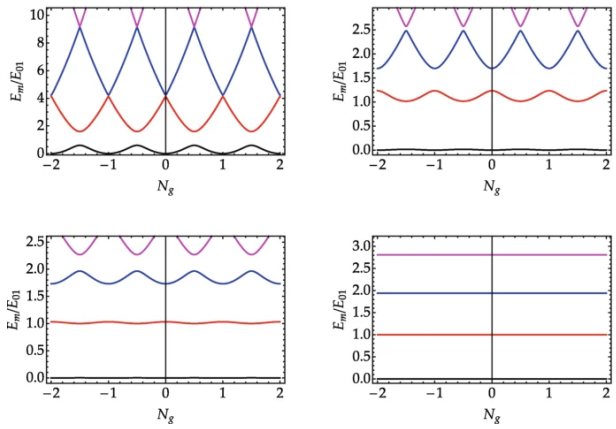

Figure 3.2: Qubit energy as a function of offset charge. The transmon is nearly insensitive to n_g, whereas the CPB retains appreciable charge dispersion and can therefore exert a displacement-dependent force.

Equation (3.61), rather than the A^2-free criterion alone, is the appropriate starting point for a quantitative CPB stability calculation. The complete analysis should also retain the voltage-source contribution in Eq. (3.17) and the full nonlinear capacitance $C_g(x)$.

3.6 Feasibility to enter DSC region by negative curvature of CPB ground stage

Using $n_g = n_{g0} + \eta(a + a^\dagger)$ where η is defined in (3.52), the charging term becomes

$$\begin{aligned} 4E_C\left[n - n_g\right]^2 = 4E_C(n - n_{g0})^2 \\ - 8E_C\eta(n - n_{g0})(a + a^\dagger) \\ + 4E_C\eta^2(a + a^\dagger)^2. \end{aligned} \tag{3.62}$$

At the degeneracy point, $n - n_{g0} = \sigma_z/2$ in the two-charge-state subspace. After rotating into the qubit energy basis, the Hamiltonian becomes

$$\boxed{\begin{aligned} H = \hbar\omega_m a^\dagger a - \frac{\hbar\omega_q}{2}\tau_z - \hbar g\,\tau_x(a + a^\dagger) \\ + \hbar D(a + a^\dagger)^2, \end{aligned}} \tag{3.63}$$

where

$$\hbar\omega_q = E_J, \qquad g = \frac{4E_C\eta}{\hbar}, \qquad D = \frac{4E_C\eta^2}{\hbar}. \tag{3.64}$$

The coupling and quadratic coefficient are not independent:

$$\boxed{D = \frac{\hbar g^2}{4E_C}.} \tag{3.65}$$

For a slowly varying oscillator coordinate $q = a + a^\dagger$, the qubit ground energy is

$$\begin{aligned} E_{q,0}(q) &= -\frac{1}{2}\sqrt{E_J^2 + 4\hbar^2 g^2 q^2} \\ &= -\frac{E_J}{2} - \frac{\hbar g^2}{\omega_q}q^2 + O(q^4). \end{aligned} \tag{3.66}$$

Adding the explicit quadratic term gives the net correction

$$\Delta H^{(2)} = \hbar\left(D - \frac{g^2}{\omega_q}\right)(a + a^\dagger)^2. \tag{3.67}$$

Using Eq. (3.65),

$$\boxed{D - \frac{g^2}{\omega_q} = g^2\left(\frac{\hbar}{4E_C} - \frac{1}{\omega_q}\right).} \tag{3.68}$$

This coefficient is negative precisely when $E_J < 4E_C$, in agreement with the charge-band-curvature derivation. Notice that for CPB, D represented the A^2 term hardening effect and the linear coupling softening $\frac{g^2}{\omega_q}$ can not cancel each other. The true DSC region could be entered for CPB coupling to membrane.

Introduce dimensionless quadratures

$$X = \frac{a + a^\dagger}{\sqrt{2}}, \qquad P = \frac{i(a^\dagger - a)}{\sqrt{2}}. \tag{3.69}$$

The locally renormalized oscillator Hamiltonian is

$$H_{m,\text{eff}} = \frac{\hbar}{2}\left[\omega_m P^2 + \left(\omega_m + 4D - \frac{4g^2}{\omega_q}\right) X^2\right]. \tag{3.70}$$

The corresponding local mode frequency is

$$\boxed{\omega_{m,\text{eff}}^2 = \omega_m \left(\omega_m + 4D - \frac{4g^2}{\omega_q}\right).} \tag{3.71}$$

Defining $\omega_C = E_C/\hbar$, this can be written as

$$\omega_{m,\text{eff}}^2 = \omega_m \left(\omega_m + \frac{g^2}{\omega_C} - \frac{4g^2}{\omega_q}\right). \tag{3.72}$$

3.6.1 Soft-mode threshold including the A^2 term

The central equilibrium loses local stability when $\omega_{m,\text{eff}}^2 = 0$. If $E_J < 4E_C$, the critical coupling is

$$\boxed{g_c'^2 = \frac{\omega_m \omega_q}{4\,(1 - E_J/(4E_C))}.} \tag{3.73}$$

Equivalently, for the normalized Rabi coupling

$$\lambda = \frac{2g}{\sqrt{\omega_m \omega_q}}, \tag{3.74}$$

the critical prefactor is

$$\boxed{\lambda_c = \frac{1}{\sqrt{1 - E_J/(4E_C)}} > 1.} \tag{3.75}$$

The A^2 term therefore raises the threshold relative to the A^2-free value $g_c = \sqrt{\omega_m \omega_q}/2$, but it does not make the threshold unreachable within the ideal two-state CPB model.

3.6.2 Parameter bound for entering DSC region before reaching pull-in limits

To make the critical coupling below the pull-in limits, the critical coupling g' (3.73) should be smaller than the pull-in coupling $g_{PI}^{(CPB)}$ (3.57). Using $r = \frac{C_m}{C_\Sigma}$, this requires:

$$\boxed{\frac{E_J}{E_C} < \frac{32r}{27 + 8r}.} \tag{3.76}$$

For r $= \frac{3fF}{3.1fF} = 0.968$, $\frac{E_J}{E_C} < \frac{32r}{27+8r} = 0.89$. For $E_c/\hbar = 6.25$GHZ , $E_J/\hbar < 5.56$GHZ

3.6.3 Hypothesis: extension to flux-sensitive circuits

An analogous Born–Oppenheimer argument can be applied to a flux-sensitive qubit such as fluxonium: the mechanical spring is modified by the curvature of the qubit ground-state energy with respect to the mechanically modulated flux. A sufficiently large negative curvature would produce softening. However, this conclusion requires a separate inductive circuit derivation; it does not follow from the capacitive Hamiltonian in Eq. (3.10).

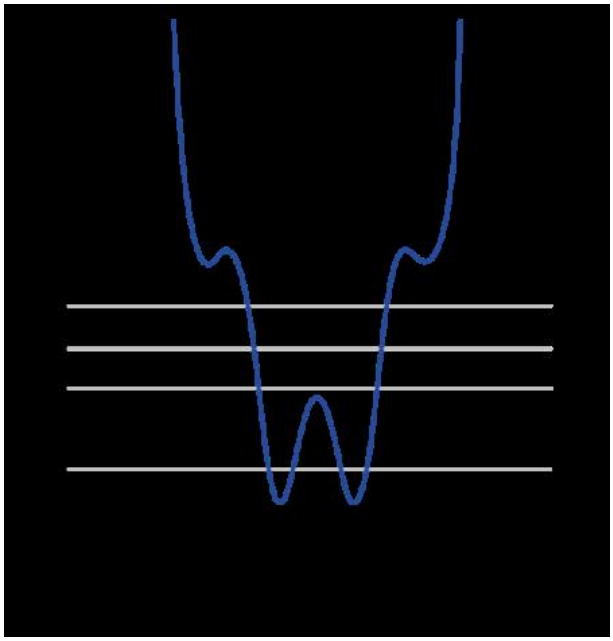

Figure 3.3: Schematic dependence of fluxonium energy levels on external flux. The relevant electromechanical response is determined by the curvature of the appropriate dressed energy band.

3.7 Summary

The voltage-biased gate capacitor produces the exact charging term $4E_C(x)[n - n_g(x)]^2$. Its first-order expansion gives the desired linear charge–displacement coupling, while the same square necessarily generates a positive quadratic A^2 term. For an anharmonic transmon in the adiabatic limit, the A^2 term cancels the mechanical softening caused by virtual qubit excitation. The remaining mechanical response comes from the fixed-voltage electrostatic potential, the displacement dependence of $E_C(x)$, transmon anharmonicity, and higher-level corrections. Moreover, a single parallel-plate capacitor is constrained by pull-in before it reaches the soft-mode threshold of the A^2-free model. A CPB can retain negative charge-band curvature and therefore behaves differently. The DSC region seems to be feasible to reach before the pull-in limits when E_J/E_C is smaller than certain value. But its accessible regime must be assessed using the full band curvature and the same electrostatic stability constraint.

Chapter 4

Results and discussion

This chapter presents and discusses the design of a membrane-transmon device through the simulation and experiment of a membrane, as an example of device design towards the DSC regime. Four simulations were conducted to investigate the parameters to check the DSC feasibility: the mechanics of the pure wheel membrane with a larger center pad, the mechanics of the metallized wheel membrane, the capacitance of the transmon qubit, and the coupling for the designed membrane-qubit device. To verify the process of metallization on the membrane, the mechanical spectrum of three lotus-shaped membranes was measured before and after metallization.

The simulation of a pure membrane provides an initial estimation of coupling strength and buckling. It has a fundamental frequency of 26.6 kHz, a quality factor of 8e7, and an effective mass of 64.75 ng. By assuming the parameters of the qubit and packaging, we found that the DSC regime is not reachable. The buckling analysis indicates that the region near the joint on the wheel part of the membrane experiences at most -8e5 Pa of compressive stress, showing a low buckling risk.

To improve coupling strength, we perform bayesian optimization of the geometry for the 70 nm thick wheel membrane without metallization. The optimizer yields a square-shaped membrane that shows a 1.58 times improvement in the objective function $Q \cdot g$. However, the improvement is primarily due to the increase in the quality factor from 1e8 to 1.5e8. The buckling of the optimized design has not yet been fully studied due to limited time. Thus, we do not adopt the optimized membrane in the final membrane-transmon design.

The simulation of metallization corrects the estimation and produces the membrane geometry used for the final coupling calculation. The 100 nm thick wheel membrane is metallized with a 10-70 nm thick al layer. For a 30 nm deposition of 0 stress Al, the frequency decreases from 26.6 to 22.6 kHz. The quality factor decreases from 8e7 to 3.3e7. The residual stress causes the membrane to bend 0.83 microns toward the qubit in the center region for a 50 nm thick deposition at 300 MPa. To compensate, the fabrication process demands a residual stress of Al around -300 Mpa at room temperature.

Next, we simulate the coupling capacitance between membranes and different pads of the qubit to calculate E_C for the coupling calculation. The capacitance contribution is dominated by the capacitance of the membrane-qubit pad, with a value of 567 fF. Assuming that the voltage biased membrane only has capacitance coupling to one pad of the qubit, The E_C is estimated to be 112.7 MHz. We leave the Josephson energy as a variable to meet the designed qubit frequency requirement of 4 GHz.

Lastly, we calculate the achievable coupling strength, assuming the voltage is biased at 80% of the pull-in voltage limits and the qubit chip to membrane chip distance is 2.5 μm. We reached a coupling of 0.775 MHz for the fundamental mode of a 30 nm Al deposited wheel

membrane with effective mass, frequency, and quality factor of 78.9 ng , 23.7 kHz, and 1.05e8 at 10 mK. At 80% pull-in limits, This converts to 16% of the DSC critical value, far below the theoretical pull-in threshold of 35.9%. The difference comes from the coupling reduction when single mode driving is applied to a differential mode transmon. By using a grounded transmon or a differential membrane, The reduction can be avoided. The coupling strength should reach the theoretical value of 1.74 MHz.

The simulation methods are shown in the appendix.B. The simulation results for the diagonal membrane and the square membrane are included in the appendix.C.

4.1 Parameters of the final device

This section shows the geometry and parameters of the final qubit-transmon device, providing a summary of the main results of this thesis.

We demonstrate a proposal for the physical realization of the capacitive coupling membrane-qubit device in fig.4.1. The membrane, fabricated on a separate chip, was flip-chip bonded on top of one pad of the qubit, enabling capacitive coupling. To enhance the electric connectivity of the membrane while maintaining small parasitic capacitance, the membrane is partially metallized and tilted at a 45 degree angle. The DC biasing of the membrane is achieved by a large coupling pad, avoiding wire-bonding. To allow precise bonding locations without overlapping with the port of the feedline, the size of the membrane chip is set to 8 mm.

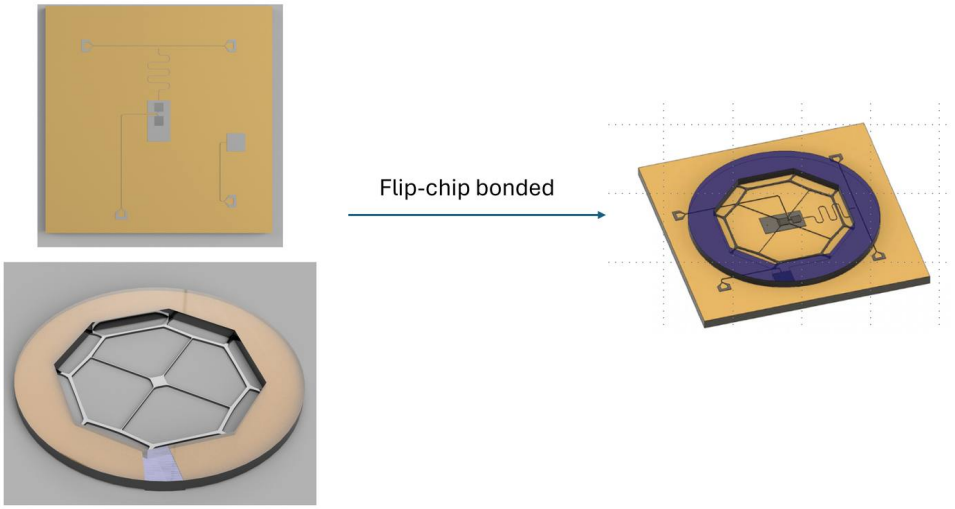

Figure 4.1: Left: (top) The transmon qubit chip where the center region indicate the qubit. The gray area indicates the feedline and the coupling pad that biased voltage applied.(bottom) The wheel membrane chip with diameter of 8 mm and hollow radius of 5mm. For simplicity, all the wheel membrane is depicted with a metal appearance, but only the side facing qubit will be metallized. Right: The flip-chip bonded device with membrane on top of the qubit. The membrane is inverted and is located at 2.5 μm right above the qubit pad.

Table.4.1 compiles the physical and operational parameters from multiple simulations. Taken together, we are able to reach a coupling of 0.775 MHz using a 23.7 kHz, $1.05 \cdot 10^8$ quality factor membrane and a 4 GHz, 112.7 MHz anharmonicity qubit. The critical coupling strength is 4.86 MHz, suggesting that the DSC regime is not reachable with this design.

Wheel membrane couple to transmon

Parameter	Description	Value
	Membrane	
-	Membrane geometry	wheel membrane
-	Membrane substrate material	100 nm Si_3N_4
$h1$	Membrane metallized layer thickness	30 nm Al e-beam deposited
σ_{Al}	metallized stress	-300 Mpa (298k) 0 Mpa (10mk)
$\frac{\omega_m}{2\pi}$	Membrane frequency without al	26.62 kHz
$\frac{\omega_m}{2\pi}$	Membrane frequency with al	22.62 kHz (298k) 23.70 kHz (10mk)
m_{phy}	Membrane physical mass	620 ng (without al) 783 ng (with al)
m_{eff}	Membrane effective mass	62.7 ng (without al), 78.9 ng (with al)
x_{zpf}	Position zero point fluctuation	5.43 fm (298k) 5.33 fm (10mk)
Q_i	Membrane quality factor before metallization	$8.07 \cdot 10^7$
Q_{al}	Membrane quality factor after metallization	$3.32 \cdot 10^7$(298k) $1.05 \cdot 10^8$(10mk)
$r0$	Fillet length	2 μm and 50 μm
$w0$	First tether Width	15 μm
$w1$	Second tether width	107.5 μm
$w2$	Third tether width	151.7 μm
w_b	Bridge tether width	114.8 μm
$l0$	First tether length	2.28 mm
$l1$	Second tether length	1.03 mm
$l2$	Third tether length	0.4762 mm
lb	Bridge tether length	1.880 mm
A	Pad area	0.4 mm $\cdot$ 0.4 mm
θ	Angle	86^o
	Qubit	
$\frac{E_c}{\hbar}$	Qubit charging frequency	112.7 MHz
ω_q	Qubit frequency	4 GHz
$\frac{E_J}{\hbar}$	Qubit Josephson Frequency	18.76 GHz
	Coupling	
d_{gap}	Distance between membrane and qubit	2.5 μm
C_m	Membrane qubit capacitance	567 fF
C'_m	Membrane qubit capacitance gradient	$2.20 \cdot 10^{-7}$ F/m
C_{shunt}	Qubit shunt capacitance	16 fF
C_B	Qubit ground capacitance	789 fF
g_t	Couple strength with grounded qubit	1.721 MHz (298k) 1.728 MHz (10mk)
g	Couple strength with floating qubit	0.772 MHz (298k) 0.775 MHz (10mk)
g_c	DSC coupling strength	4.75 MHz (298k) 4.86 MHz (10mk)
β	Coupling reduction	0.207
	LC readout [chap.5]	
-	Resonator type	Loop gap resonator
-	Resonator material	Niobium on top of silicon
ω_{lc}	LC resonator frequency	2.73 GHz
g_{lc}	Transduction for optomechanical coupling	1.12 MHz/nm

Table 4.1: The table of parameters extracted from simulation that includes: the geometrical and physical parameters of the membrane, the physical parameters for the qubit, the coupling parameters and the parameters for the LC resonator readout.

The simulated coupling strength g agrees with the theoretical limits set in the last chapter, reassuring us that the coupling is pull-in limited. In the simulation, g is 0.775 MHz, which is 0.163 of g_c. Theoretically, the requirement of 80% pull-in voltage sets g as $0.8 \cdot \sqrt{\frac{8}{27}\beta\frac{C_m}{C_B}} = 0.16795$ of g_c, according to Eq.(3.49) and Eq.(2.26). The difference is caused by the mismatch of C_m(567 fF) used to calculate pull-in voltage and the one(550 fF) used to calculate $\frac{dC}{dx}$. With this mismatch modified, $g = 0.168$ is almost the same as the theoretical value 0.16795.

However, this agreement should not be viewed as a separate verification of the theory. The calculation of coupling derives from Eq.(3.49) with parameters extracted from various simulations. The agreement is expected, proving that the simulation of device parameters is reasonable.

The design of the qubit circuit alters coupling. If we switch the floating qubit to the grounded qubit, the coupling increases from 0.775 MHz to 1.728 MHz. This is because the coupling reduction is removed when coupled to the ground transmon. This converts into a trade-off on E_C. The capacitance seen from the grounded qubit is the summation of all the capacitances. With a giant capacitance added, the capacitance increases, thus dropping anharmonicity to only 24 MHz.

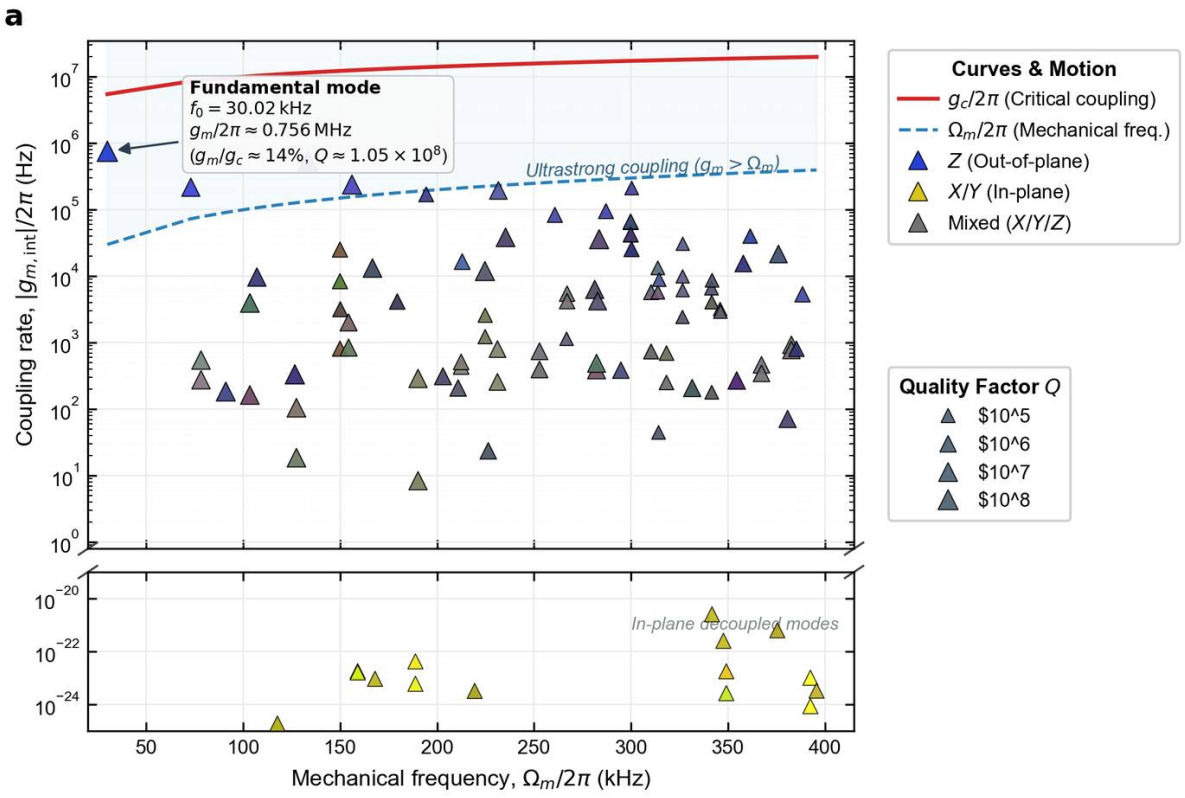

Figure 4.2: Membrane coupling-eigenfrequency plot before metallization. The size of the dot represents the quality factor of the deflection mode. The color represents the dominate oscillation mode. The blue dashline is the traditional ultrastrong coupling value $g = \omega_m$, while the read line is the DSC regime $g = 1/2\sqrt{\omega_m\omega_q}$. The highest coupled mode is the fundamental mode, with frequency of 30.02 kHz and couplinge strength of 0.756 MHz. The color correlates the coupling strength. Only blue color modes, dominated by our-of-plane motion, obtains high coupling strength.

4.1.1 Membrane eigenfrequencies

We simulate the mechanical eigen-frequencies of the 1.1 GPa prestressed 100 nm thick membrane with the membrane geometry shown in the appendix.C.1. The result is plotted in fig.4.2. We read the x-axis only to analyze its mode distribution first. The fundamental mode has a frequency of 30.02 kHz, while the second and third modes have frequencies of 73.06 kHz and 78.31 kHz, respectively. Other Higher-order modes exist, while the separation between modes is not uniform, indicating that a free spectrum range does not exist here. This is caused by soft-clamping, which loosens the boundary conditions and allows in-plane modes with different dynamics.

To estimate the possible interaction landscape for different modes, we calculate its coupling. The calculation of coupling assumes $E_C = 112.7$MHz, $\omega_q = 4$GHz, $V = 1.5$V, and $d_{gap} = 2.5\mu$m. The goal is to qualitatively understand the coupling contribution of different modes. We read the y-axis together with the x-axis only in Fig.4.2.

Among all the modes that couple, only the fundamental mode needs consideration. In Fig.4.2, there are three modes that are above the ultrastong coupling($g > \omega_m$), while there are no modes above the critical coupling. The highest coupling strength comes from the fundamental mode. It is at least a factor of 3 greater than all the other modes. Also, the critical coupling strength scales with $\sqrt{\omega_m}$. The distance to the critical coupling value increases for higher order modes. Together, Only the fundamental mode is strong enough. In the following simulation, we focus only on the fundamental modes.

The mode shape of the membrane determines the coupling strength. Most of the motion with out-of-plane movement, denoted by the blue color in the plot, has a higher coupling than the other colors. For modes that ultrastrongly couple, only the blue color exists. The dominance of the blue color indicates that higher coupling favors the deflection motion. This can be understood by inspecting dC/dx for different modes. For the deflection only mode that is symmetric, the motion contributes to a change in capacitance, while for the mode that is anti-symmetric, the capacitance changes almost cancel each other. The deflection module capacitance is weaker for the mixed mode and diminishes for the in-plane-only mode.

The dependence of the quality factor on coupling and modes is unclear from the plot. The High quality factor mode distributes randomly among the modes and coupling strength. This may suggest that an increasing quality factor can be achieved without changing coupling and frequency constraints. A detailed understanding of quality factor dependence requires measurement of the curvature and surface gradient of each mode.

4.1.2 Membrane optimization result

To improve the coupling and quality factor, we use a Bayesian optimizer to generate design candidates with different membrane geometries. we optimize the product of the quality factor and the coupling by changing the length, angle, width, and filet radius of the membrane. We set a total of 80 rounds of optimization. The first 30 rounds collect data to create the surrogate model. After that, the optimizer consistently finds its best candidates and tests them in the FEM software. The design with the highest objective value was chosen as the final design. The implementation details can be found in the appendix.B.3.

Present in the figure.4.3, we obtain a 58% improvement in the product of the coupling and quality factor by changing the membrane geometry. We reach a square-membrane of 23 kHz in frequency, $1.53 \cdot 10^8$ in quality factor, 46.8 ng in effective mass. The objective function is

improved by 58%, primarily due to the quality factor changing from $1.04 \cdot 10^8$ to $1.53 \cdot 10^8$. The coupling is also slightly improved by 7%.

One explanation for the resulting square shape is that a longer tether length promotes larger curvature dilution, thus increasing the quality factor. The main contributor to loss in the simulation is the bending loss caused by the curvature near the clamping point. For the same value of deflection, a longer tether decreases the tilt angle between the tether and the horizontal plane. The curvature at the clamping point is therefore reduced, leading to an increase in the quality factor. By offsetting the clamping point diagonally away from the center pad, the tether length increases. The resulting geometry is a square shape. In the coupling size, one can maintain the coupling to be the same by fixing $m_{eff}\omega_m$.

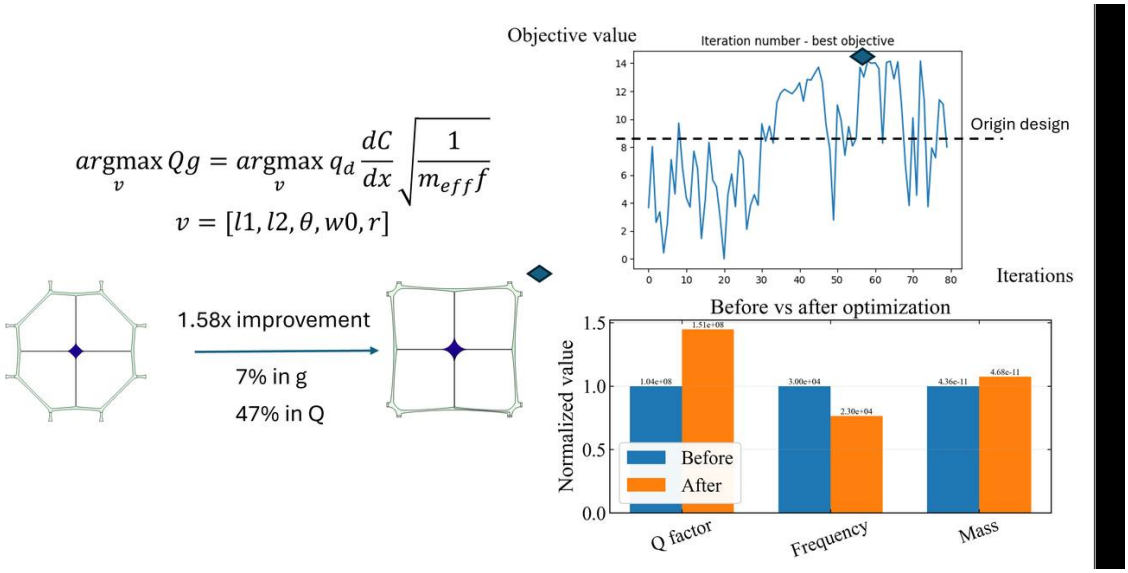

Figure 4.3: Left: optimization objective function and the change in membrane geometry. The optimizor maximizes the objective function by tuning a combination of second tether length, third tether length, width of the first tether, angle and the fillet length. The wheel membrane evolves to the square membrane with 7% and 47% improvement in coupling and quality factor. Right: the objective value curve in optimization steps and the frequency, quality factor, mass and coupling relative to the baseline value. The dominance in the decrease of frequency increase the coupling.

Whether the square-shaped membrane is an actual improvement remains to be validated experimentally. The loss could easily outweigh the benefit if the square-shaped membrane fabrication brings a greater reduction in the quality factor. The improvement of the objective function could be an illusion of the simulator. The curvature near the edge of the membrane is sensitive to meshing. A larger mesh distorts the motion, creating a misleading curvature value. During the operation in optimization, the simulator is inert to such problems due to a lack of observation. Although we tried to exclude the meshing and geometry issues from this optimization, further investigation is required to validate this optimization result.

We adopt a wheel membrane design with a longer tether to capture the optimization spirit. Due to the time constraints, we are not able to fully analyze the fabrication feasibility of the square membrane. The detailed parameters are set in appendix.C.1. The fundamental mode has a frequency of 26.616 kHz, while the second and third modes have frequencies of 67.099 kHz and 70.803 kHz, respectively. The calculated physical mass, effective mass, change of capacitance,

and quality factor for the fundamental mode are 620.5 ng, 64.75 ng, $-2.20 \cdot 10^{-7}$, and $8.04 \cdot 10^{7}$. We can directly calculate the zero point fluctuation of position given the effective mass and frequency using $x_{zpf} = \sqrt{\frac{\hbar}{2m_{eff}\omega_m}}$; the value is 2.21 fm.

4.1.3 Membrane metallization

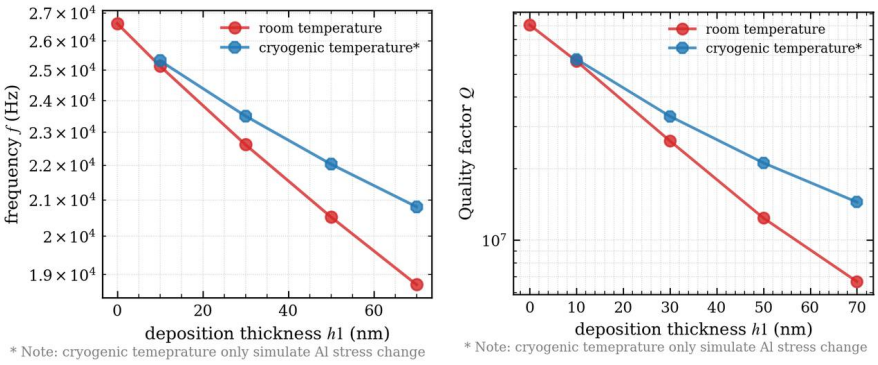

Figure 4.4: Left: frequency-deposition thickness plot for 100 nm wheel membrane with Al of -300 MPa(cryogenic temperature = 10mk) and 0 Pa (room temperature = 298k). The point with zero deposition thickness is shared by blue and red point Right: Quality factor-deposition thickness plot. The frequency and quality factor drops less with higher deposition stress. The simulation doesn't consider the temperature dependence of intrinsic quality factor.

Using the optimized membrane, we obtain the mechanical mode frequency and the quality factor dependence on the deposition thickness in Figure.4.4. An increase in the thickness of the deposition reduces the frequency and quality factor. After 10 nm of Al deposition, the frequency decreases from 26.6 to 25.1 kHz. The quality factor shrinks by a factor of 0.75 from $8.05 \cdot 10^{7}$ to $6 \cdot 10^{7}$. When the thickness increases, the change scales linearly. For room temperature simulation, the frequency decreases by 2.4 kHz, 2.1 kHz, and 1.8 kHz for thicknesses of 30 nm, 50 nm, and 70 nm. The frequency differences seem to be the same at 0.3 kHz, indicating a quadratic trend. The same effect can be seen for cryogenic temperature simulation, with a frequency difference of 0.2 kHz.

Differing from the result in [47], for soft-clamped membranes, the degradation of the quality factor after metallization depends less on curvature modulation. The quality factor degradation due to metallization is only 0.125 for 50 nm deposition, less than the 1 to 2 orders of magnitude degradation reported. This can be understood because the curvature distribution is equalized across the whole membrane, rather than concentrated at the connecting edge. The percentage of added loss follows the dissipation dilution, which is smaller for the fractal membrane.

The invariance of the quality factor suggests that intrinsic loss dominates the increase in the quality factor at cryogenic temperatures. Ref. [48] reported a quality factor increase of the square membrane by a factor of four from $3.2 \cdot 10^{7}$ to $1.27 \cdot 10^{8}$ when cooled to 14 mK. In fig.4.4, the cryogenic temperature quality factor represented by the blue curve is of the same order of magnitude as that in room temperature. The discrepancy arises because we assume the intrinsic loss to be constant. By assuming an intrinsic loss reduction factor of 4, we can obtain a Q-f plot for different modes. For a 30 nm deposition thickness with a stress equal to 0 MPa, the

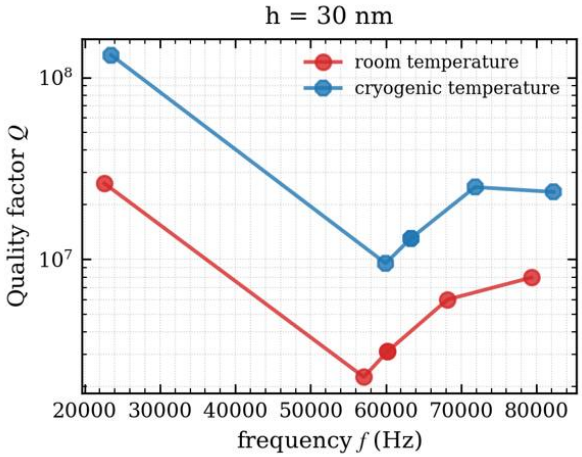

Figure 4.5: The quality factor and the frequency of the first 5 modes of the wheel membrane. Room and cryogenic temperature represents Al stress as -300 MPa and 0 MPa. The quality factor and frequency for the fundamental mode is $1.05 \cdot 10^8$ and 23.7 kHz at 10 mK after metallization.

fundamental mode frequency can reach a value of $1.05 \cdot 10^8$ at a frequency of 23.7 kHz. The effective mass is 78.9 ng.

4.1.4 Membrane buckling analysis

To check for the existence of a contractive stress region and the potential for buckling, we performed a principal stress analysis on the initial membrane and metallized it. Fig.4.6 shows it. The buckling region of the initial membrane is limited to the corner of the wheel branch. The lowest geometric third principal stress is $-8 \cdot 10^5$ Pa, low enough compared with the tensile stress of 10^9. This stress can be further reduced by varying the taper geometry and the radius of the filet.

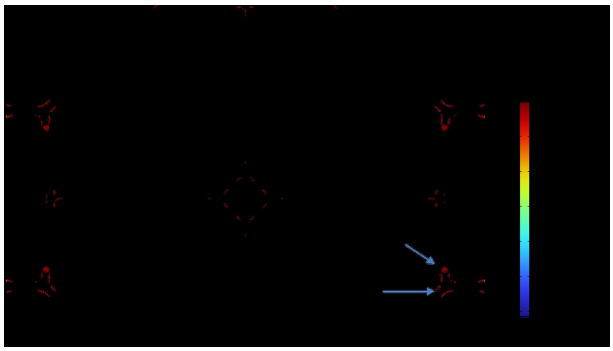

Figure 4.6: Buckling of the pure membrane. The third principal stress analysis shows that the corner of one has compressive stress up to $-8 \cdot 10^5$ Pa. Comparing with the tensile stress of 1 GPa, it can be ignored.

To check whether metallization introduces buckling, we repeat the third principal stress analysis on the metallized membrane. We first define the residual stress value in Al. Ref.[33] examines the residual stress of Al when deposited at room temperature. For 79 nm thick Al, the stress is -228 MPa. The thinner the al, the higher the residual stress. Therefore, we assume

that the residual stress for 30 nm Al is -300 MPa. We can also calculate changes in thermally induced stress. Following [34] calculations for the increase in stress for Al in silicon and the thermal similarity of Si and Si3N4, we calculate and take the stress increase to be +300 MPa. Therefore, the stress at 10 mK is 0 Pa. We also consider the case where annealing is performed on Al to relax the stress at room temperature. The residual stress of Al is zero. The cryogenic temperature stress for the Al layer is therefore +300 MPa.

Here we show the change in geometry of the center pad to demonstrate the deformation at thicknesses of 30 nm , 50 nm, and 70 nm, and stresses of -300 MPa, 0 MPa, and +300 Mpa in Figure.4.7. From left to right, the images in the first row illustrate the center pad region of 30 nm Al on top of a 100 nm Si_3N_4 membrane with Al stress of -300 MPa , 0 MPa, and +300 MPa.

The metallization with tensile stress bends the pad towards the qubit, potentially challenging the flip-chip bonding process. From top to bottom, the images in the third column demonstrate that for thicker deposition, both the third principal stress and curvature increase. The bending direction is on the Al side, which is also the direction facing the qubit when bonded. Such bending decreases the gap between the membrane and the qubit. This lowers the pull-in voltage because the closer edge of the membrane reduces the maximum pull-in distance, thus reducing the coupling. More importantly, any dust between the membrane and the qubit is more likely to touch the membrane. This requires the flip-chip bonding process to be dust-free.

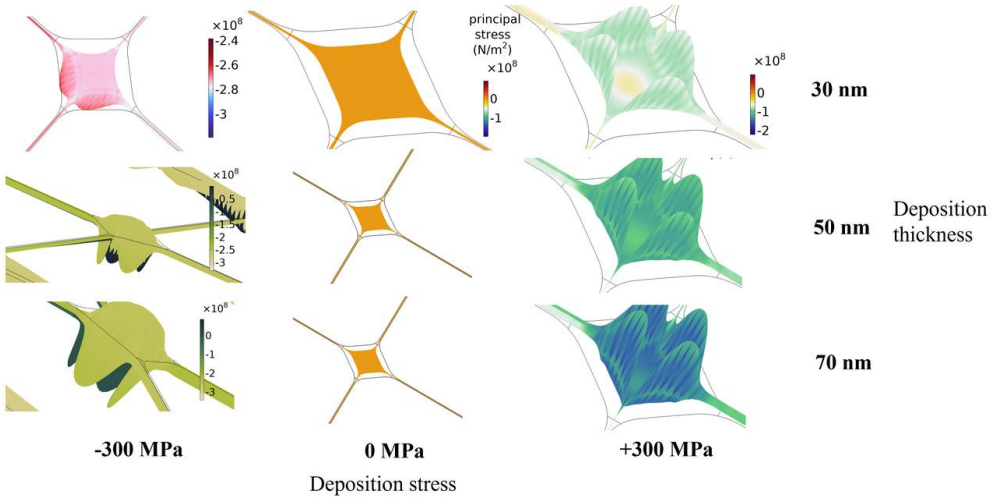

Figure 4.7: Buckling of the membrane pad is presents. The color is ploted according to the value of third principal stress. From left to right, the stress is -300 MPa, 0MPa and +300 MPa. From top to down, the thickness is 30 nm, 50 nm ,70 nm.The front surface is the Al layer. The front surface that we can see in the plot of the membrane is the Al layer. The compressive(negative) stress of Al bends the membrane in an inward(inside the screen) direction. Tensile(positive) stress folds the membrane in the outward(outside the screen) direction. The center picture presents the membrane without Al stress. The surface is flat. The third principal stress value, indicated by color and the color bar, is of the order of 10^8 Pa.

To avoid the bending induced gap distance decrease, we can set the membrane at operation to be flat or bent in the other direction. This means that if we want to have a working device at 10 mK, the deposition stress at room temperature should be around -300 MPa. If we want to make it a device in room temperature, we can either set the stress to the compressive side.

The metallization with compressive stress bends the membrane in the opposite direction, slightly decreasing the gap distance and modulating the coupling. From top to bottom in the first column, higher deposition thickness bends the edge membrane inward more. The center part of the pad moves outward, decreasing the gap distance. The corresponding bending height is 0.30 μm for 20 nm thickness and 1.37 μm for 70 nm thickness for Al at 300 MPa. The static operation shape of the membrane is therefore bowl-like. In our calculation for coupling, we assume the membrane to be flat at the static position. This shape difference may increase the capacitance and decrease the pull-in voltage. To avoid pull-in, the bending height must be less than one third of the gap. Thus, the minimum gap between the membrane and the qubit chip is 0.9 μm and 4.01 μ m, respectively. The overall pull-in bound for the membrane is not influenced.

Although the third principal stress analysis shows high compressive stress along the membrane for non-negative stress, it may not imply that the device is too buckling-sensitive to fabricate. This is because this method fails to capture buckling here. For an unmetallized membrane, the principal stress analysis reveals the regions with compressive stress in the background of the tensile stress. That region may wrinkle and become an absorption and reflection center for propagating waves. For Al deposited membrane, the compressive third principal stress dominates because of the bending. The compressive region is no longer indicating an absorption center but rather a geometry change. The mechanical wave could still propagate in the dominant tensile stress direction. Evidence of this hypothesis can be observed from the non-significant drop in the quality factor in the simulation of metallization and the experimental results of the lotus membrane. This hypothesis needs further experimental support from tests of the quality factor of the metallized hierarchical soft-clamped membrane.

The correlation between bending direction and stress value can be understood through the nature of tensile and compressive stress. The compressive stress dominated membrane has a tendency to enlarge the area. If no edge is fixed, curvature appears due to the tendency to expand. The resulting geometry is the one with the lowest energy. For a compressive membrane, the lowest one is the one that can expand the most. The inward bending direction expands the compressive layer more than the outward direction due to the existence of the substrate membrane. Therefore, the membrane will bend in the direction where the Al layer faces. Tensile stress dominates the behavior of the membrane in the opposite way.

4.1.5 Qubit frequency estimation

We simulate the qubit frequency by calculating the capacitance matrix of a 2D qubit. The qubit geometry follows a 2D circuit created by Igor Kladaric, shown in fig.4.8 . We remove the antenna in our simulation.

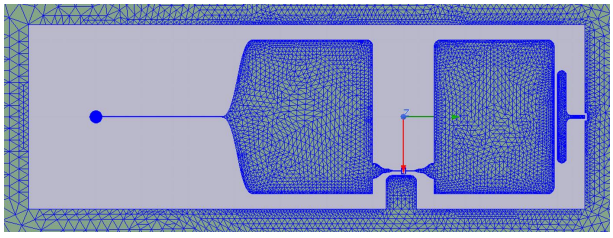

Figure 4.8: Mesh diagram of a 2D qubit design, taken from Igor Kladaric. It has two pads as the capacitaor connected by a group of josephson junction. The readout resonator locates as a bar at the left, coupling to the capacitor. The 2d qubit sits in a grounded box, dipicted as the wall around the qubit.

To calculate E_c, the qubit capacitance matrix is shown in the figure. 4.9 and Figure 4.10. The 3 by 3 plot shows the variation of capacitance with respect to gap distance, pad size length, x displacement, and y displacement between the membrane pads. The membrane only couples

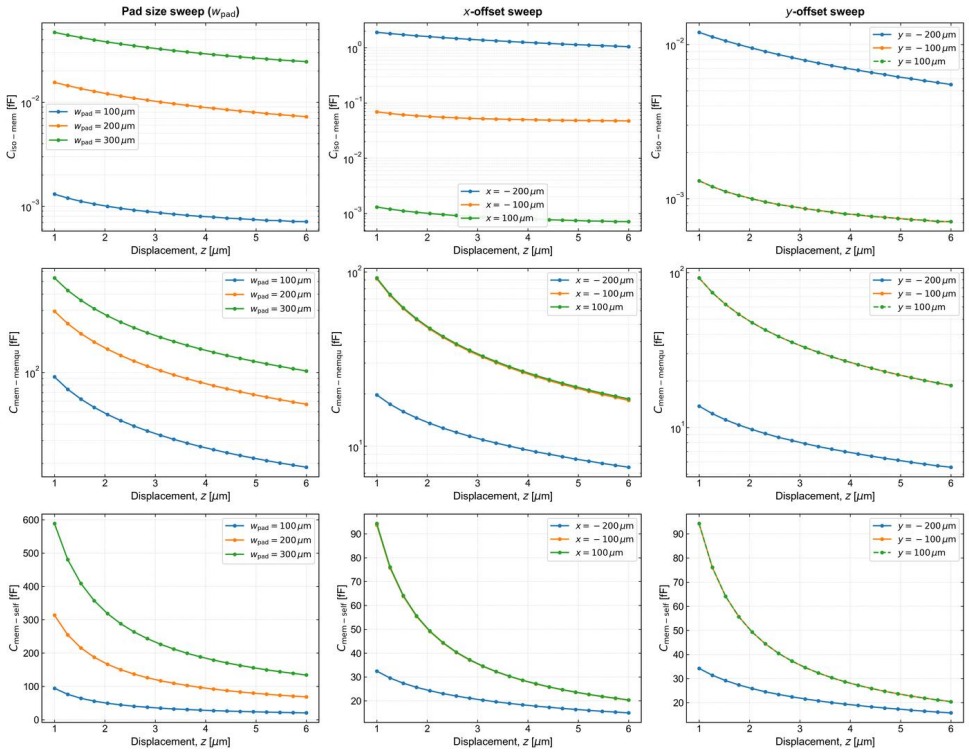

Figure 4.9: The membrane to close pad, membrane to far pad and membrane to membrane capacitance dependence on the relative position in x y direction of between membrane and close pad, distance between membrane and pad and size of the pad. The coupling between membrane and the close pad dominates.

to the closest pad of the qubit. We can see from the top right plot that the coupling between the far pad and the membrane is less than 0.01 for gap distances less than 2 μm. This value is 4 orders of magnitude smaller than the capacitance from the close pad to the membrane. The value we take is 567 fF since we use a pad size length of 400 μm and a distance of 2.5 μm.

	Ground	Pad_B	Pad_T	readout
Ground	425.388821	-211.430398	-190.315401	-23.643031
Pad_B	-211.430249	222.160673	-10.715164	-0.015091
Pad_T	-190.315408	-10.715072	229.468585	-28.437917
readout	-23.643034	-0.015094	-28.437963	52.096046

Figure 4.10: The capacitance matrix of the qubit-membrane device of the qubit devices shown before. Pad B is the pad facing membrane. Pad T is the pad that is far from the membrane. Readout and ground is the readout resonator and the cage.

The current design seems to allow the flip-chip bonding tolerance. The sensitivity of capacitance to movement is shown in Fig.4.11. We plot the capacitance to movement relation in a heat map for a 300 μm by 300 μm membrane with a tilted angle of 45 degrees on top of a qubit design. For a horizontal movement of 50 μm, no significant capacitance change is observed. For a vertical movement of 50 μm, less than 50 fF decay is recorded. The alignment precision can thus be controlled within 50 μm;

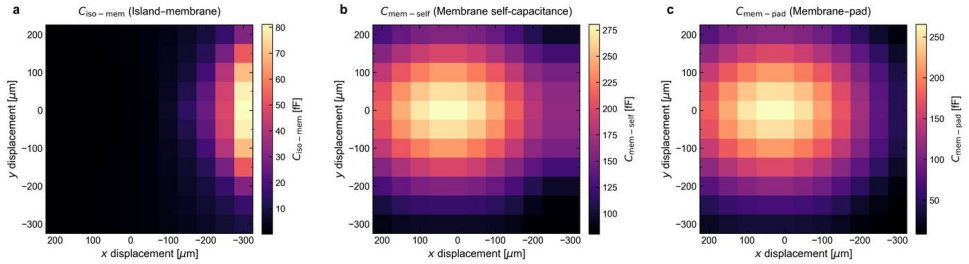

Figure 4.11: Heat map of capacitance. For left to right showing the capacitance profile of membrane-far pad, membrane-close pad and membrane-membrane. The color represents the value of capacitance. The x,y value represents the position offset of the membrane with respect to the center-to-center alignment point. The membrane can tolerate mismatch of 50 μm.

Taking the membrane that is biased by a constant voltage source and capacitively couples to PadB with a capacitance of 567 fF(d = 2.5μm), we can calculate the qubit E_C. Using the formula

$$E_C = \frac{e^2}{2}\mathbf{d}^T\mathbf{C}_{\text{dyn}}^{-1}\mathbf{d}$$

d is the differential charge mode:

$$\mathbf{d} = \begin{pmatrix} 1 \\ -1 \\ 0 \end{pmatrix}$$

The node for the vector is (PadB,PadT,readout). The reduced capacitance matrix gives:

$$\mathbf{C}_{\text{dyn}} = \begin{pmatrix} 789.160673 & -10.715118 & -0.015093 \\ -10.715118 & 229.468585 & -28.437940 \\ -0.015093 & -28.437940 & 52.096046 \end{pmatrix} \text{ fF}$$

Plugging in the value gives:

$$\frac{E_C}{h} \simeq 112.7 \text{ MHz}$$

E_L is usually a pre-defined parameter when a Josephson junction is fabricated. To allow the qubit frequency to be at 4 GHz, the value we take is $E_j/\hbar = 18.76$ GHz.

The β can be calculated as:

$$\beta = C_\Sigma \left[(\mathbf{C}_{\text{dyn}}^{-1})_{BB} - (\mathbf{C}_{\text{dyn}}^{-1})_{BT}\right] = 0.207 \tag{4.1}$$

The E_c of grounded qubit can be calculated by:

$$E_C = \frac{e^2}{2}C_B = 24.5 \text{ MHz} \tag{4.2}$$

4.1.6 Coupling estimation

Qubit frequency ω_q, qubit anharmonicity E_c, membrane frequency ω_m, membrane effective mass m_{eff}, and capacitance change $\frac{dC}{dz}$ are all calculated in the above session. The final coupling estimation can be derived. The pull-in voltage V_{pi} is 2.29 V (2.34 V).

With E_C = 112.7 MHz, ω_q = 4 GHz, V = 1.86 V (1.91 V)(80% pull-in limits), stress = -300 MPa(room temperature), 0 MPa(10 mK temperature), and metallization layer = 30 nm, we are able to plot the coupling modes for the metallized wheel membrane in room and cryogenic temperatures. The fundamental mode coupling strength is 0.772 MHz(0.775 MHz) which is less than the critical coupling strength of 4.75 MHz(4.86 MHz). The frequency and quality factor are 22.620 kHz(23.701 kHz) and $2.62 \cdot 10^7 (1.296 \cdot 10^8)$.

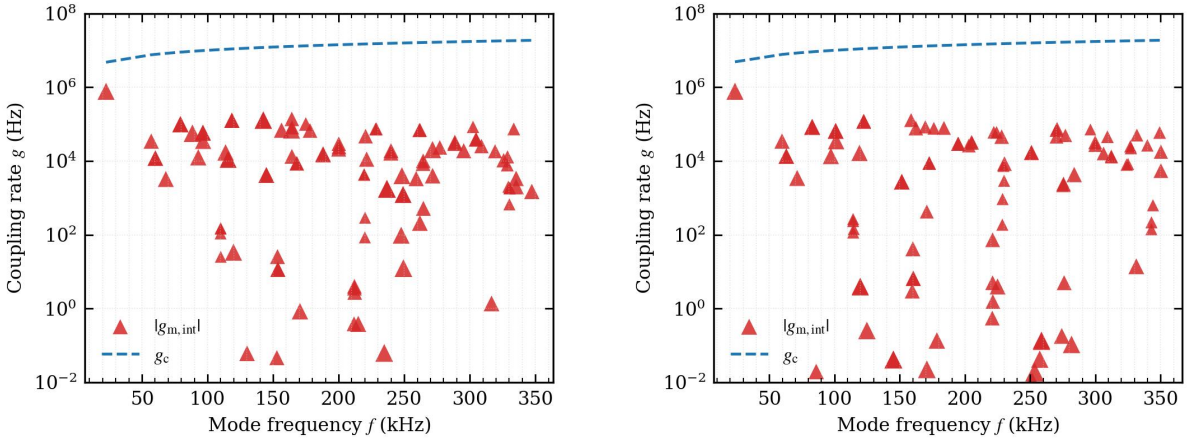

(a) Coupling strength at 298k.

(b) Coupling strength at 10mk

Figure 4.12: The coupling strength for first 100 mechanical modes at 298 k and 10 mk for the floating qubit. The mode frequency is the eigenfrequency for different modes. The blue dash line represents the critical coupling strength to overcome to enter DSC regime. The size of the red triangular dot represented the quality factor with the scale$((\log Q)^{1.4})$. None of the mode enters the DSC regime.

.

All of the modes are below the critical coupling value, proving that the device cannot reach the deep strong coupling. The highest mode, reaching 0.772 MHz, is only 0.168 of the critical value. The reason is that no free parameters can be tuned independently in coupling to increase the coupling within the pull-in voltage bound, as can be seen from Eq. (3.39).

Instead of coupling to the differential qubit, using a grounded qubit enables high coupling. Fig.4.13 shows an increase in the coupling strength for the fundamental mode from 0.772 to 1.728 MHz. The grounded qubit, having capacitance in parallel, only reduces the E_C, not the dC/dx. However, this is still limited by the pull-in voltage bound. The change of the qubit increases the bound to $\sqrt{(8/27) \cdot (567/789)} = 0.46$ of the critical coupling strength.

Notice that this is not a first-principles-like simulation to verify the theory. We extract the value from the simulation to complete the coupling equation. Validation of such results depends on the theory.

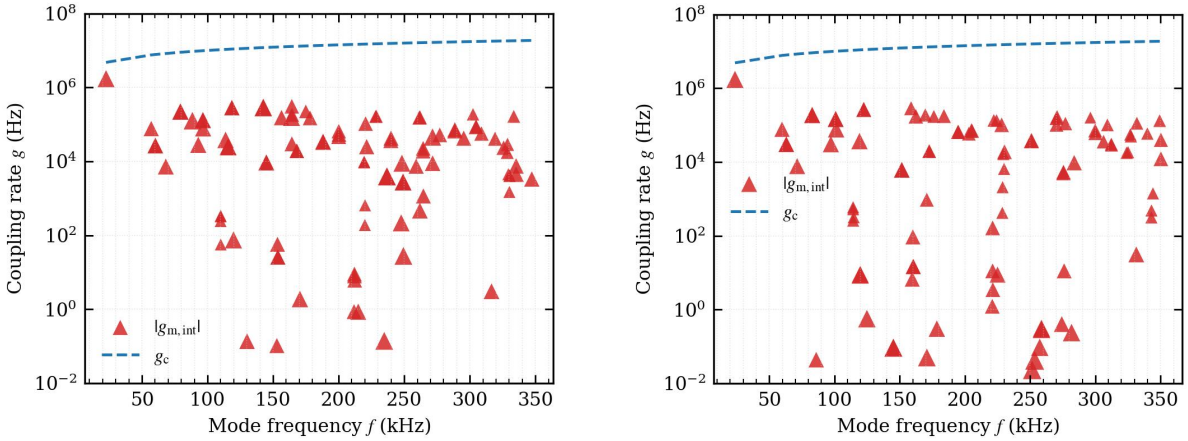

(a) Coupling strength at 298k.

(b) Coupling strength at 10mk

Figure 4.13: The coupling strength for first 100 mechanical modes at 298 k and 10 mk for grounded qubit. The highest mode reaches coupling of 1.728 MHz at 10 mK.

4.2 Membrane experimental characterization

In order to experimentally verify the feasibility of metallizing membranes and observe their changes in mechanical properties, we measured the interferometric properties of three lotus-shaped membranes before and after the metallization of a 20 nm thick aluminum layer.

Metallization allows electrical contact with an acceptable degradation of the membrane. We observed a factor of 4 decay in the quality factor and a shift of 100 kHz in one distinguishable frequency after metallization for two membranes. The other membrane had only a 20 percent decrease in the quality factor due to the difference in geometry. The best mode of the membrane still reaches a quality factor of more than 1 million at a frequency of 1.4 MHz. We record a very low resistance at room temperature. Together with the observation from the simulation that metallization barely changes the mode shape, we attribute the degradation of the quality factor to the decrease of the intrinsic quality factor Q_{int} and effective stress σ_{eff}. For different geometries, we expect the influence of metallization to be of the same order of magnitude as that of the lotus membrane.

4.2.1 Metallized Si_3N_4 lotus membrane

The spectrum of three lotus-shaped membranes before metallization and after metallization is plotted in fig.4.14. Two characteristic of the lotus membrane: bandgap and no Free spectral range are presented. The 1.56 MHz mode has a 200 kHz bandgap from the peripheral modes for all three membranes before metallization. The distribution of the other modes is non-uniform. Such a type of membrane possesses periodic holes on the surface. It creates a phononic crystal that has periodic conditions for specific frequencies.

The frequency modulation by metallization is expected, as presented in the top left corner of fig.4.14. The eigenfrequency is proportional to the effective stress $\sqrt{\sigma}$. Assume that the deposition of Al introduces a compressive stress of -300 MPa. We can calculate the effective stress of the membrane using the following formula $1 \cdot 1 - 0.3 \cdot 0.2GPa/1.2GPa = 0.8Gpa$. $1.56 \cdot \sqrt{0.8} = 1.395MHz$. The expected frequency of 1.395 MHz is very close to the detected frequency of the membrane. The difference could be attributed to multiple reasons, such as

non-uniform metallization on the membrane, surface defects, and geometry depending on the membrane thickness. More metallization samples could help reveal this mismatch.

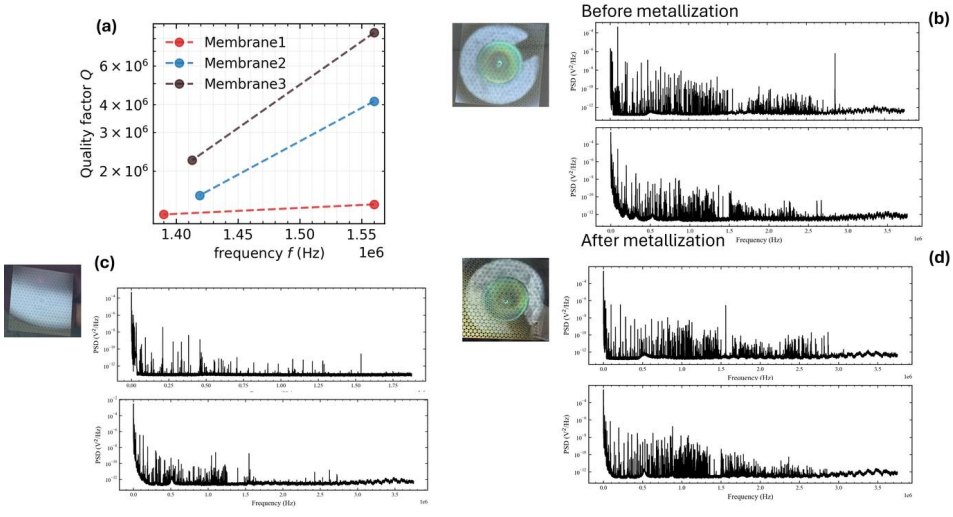

Figure 4.14: (a) the quality factor and frequency drop of the fundamental mode before and after metallization of 20 nm Al for three membranes. The initial frequency for three mode is 1.56 MHz. (b)-(d) the picture, spectrum before and after metallization for membrane 2, 1 and 3. The bandgap protected mode locates at 1.56 MHz. The metallization process uses an e-beam to evaporate 20 nm of Al on top of the silicon nitride membrane. The 1.56 MHz mode is reduced to 1.41 MHz for membranes 2 and 3, and 1.39 MHz for membrane 1.

The quality factor drops differently on two membranes. From the previous simulation on the wheel membrane and diagonal membrane, the quality factor drop is 33% to 50%. The decay of quality above 90% is not expected. For lotus membranes 2 and 3, the quality factor drop reaches 75%. For lotus membrane 1, the quality drop is from $1.41 \cdot 10^6$ to $1.27 \cdot 10^6$. Such a difference is due to the fact that the quality factor also depends on the geometry of the membrane. The hole to hole distance is smaller for membrane 1 than for membranes 2 and 3, modulating The quality factor. The detailed modulation requires a simulation for specific design.

The membrane after metallization seems to maintain a quality factor that allows for qubit operations. The decay time is $\frac{Q}{2\pi f} = 0.23s$, which is much longer than the qubit decoherence time of hundreds of μs. We need a quality factor three orders of magnitude smaller to be concerned about the decoherence problem.

4.3 Summary

In this chapter, we discuss the design and simulation of a membrane-transmon device. We show that the coupling aligns with the pull-in voltage limits, reaching 0.775 MHz for the floating qubit and 1.728 MHz for the grounded qubit. No indicator for buckling was observed from the simulation. The flip-chip bonding process and operation of the device favor metallization with non-positive residual stress.

Chapter 5

Proposal of capacitive readout of metallized membrane

Optical readout of the membrane using interferometry is the benchmark for the measurement of frequency (f_m) and quality factor (Q_m). In a cryogenic environment, the limited cooling power, space, and cooldown-induced thermal contraction require careful integration and alignment of optical components and vibration separation. In addition, using the membrane-qubit device for membrane readout requires validation of the device fabrication, characterization, and readout equipment setup. This motivates the use of electrical readout because it is compact, less complicated, and compatible with superconducting circuits. This proposed experiment aims to validate whether electrical readout can reliably recover the mechanical spectrum by comparing it with the optical benchmark. We will capacitively couple a metallized Si_3N_4 membrane to an LC resonator at room temperature and measure the mechanical spectrum. Following that, we will repeat the measurement using an interferometer to compare the linewidth and frequency of the peak of the target mode at 23.7 kHz. After room temperature validation, we will then characterize the spectrum at cryogenic temperatures. This experiment enables further experiments such as sideband cooling and OMIT.

5.1 Experimental principles

The mechanical resonator we use is a 100 nm thick wheel shape membrane with a fundamental mode of 23.7 kHz. For transduction, we metallize the surface with 20 nm thick Al using e-beam deposition. We then flip-chip bond the membrane on top of a 2D circuit with a 3 µm gap. The membrane will be carefully aligned with the metal pad on the 2D circuits, forming a parallel-plate capacitor with a capacitance of 400 fF.

The 2D circuit is an electrical LC resonator with a fundamental frequency of 2 GHz, simply defined by $\frac{1}{2\pi\sqrt{LC}}$. Physically, it is made of a coplanar waveguide, where the center region inductively and capacitively couples to the surrounding pad. To maximize the coupling strength with the membrane, part of the waveguide is thickened to match the size of the membrane pad. Although the full membrane metallization brings additional capacitance not limited to center pad, this capacitance offset is not time dependent due to mode localization. Ref.[49] provides a nice visualization for such a device, depicted in Figure.5.1.

Transduction occurs when the vibration of the membrane modulates the parallel plate capacitance, which changes the resonant frequency. By first order taylor expansion, we can deduce the capacitance transduction relation as $C_m(t) = \frac{\epsilon_0 A}{d-x(t)} = C_0 + \frac{dC}{dx}x(t)$,where $C_0 = \frac{\epsilon_0 A}{d}$. Let's now consider the fundamental mode with $\frac{dC}{dx} = \frac{C_0}{d}$. The modulated cavity angular frequency is then $\omega_c = \omega_0 - G_0 x(t)$, where $\omega_0 = \frac{1}{\sqrt{LC_s}}$ and $G_0 = \frac{\omega_0 C_0}{2C_s d}$.We simulate the target circuit us-

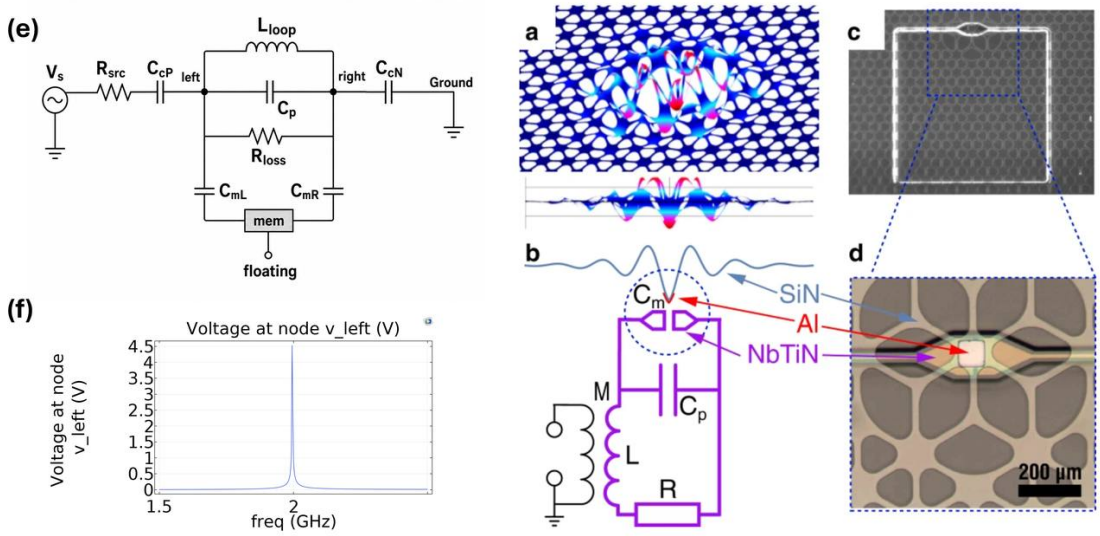

Figure 5.1: Edited from Ref.[49]. (a): the membrane vibration mode. (b): the circuit model used in the paper. (c): the overlook of the device. (d): enlarge image of the device, where membrane locate on top of the LC resonator. (e) the circuit we model for S11 read out. The membrane floats about to membrane. The coupling is energetic.

ing COMSOL with total capacitance of 0.48 pF and L = 13.02 nH, giving resonance frequency of 1.98 GHz. The sensitivity to membrane movement is 1.243 MHz/nm. Given the spectrum resolution of 50 kHz, the maximum displacement sensitivity is 0.04 nm.

This is the cavity field formula based on input-output theory and including a dissipation term: $\dot{a} = -(i\omega_c + \frac{\kappa}{2})a + \sqrt{\kappa_{ext}}s_i$. Given the probe at frequency ω_p, the solution yields $a = \frac{\sqrt{\kappa_{ext}}s_p}{\frac{\kappa}{2}+i\Delta(t)}e^{i\omega_p t}$, where $\Delta(t) = \omega_p - \omega_c(t)$. The output signal is $s_o = s_i - \sqrt{\kappa_{ext}}a = (1 - \frac{\kappa_{ext}}{\frac{\kappa}{2}+i\Delta(t)})s_p e^{i\omega_p t}$. $S_{11} = (1 - \frac{\kappa_{ext}}{\frac{\kappa}{2}+i\Delta(t)})$. Modulation of ω_c due to membrane vibration here would cause amplitude and phase changes according to the mechanical frequency of the membrane. Taking the derivative with respect to x gives : $\delta S_{11} = \frac{-i\kappa_{ext}G}{(\frac{\kappa}{2}+i\Delta_0)^2}x(t)$ where $\Delta_0 = \omega_p - \omega_0$. One can observe that the mechanical modes are encoded at frequency $\omega_p \pm \omega_m$ of the output signal, with different coupling constants G.

Choosing $w_0 = 2\pi \cdot 2$ GHz, $\frac{C_0}{C_s} = 0.2$, d = 1 μm , Q= 10^6, $\Delta_0 = 0$. This gives a total decay of $\kappa = 2\pi \cdot \frac{f_c}{Q} = 2\pi \cdot 12.57$ kHz. Taking the critical coupling condition at $\kappa_{ext} = \kappa_{int} = \frac{\kappa}{2} = 2\pi \cdot 6.283$ kHz. We can have $\delta S_{11} = \frac{-i\omega_0}{\kappa}\frac{C_0}{C_s}\frac{1}{d}x(t) = -iQ \cdot 0.2 \cdot \frac{1}{1} \cdot 10^6 x(t) \approx -2 \cdot 10^{11} i x(t)$. The thermal excitation displacement of the membrane can be expressed as $\sqrt{\frac{k_b T}{m\omega_m^2}}$. Using $\omega_m = 2\pi \cdot 23.51$ kHz, $m = 78.9$ ng , $T = 10$ mk, we have $x = 5.33$ fm. $\delta S_{11} \approx 1.06 \cdot 10^{-3} i$.

The f_m and Q for mechanical modes can be retrieved by analyzing the amplitude of S_{21} through power spectral density, read out by a spectrum analyzer or vector network analyzer(VNA). Using a similar setup, Teufel et al. demonstrated that continuous-wave microwave readout followed by homodyne demodulation can resolve mechanical displacements well into the sub-femtometer regime[50]. The thermal excitation of the membrane can be well captured.

The reason for not using linear transduction from motion to the charge involving a voltage biased membrane is that the cross-kerr interaction term for a GHz resonator and a kHz membrane is highly suppressed. Ref.[41] shows that the term scales with $8Ag^2\frac{\omega_m^2}{\omega_q^4}$, where A is the anharmonicity, g is the coupling, and ω_m,ω_q are the frequencies of the membrane and qubit. Even if critical coupling is reached, the energy change of the qubit imposed by a single phonon is strongly restrained by $\frac{\omega_m^3}{\omega_q^3} \approx 6 \cdot 10^{-16}$, which makes it impossible to observe. Although we could have multiple phonon processes, the required phonon number may be at the level of $2.7e9/23e3 \approx 1e5$ to match the required energy. The motion is therefore enlarged to the 30 fm level, comparable to the resolution demonstrated in the scheme shown here .

5.2 Device design

The loop gap resonator contains a 3.5x1.5 mm, 10 μm thick rectangular inductor and two parallel plates connected in parallel with an effective area of 0.4x0.4 mm^2. The wheel membrane with the same parameters in chap.4 was flip-chip bonded with 1 μm on top of the LC resonator. The resonator is made of niobium on top of silicon. Simulation shows that the effective capacitance of the resonator is 0.35 pF, reduced by the parasitic capacitance located on the overlap between the resonator and the membrane. The cavity resonance frequency is thus modified to 2.73 GHz.

To capacitively read out the resonator, two balanced feedlines of 3.5 mm long, 40 μm width each couple to the pad of the LC resonator with a connecting pad that has a length of 150 μm. The full device is 8 mm by 8 mm and is assumed to be placed in a metal box with only the feedline port exposed to the RF port of the fridge.

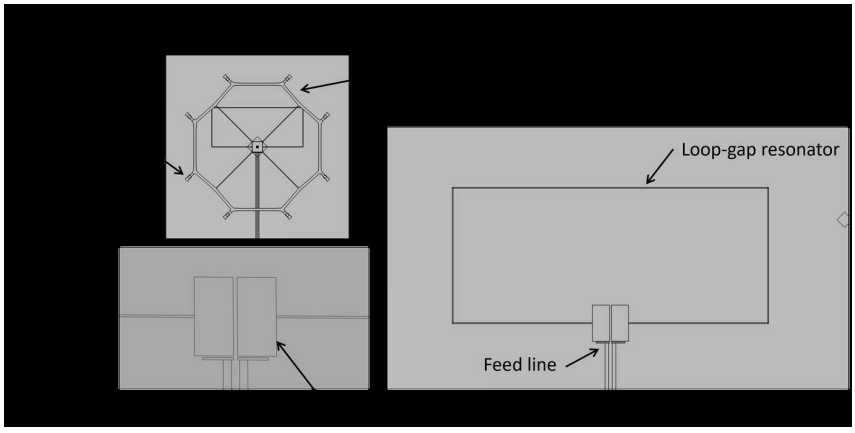

Figure 5.2: The geometry of the readout setup. (a) Outlook of a loop gap resonator coupling to kHz membrane. the membrane is assume to bonded to the resonator chip through 8 legs. A frame to hold the membrane could be included in the future. (b) The overlook for the Loop gap resonator. (c) the coupler between feedline and loop gap resonator.

5.3 Measurement plan

The bonded device will be mounted in the cryostat and first characterized at room temperature before cooling down. We first perform S_{21} sweeping to extract the LC cavity linewidth

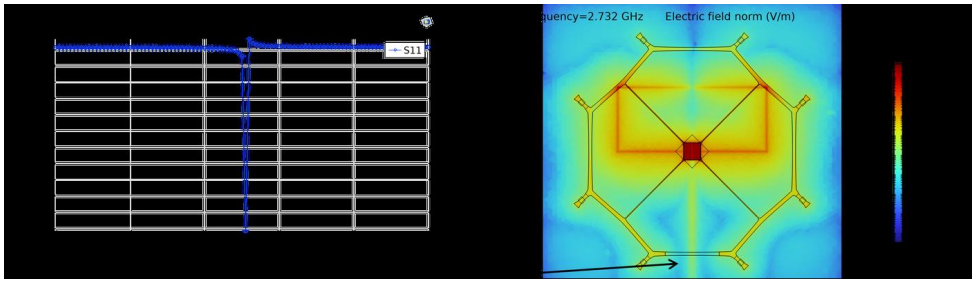

Figure 5.3: Left: S_{11} of the Loop-gap resonator when microwave enters from the port locate at the bottom of the right figure. The resonance around 2.7327 GHz with indistinguishable linewidth due to ignorance of loss in simulation. Right: The eigenmode consider the membrane, LC resonator and insider a perfect electric box. To deliver microwave to the resonator, part of the metallization is remove. The color represents the electric field 0.33μm above the qubit in log scale.

and the LC frequency. Similar to Ref.[51], this is done by sending in a frequency sweeping microwave tone and reading out using a vector network analyzer. Once we retrieve the resonant frequency, we choose a probe detuning where a small LC frequency shift produces the largest measurable amplitude or phase modulation. We limit the amplitude of the drive tone to avoid cavity nonlinearity.

By taking the power spectral density of the demodulated output signal, the target mechanical mode appears in the baseband spectrum near 23.7 kHz. If the thermal spectrum is too weak, a controlled electrostatic drive with target mechanical mode frequencies will be applied to measure the driven mechanical response. This is achieved by two tones with a 23.7 kHz separation.

To get a precise Q factor, we would first drive the membrane using beat notes created by two tones and then record the ring-down induced amplitude change of the corresponding sideband peak. By fitting the amplitude exponential decay time τ_{amp}, Q can be obtained with $Q_m = \pi f_m \tau_{amp}$.

Once the spectrum and Q factor are obtained at room temperature, we cool the system to cryogenic temperatures. We will record the PSD of the membrane and Q factor during the cooldown process for fitting the Boltzmann distribution to obtain the effective temperature of the membrane. The measurement procedures remain the same.

In the optical setup, we first perform a calibration of the laser power and the GRIN lens position to maximize sensitivity to membrane vibration. A PSD of the interferometry signal provides an estimation of the resonant frequency and linewidth. We then measure the Q factor by fitting an exponential curve to the amplitude given by the ring-down experiment.

5.4 Expected outcome

Fig.5.3 shows the simulation of the eigenmode of the loop-gap resonator coupling to a wheel membrane and the input reflection coefficient(S_{11}) without consideration of loss. Measurement of S_{11} should have a Lorentzian-like shape centered at the cavity design frequency $f_c = 2.7327$ GHz with additional asymmetry. The fitted Lorentzian linewidth $\frac{\kappa}{2\pi}$ indicates the energy decay rate of the cavity. At room temperature, LC circuit is lossy. We expect the linewidth to be in the hundreds of MHz range[51].

The targeted fundamental mode of the wheel membrane has a frequency of 23.7 kHz and

a Q_m of 105 million, corresponding to a linewidth of 9.8e-4 Hz. The power spectral density of the LC cavity sideband should show a peak at the same frequency as the optical measurement, while the linewidth could be broadened. We can characterize the additional loss by comparing the linewidth with optical results and the 3D cavity system [48].

5.5 Potential risk and mitigation

At room temperature, a lossy LC cavity results in a sideband nonresolvable region. The sideband signal is thus part of the cavity spectrum noisy background, posing challenges in reading it out. Additionally, the thermal excitation is rather weak. To increase the SNR, we can first inject a broadband 2 MHz white electrical noise, from which the mechanical modes can gain energy, allowing for the measurement of the driven response. Multiple methods, such as optimizing the driving power, frequency, and reconstruction algorithms, can be applied to increase the SNR simultaneously. If it continues to be challenging to read out, we would cool down the system to achieve superconductivity to decrease κ. To have the mechanical modes fully resolved in sideband, one needs to achieve $\kappa \ll \omega_m$. Although it is not required for our setup, it is important for experiments like OMIT and sideband cooling. If it is still not resolvable, future experiments could consider feedback cooling, such as ref [52]. With sideband cooling or feedback cooling, one can enter the quantum region that makes the device applicable for quantum operation[53].

Chapter 6

Conclusion and Outlook

This thesis investigated whether a low-frequency, high-Q metallized Si_3N_4 membrane can be capacitively coupled to a superconducting charge circuit strongly enough to produce the displaced ground-state structure sought in the deep-strong-coupling regime. The work combined a circuit-level derivation, finite-element modeling of the mechanical and electrostatic device, preliminary characterization of metallized membranes, and the design of an electrical readout experiment. The central conclusion is that increasing the linear membrane–transmon coupling alone is not sufficient to reach the target regime.

Starting from the circuit Lagrangian, an exact Hamiltonian was derived for a voltage-biased membrane and transmon whose coupling capacitance depends on displacement. This derivation shows that the linear charge–displacement interaction and a positive quadratic A^2 term arise from the same charging-energy expression. In the harmonic-transmon and adiabatic limits, the quadratic term cancels the mechanical softening caused by virtual qubit transitions. A separate restriction is imposed by electrostatic stability: for the single-sided parallel-plate capacitor considered here, pull-in occurs before the critical coupling strength can be reached. This conclusion is specific to the circuit topology and approximations used here; it does not exclude capacitive electromechanics more generally.

The Cooper-pair box offers a different possibility because its ground-state energy retains appreciable curvature with respect to gate charge. In the two-charge-state approximation, this curvature becomes negative for $E_J < 4E_C$, so the softening induced by the linear interaction is not fully canceled by the quadratic term. Combining this result with the pull-in constraint gives the idealized condition

$$\frac{E_J}{E_C} < \frac{32r}{27 + 8r}, \qquad r = \frac{C_m}{C_\Sigma}. \tag{6.1}$$

For $r = 0.968$, the corresponding bound is $E_J/E_C < 0.89$. This result identifies a concrete parameter window for further study, but it does not yet prove that an experimentally realizable CPB-membrane device will reach the desired regime. Such a claim requires a calculation using the full charge basis, the nonlinear capacitance and voltage-source potential, and the mechanical and electrical loss channels of the complete device.

A COMSOL workflow was developed to evaluate membrane eigenmodes, dissipation dilution, metallization-induced deformation, buckling risk, capacitance matrices, and electromechanical coupling. The final wheel-membrane design consists of a 100 nm Si_3N_4 membrane with a 30 nm Al layer and a simulated gap of 2.5 μm to the qubit chip. At 80% of the calculated pull-in voltage, the detailed model gives mechanical frequencies of 22.6 kHz at room temperature and 23.7 kHz at 10 mK, with coupling strengths of 0.772 MHz and 0.775 MHz, respectively. These values remain below the corresponding soft-mode thresholds of 4.75 MHz and 4.86 MHz. The simulations nevertheless show that megahertz-scale coupling to a kilohertz mechanical mode is compatible with a realistic membrane geometry. The absolute quality factors and the improvements suggested

by Bayesian geometry optimization should be interpreted more cautiously because they depend strongly on mesh resolution, intrinsic-loss assumptions, residual Al stress, and the boundary conditions used at cryogenic temperatures.

Interferometric measurements of three lotus-shaped membranes before and after the deposition of 20 nm Al provided an initial experimental test of metallization. The protected mode shifted from 1.56 MHz to 1.39–1.41 MHz, consistent with the combined effects of added mass and modified stress. The quality factor reduction varied substantially between samples: two membranes showed a reduction of approximately a factor of four, whereas the third retained a quality factor above 10^6 with a much smaller decrease. These measurements show that metallization can preserve a well-resolved and long-lived mechanical mode. However, the limited sample size and the variation in membrane geometry do not yet allow the additional loss to be assigned uniquely to intrinsic Al loss, reduced dissipation dilution, or fabrication-induced defects.

6.1 Outlook

For the next experimental step, a loop-gap LC resonator was designed to convert membrane motion into a microwave-frequency shift. The simulated resonance is approximately 2.73 GHz, with displacement transduction on the order of $1\,\mathrm{MHz\,nm^{-1}}$. Measuring the sideband spectrum and ring-down electrically, and comparing the extracted frequency and linewidth with interferometric measurements would directly test the readout concept.

6.1.1 Short-term objective: cryogenic membrane readout

The short-term objective is to fabricate and characterize the membrane at room temperature and under cryogenic conditions. Independent measurements of the residual Al stress and the temperature dependence of the membrane quality factor will be required to constrain the mechanical model. Agreement between electrical and optical measurements of the mechanical frequency and linewidth would validate the proposed readout method and provide a basis for subsequent sideband-cooling and optomechanically induced-transparency experiments.

6.1.2 Long-term objective: coupling to a charge-sensitive qubit

In the longer term, the circuit may be considered to be redesigned around a charge-sensitive Cooper-pair box with parameters satisfying both the DSC and pull-in constraints. This should be followed by a full numerical treatment of the coupled Hamiltonian, including the complete charge basis, the full model of the parallel plate capacitor, higher mechanical modes, and the relevant decoherence channels. Flux-sensitive circuits may provide another route, but their feasibility requires an independent derivation of the inductive coupling and its accompanying quadratic terms.

6.1.3 Contribution of thesis for future work

This thesis enhances the understanding of the feasibility and realization of the coupling between membrane-qubits towards the DSC regime through simulation, theory, and experiment. We have developed the groundwork for future simulation efforts. A basic understanding of hierarchical membranes was built thanks to the simulation. Furthermore, we have developed a reliable approach to simulate and optimize the membrane-transmon device with larger coupling

based on an existing membrane device. This process can be reapplied to membranes with different geometries, facilitating design choices. The theoretical work provides preliminary insight into the DSC regime requirements for device parameters and presents a basis for future investigation on CPB based devices. We have tested three membranes for aluminum deposition, reassuring the feasibility of the metallization process. In addition, the readout resonator was designed, suggesting an alternative method for the cryogenic readout of the membrane mechanical spectrum.

Bibliography

[1] Brian Vlastakis, Gerhard Kirchmair, Zaki Leghtas, Simon E. Nigg, Luigi Frunzio, S. M. Girvin, Mazyar Mirrahimi, M. H. Devoret, and R. J. Schoelkopf. "Deterministically Encoding Quantum Information Using 100-Photon Schrödinger Cat States". In: *Science* 342.6158 (2013), pp. 607–610. DOI: 10.1126/science.1243289. eprint: https://www.science.org/doi/pdf/10.1126/science.1243289. URL: https://www.science.org/doi/abs/10.1126/science.1243289.

[2] Sebastian Pedalino, Bruno E. Ramírez-Galindo, Richard Ferstl, Klaus Hornberger, Markus Arndt, and Stefan Gerlich. "Probing quantum mechanics with nanoparticle matter-wave interferometry". In: *Nature* 649.8098 (2026), pp. 866–870. DOI: 10.1038/s41586-025-09917-9.

[3] T. Kovachy, P. Asenbaum, C. Overstreet, C. A. Donnelly, S. M. Dickerson, A. Sugarbaker, J. M. Hogan, and M. A. Kasevich. "Quantum superposition at the half-metre scale". In: *Nature* 528 (2015), pp. 530–533. DOI: 10.1038/nature16155.

[4] Yaakov Y. Fein, Philipp Geyer, Patrick Zwick, Filip Kiałka, Sebastian Pedalino, Marcel Mayor, Stefan Gerlich, and Markus Arndt. "Quantum superposition of molecules beyond 25 kDa". In: *Nature Physics* 15 (2019), pp. 1242–1245. DOI: 10.1038/s41567-019-0663-9.

[5] Paul Adrien Maurice Dirac. *The Principles of Quantum Mechanics*. 27. Oxford: Oxford University Press, 1981.

[6] Markus Viktor Arndt, Olaf Nairz, Julian Vos-Andreae, Claudia Keller, Gerbrand Van der Zouw, and Anton Zeilinger. "Wave–particle duality of C60 molecules". In: *Nature* 401.6754 (1999), pp. 680–682. DOI: 10.1038/44348. URL: https://doi.org/10.1038/44348.

[7] Marius Bild, Matteo Fadel, Yu Yang, Uwe von Lüpke, Phillip Martin, Alessandro Bruno, and Yiwen Chu. "Schrödinger cat states of a 16-microgram mechanical oscillator". In: *Science* 380.6642 (2023), pp. 274–278. DOI: 10.1126/science.adf7553. eprint: https://www.science.org/doi/pdf/10.1126/science.adf7553. URL: https://www.science.org/doi/abs/10.1126/science.adf7553.

[8] Wei-Bo Gao, Chao-Yang Lu, Xing-Can Yao, Ping Xu, Otfried Gühne, Alexander Goebel, Yu-Ao Chen, Cheng-Zhi Peng, Zeng-Bing Chen, and Jian-Wei Pan. "Experimental demonstration of a hyper-entangled ten-qubit Schrödinger cat state". In: *Nature Physics* 6.5 (2010), pp. 331–335. DOI: 10.1038/nphys1603.

[9] Roger Penrose. "On Gravity's Role in Quantum State Reduction". In: *General Relativity and Gravitation* 28.5 (1996), pp. 581–600. DOI: 10.1007/BF02105068.

[10] Sandro Donadi, Kristian Piscicchia, Catalina Curceanu, Lajos Diósi, Matthias Laubenstein, and Angelo Bassi. "Underground test of gravity-related wave function collapse". In: *Nature Physics* 17.1 (2020), pp. 74–78. DOI: 10.1038/s41567-020-1008-4. URL: https://doi.org/10.1038/s41567-020-1008-4.

[11] Sougato Bose, Anupam Mazumdar, Gavin W. Morley, Hendrik Ulbricht, Marko Toroš, Mauro Paternostro, Andrew A. Geraci, Peter F. Barker, M. S. Kim, and Gerard Milburn. "Spin Entanglement Witness for Quantum Gravity". In: *Physical Review Letters* 119.24 (2017), p. 240401. DOI: 10.1103/PhysRevLett.119.240401.

[12] C. Marletto and V. Vedral. "Gravitationally Induced Entanglement between Two Massive Particles is Sufficient Evidence of Quantum Gravity". In: *Physical Review Letters* 119.24 (2017), p. 240402. DOI: 10.1103/PhysRevLett.119.240402.

[13] William Marshall, Christoph Simon, Roger Penrose, and Dik Bouwmeester. "Towards Quantum Superpositions of a Mirror". In: *Phys. Rev. Lett.* 91 (13 Sept. 2003), p. 130401. DOI: 10.1103/PhysRevLett.91.130401. URL: https://link.aps.org/doi/10.1103/PhysRevLett.91.130401.

[14] Brian Vlastakis, Gerhard Kirchmair, Zaki Leghtas, Simon E Nigg, Luigi Frunzio, Steven M Girvin, Mazyar Mirrahimi, Michel H Devoret, and Robert J Schoelkopf. "Deterministically encoding quantum information using 100-photon Schrödinger cat states". In: *Science* 342.6158 (2013), pp. 607–610. DOI: 10.1126/science.1243289.

[15] Stefan Nimmrichter and Klaus Hornberger. "Macroscopicity of Mechanical Quantum Superposition States". In: *Phys. Rev. Lett.* 110 (16 Apr. 2013), p. 160403. DOI: 10.1103/PhysRevLett.110.160403. URL: https://link.aps.org/doi/10.1103/PhysRevLett.110.160403.

[16] Yu Yang, Igor Kladarić, Maxwell Drimmer, Uwe von Lüpke, Daan Lenterman, Joost Bus, Stefano Marti, Matteo Fadel, and Yiwen Chu. "A mechanical qubit". In: *Science* 386.6723 (2024), pp. 783–788. DOI: 10.1126/science.adr2464. eprint: https://www.science.org/doi/pdf/10.1126/science.adr2464. URL: https://www.science.org/doi/abs/10.1126/science.adr2464.

[17] Hsiang-Yu Lo, Daniel Kienzler, Ludwig de Clercq, Matteo Marinelli, Vlad Negnevitsky, Ben C Keitch, and Jonathan P Home. "Spin–motion entanglement and state diagnosis with squeezed oscillator wavepackets". In: *Nature* 521.7552 (2015), pp. 336–339. DOI: 10.1038/nature14458.

[18] J. Casanova, G. Romero, I. Lizuain, J. J. Garćia-Ripoll, and E. Solano. "Deep Strong Coupling Regime of the Jaynes-Cummings Model". In: *Physical Review Letters* 105.26 (2010), p. 263603. DOI: 10.1103/PhysRevLett.105.263603. URL: https://doi.org/10.1103/PhysRevLett.105.263603.

[19] Nathan K. Langford, Ramiro Sagastizabal, Marios Kounalakis, Christian Dickel, Alessandro Bruno, Nils Luthi, David J. Thoen, Akira Endo, Leo P. Kouwenhoven, and Leonardo DiCarlo. "Experimentally simulating the dynamics of quantum light and matter at deep-strong coupling". In: *Nature Communications* 8.1 (2017), p. 1715. DOI: 10.1038/s41467-017-01061-x. URL: https://doi.org/10.1038/s41467-017-01061-x.

[20] Fumiki Yoshihara, Tomoko Fuse, Sahel Ashhab, Kosuke Kakuyanagi, Shingo Shiu, and Kouichi Semba. "Superconducting qubit–oscillator circuit beyond the ultrastrong-coupling regime". In: *Nature Physics* 13.1 (2017), pp. 44–47. DOI: 10.1038/nphys3906. URL: https://doi.org/10.1038/nphys3906.

[21] Mohammad J. Bereyhi, Alberto Beccari, Russell Groth, Sergey A. Fedorov, Amir Arabmohemdy, Nils J. Engelsen, and Tobias J. Kippenberg. "Hierarchical tensile structures with ultralow mechanical dissipation". In: *Nature Communications* 13.1 (2022), p. 3097. DOI: 10.1038/s41467-022-30586-z. URL: https://doi.org/10.1038/s41467-022-30586-z.

[22] Lorenzo Dania, Dmitry S. Bykov, Florian Goschin, Pau Mestres, and Tracy E. Northup. "Ultrahigh Quality Factor of a Levitated Nanomechanical Oscillator". In: *Physical Review Letters* 132.13 (2024), p. 133602. DOI: 10.1103/PhysRevLett.132.133602.

[23] Lukas Martinetz, Klaus Hornberger, James Millen, and Benjamin A. Stickler. "Quantum electromechanics with levitated charged particles". In: *npj Quantum Information* 6 (2020), p. 101. DOI: 10.1038/s41534-020-00333-7.

[24] Felix Tebbenjohanns, Martin Frimmer, Andrei Militaru, Vijay Jain, and Lukas Novotny. "Motional Ground-State Cooling of an Optically Levitated Nanoparticle with Dynamical Backaction". In: *Physical Review Letters* 124.1 (2020), p. 013603. DOI: 10.1103/PhysRevLett.124.013603.

[25] G Pagano, P Dubé, and A A Madej. "Cryogenic setup with a macroscopic Paul trap for single-ion optical clocks". In: *Quantum Science and Technology* 4.1 (2018), p. 014004. DOI: 10.1088/2058-9565/aae059.

[26] Philipp Treutlein, David Hunger, Stephan Camerer, Theodor W Hänsch, and Jakob Reichel. "Micromechanical oscillator ground-state cooling and state transfer with a superconducting qubit". In: *Physical Review Letters* 99.14 (2007), p. 140403. DOI: 10.1103/PhysRevLett.99.140403.

[27] Christoffer Reinhardt, Tina Müller, Alexandre Bourassa, and Jack C. Sankey. "Ultralow-noise photothermal cooling of a low-frequency nanomechanical resonator". In: *Nature Physics* 16.1 (2020), pp. 40–44. DOI: 10.1038/s41567-019-0683-5.

[28] Amir H. Ghadimi, Sergey A. Schilling, Yeghishe Tsaturyan, Albert Schliesser, and Tobias J. Kippenberg. "Elastic strain engineering for ultralow mechanical dissipation". In: *Science* 360.6390 (2018), pp. 764–768. DOI: 10.1126/science.aar6939.

[29] Sergey A. Fedorov, Alberto Beccari, Alireza Arabmoheghi, David J. Wilson, Nils J. Engelsen, and Tobias J. Kippenberg. "Fractal-like mechanical resonators with a high quality-factor-to-mass ratio". In: *Physical Review Letters* 124.25 (2020), p. 255502. DOI: 10.1103/PhysRevLett.124.255502.

[30] B.D. Hauer, C. Doolin, K.S.D. Beach, and J.P. Davis. "A general procedure for thermomechanical calibration of nano/micro-mechanical resonators". In: *Annals of Physics* 339 (2013), pp. 181–207. ISSN: 0003-4916. DOI: https://doi.org/10.1016/j.aop.2013.08.003. URL: https://www.sciencedirect.com/science/article/pii/S0003491613001723.

[31] S. A. Fedorov, N. J. Engelsen, A. H. Ghadimi, M. J. Bereyhi, R. Schilling, D. J. Wilson, and T. J. Kippenberg. "Generalized dissipation dilution in strained mechanical resonators". In: *Phys. Rev. B* 99 (5 Feb. 2019), p. 054107. DOI: 10.1103/PhysRevB.99.054107. URL: https://link.aps.org/doi/10.1103/PhysRevB.99.054107.

[32] Guruprasad Sosale, Dorothée Almecija, Kaushik Das, and Srikar Vengallatore. "Mechanical spectroscopy of nanocrystalline aluminum films: effects of frequency and grain size on internal friction". In: *Nanotechnology* 23.15 (Mar. 2012), p. 155701. DOI: 10.1088/0957-4484/23/15/155701. URL: https://doi.org/10.1088/0957-4484/23/15/155701.

[33] C. C. Lin, W. Fang, H. Y. Lin, et al. "Measurements of residual stresses in Al film/silicon nitride substrate microcantilever beam systems". In: *Journal of Materials Research* 26.10 (2011), pp. 1279–1284. DOI: 10.1557/jmr.2011.111. URL: https://doi.org/10.1557/jmr.2011.111.

[34] Amir Youssefi, Mahdi Chegnizadeh, Marco Scigliuzzo, and Tobias J. Kippenberg. "Compact superconducting vacuum-gap capacitors with low microwave loss and high mechanical coherence for scalable quantum circuits". In: *Phys. Rev. Appl.* 23 (6 June 2025), p. 064071. DOI: 10.1103/q5bc-y54w. URL: https://link.aps.org/doi/10.1103/q5bc-y54w.

[35] Philip Krantz, Morten Kjaergaard, Fei Yan, Terry P. Orlando, Simon Gustavsson, and William D. Oliver. "A quantum engineer's guide to superconducting qubits". In: *Applied Physics Reviews* 6.2 (2019), p. 021318. DOI: 10.1063/1.5089550. URL: https://doi.org/10.1063/1.5089550.

[36] R. Barends, J. Kelly, A. Megrant, D. Sank, E. Jeffrey, Y. Chen, Y. Yin, B. Chiaro, J. Mutus, C. Neill, P. O'Malley, P. Roushan, J. Wenner, T. C. White, A. N. Cleland, and John M. Martinis. "Coherent Josephson Qubit Suitable for Scalable Quantum Processors". In: *Physical Review Letters* 111.8 (2013), p. 080502. DOI: 10.1103/PhysRevLett.111.080502.

[37] Jens Koch, Terri M. Yu, Jay Gambetta, A. A. Houck, D. I. Schuster, J. Majer, Alexandre Blais, M. H. Devoret, S. M. Girvin, and R. J. Schoelkopf. "Charge-insensitive qubit design derived from the Cooper pair box". In: *Physical Review A* 76.4 (2007), p. 042319. DOI: 10.1103/PhysRevA.76.042319.

[38] Yasunobu Nakamura, Yuri A. Pashkin, and Jaw-Shen Tsai. "Coherent control of macroscopic quantum states in a single-Cooper-pair box". In: *Nature* 398.6730 (1999), pp. 786–788. DOI: 10.1038/19718.

[39] J. Rahamim, T. Behrle, M. J. Peterer, A. Patterson, P. A. Spring, T. Tsunoda, R. Manenti, G. Tancredi, and P. J. Leek. "Double-sided coaxial circuit QED". In: *Applied Physics Letters* 110.22 (2017), p. 222602. DOI: 10.1063/1.4984299.

[40] Hanhee Paik, D. I. Schuster, Lev S. Bishop, G. Kirchmair, G. Catelani, A. P. Sears, B. R. Johnson, M. J. Reagor, L. Frunzio, L. I. Glazman, S. M. Girvin, M. H. Devoret, and R. J. Schoelkopf. "Observation of High Coherence in Josephson Junction Qubits Measured in a Three-Dimensional Cavity". In: *Physical Review Letters* 107.24 (2011), p. 240501. DOI: 10.1103/PhysRevLett.107.240501.

[41] Mario F. Gely and Gary A. Steele. "Phonon-number resolution of voltage-biased mechanical oscillators with weakly anharmonic superconducting circuits". In: *Phys. Rev. A* 104 (5 Nov. 2021), p. 053509. DOI: 10.1103/PhysRevA.104.053509. URL: https://link.aps.org/doi/10.1103/PhysRevA.104.053509.

[42] Uri Vool and Michel Devoret. "Introduction to quantum electromagnetic circuits". In: *International Journal of Circuit Theory and Applications* 45.7 (2017), pp. 897–934. DOI: 10.1002/cta.2359.

[43] Peter M. Osterberg and Stephen D. Senturia. "M-TEST: A test chip for testing microelectromechanical systems". In: *Journal of Microelectromechanical Systems* 6.2 (1997), pp. 107–118. DOI: 10.1109/84.585788.

[44] Zlatko K. Minev, Zaki Leghtas, Shantanu O. Mundhada, Lysander Christakis, Ioan M. Pop, and Michel H. Devoret. "The energy-participation ratio of superconducting circuits". In: *npj Quantum Information* 7.1 (2021), p. 131. DOI: 10.1038/s41534-021-00461-8.

[45] Fumiki Yoshihara, Sahel Ashhab, Tomoko Fuse, Kosuke Kakuyanagi, Kouichi Semba, and Jaw-Shen Tsai. "Hamiltonian of a flux qubit-LC oscillator circuit in the deep–strong-coupling regime". In: *Scientific Reports* 12.1 (2022), p. 6764. DOI: 10.1038/s41598-022-10203-1. URL: https://doi.org/10.1038/s41598-022-10203-1.

[46] Z. Kim, B. Suri, V. Zaretskey, S. Novikov, K. D. Osborn, A. Mizel, F. C. Wellstood, and B. S. Palmer. "Decoupling a Cooper-Pair Box to Enhance the Lifetime to 0.2 ms". In: *Phys. Rev. Lett.* 106 (12 Mar. 2011), p. 120501. DOI: 10.1103/PhysRevLett.106.120501. URL: https://link.aps.org/doi/10.1103/PhysRevLett.106.120501.

[47] Pen-Li Yu, T. P. Purdy, and C. A. Regal. "Control of Material Damping in High-Q Membrane Microresonators". In: *Physical Review Letters* 108.8 (2012), p. 083603. DOI: 10.1103/PhysRevLett.108.083603. URL: https://doi.org/10.1103/PhysRevLett.108.083603.

[48] Mingyun Yuan, Martijn A. Cohen, and Gary A. Steele. "Silicon nitride membrane resonators at millikelvin temperatures with quality factors exceeding 10^8". In: *Applied Physics Letters* 107.26 (2015), p. 263501. DOI: 10.1063/1.4938747.

[49] Yannick Seis, Thibault Capelle, Eric Langman, Sampo Saarinen, Eric Planz, and Albert Schliesser. "Ground State Cooling of an Ultracoherent Electromechanical System". In: *Nature Communications* 13.1 (2022), p. 1507. DOI: 10.1038/s41467-022-29115-9.

[50] J. D. Teufel, C. A. Regal, and K. W. Lehnert. "Measurement of the Motion of a Nanomechanical Resonator with a Microwave Cavity". In: *New Journal of Physics* 10.9 (2008), p. 095002. DOI: 10.1088/1367-2630/10/9/095002.

[51] A. N. Pearson, K. E. Khosla, M. Mergenthaler, G. A. D. Briggs, E. A. Laird, and N. Ares. "Radio-frequency optomechanical characterization of a silicon nitride drum". In: *Scientific Reports* 10 (Feb. 2020), p. 1654. DOI: 10.1038/s41598-020-58554-x. URL: https://doi.org/10.1038/s41598-020-58554-x.

[52] Ewa Rej, Richa Cutting, Joe Depellette, Debopam Celesta Datta, Nils Tiencken, Joonas Govenius, Visa Vesterinen, Gheorghe Sorin Paraoanu, and Mika A. Sillanpää. "Near-ground-state cooling in electromechanics using measurement-based feedback and a Josephson traveling-wave parametric amplifier". In: *Physical Review Applied* 23.3 (2025), p. 034009. DOI: 10.1103/PhysRevApplied.23.034009.

[53] Yulong Liu, Qichun Liu, Huanying Sun, Mo Chen, Shuaipeng Mau Wang, and Tiefu Li. "Coherent memory for microwave photons based on long-lived mechanical excitations". In: *npj Quantum Information* 9.1 (2023), p. 80. DOI: 10.1038/s41534-023-00749-x.

Appendix A

Calculation of $\frac{dC}{dx}$

Let's consider the case where the pad to pad distance is constant, while a small displacement $q(t)$ is assigned to the structure. The change in capacitance is given by

$$\delta C = \frac{\epsilon(\delta A)}{d}$$

where ϵ is the dielectric constant, δA is the fracture of area, and d is the pad to pad distance. We can write the displacement as a function of time and space as

$$d = u_0(r,t) + q(t)\phi_z(r)$$

where $u_0(r,t)$ is the initial displacement, $q(t)$ is the small displacement of the structure and $\phi_z(r)$ is the mode shape. The initial displacement $u_0(r,t)$ is assigned to be d_0, the distance between the pads. we can write the change in capacitance with Taylor expansion

$$\delta C = \frac{\epsilon(\delta A)}{d} = \frac{\epsilon(\delta A)}{u_0(r,t) + q(t)\phi_z(r)} \approx \frac{\epsilon(\delta A)}{u_0(r,t)}(1 - \frac{q\phi_z}{u_0(r,t)} + \frac{q^2\phi_z^2}{u_0(r,t)^2})$$

$$u_0(r,t) = d_0$$

By integration we get

$$C = \int_A \frac{\epsilon}{d_0}(1 - \frac{q\phi_z}{d_0} + \frac{q^2\phi_z^2}{d_0^2})\, dA$$

To get the first order change in capacitance with respect to q we take the derivative with respect to q and evaluate it at $q = 0$:

$$C_1 = \frac{dC}{dq}|_{q=0} = \int_A \frac{\epsilon}{d_0^2}(-\phi_z)\, dA$$

we can evaluate the integrals value by COMSOL; specifically, the integrals of ϕ_z can be calculated by:

$$\int_A \phi_z\, dA = \int_A \frac{shell.w}{max(shell.disp)}\, dA$$

$$\int_A \phi_z\, dA = \int_A \frac{sign(shell.w)shell.w^2}{max(shell.disp)^2}\, dA$$

Normalization is done by defining the maximum displacement of the shell as 1 or defining the shape of maximum energy stored to be 1. The second normalization corresponds to the definition of m_{eff}.

$$m_eff = \rho h \int_A \frac{shell.disp^2}{max(shell.disp)^2}\, dA$$

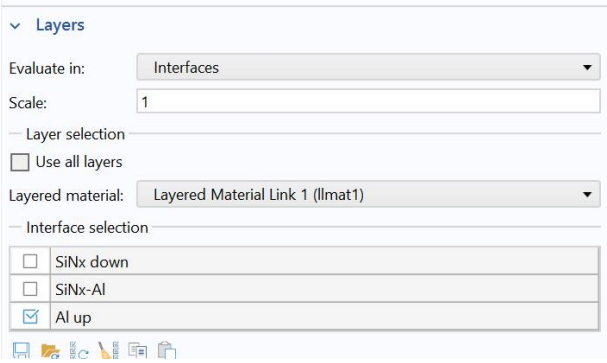

Figure A.1: layered shell setup

Notice that in layered shell interface, The surface integral includes all the surfaces defined in the material. For dual layer material, three surfaces exist. The integration of mass and area is overestimated due to repetitive measurements. This is also the origin of factor of three difference between simulation and analytics. In order to align the value analytically, we add a prefactor of $1/3$ to all of the dC/dx given by the simulation.

To avoid it, the layered material dataset needs to be assigned to take only the interface as shown in fig.A.1. However, effective parameters generated by COMSOL like lshell.rho, lsheel.Eequ will be invalid. The calculation of the quality factor requires the manual calculation of those effective values.

Appendix B

Methods in Membrane simulation

To prepare the device design and avoid risks in fabrication, we simulate the membrane with different geometries using the finite element method(FEM) with software named COMSOL. The validity of using FEM to simulate membranes has been well studied in research [21][47]. Although the simulation may differ from the actual experimental results, the mismatch is due to the discrepancies in the setup between simulation and reality. The boundary conditions, such as stress and mesh, are approximations of the real device stress and geometric conditions. Using suitable methods to set up the simulation and data analysis is necessary for valid conclusions regarding membrane design.

This chapter discusses the simulation setup in COMSOL for obtaining the results.

- Parametric geometry of the membrane
- The membrane mechanical mode shape, frequency, and quality factor
- Device capacitance matrix
- Metallization process of the membrane

Calculations of the coupling strength require effective mass m_{eff}, frequency$f$, quality factor of the membrane$Q$, qubit anharmonicity E_c, and qubit frequency ω_q. The shell and layer shell interface simulates the pure and metallized membrane, producing effective mass, frequency, and quality factor estimations at room temperature and cryogenic temperature. The electrostatic interface simulates the capacitance matrix using the positions of the device, producing a capacitance matrix that is the key ingredient for anharmonicity and qubit frequency estimation.

The buckling effect is examined through principal stress analysis on membrane mechanical modes before and after metallization. Thermal considerations address the device cooling issue. We can understand the risks associated with the membrane.

To speed up the simulation for novel geometry, we introduce the Bayesian optimizer. It can be viewed as a machine learning method that optimizes geometry under constraints.

Simulation of the LC resonator is done using the Rf interface. It generates the eigenmode for a device and the absorption spectrum around resonance.

Every session will start with a COMSOL setup, following a sanity check example.

B.1 Numerical simulation workflow

The numerical simulation workflow in COMSOL includes material setup, geometry setup, physics setup, mesh building, study settings, and result analysis. Material setup includes as-

signing the correct material properties, such as young's modulus and Poisson's ratio. It will be assigned to the geometry, such as a 2D or 3D shape, to fill in the physics equations defined by the physics setup. The setup of geometry discretizations is defined in the meshing. When everything is prepared, we configure the study and the algorithm to solve it. The solution that physics can provide will be visualized and plotted in the results analysis.

For membrane simulation, we will use the setup listed below:

materials	Si_3N_4, Al_2O_3 and Al
physics	shell or layered shell
mesh	mapped rectangles and tetrahedra
study	static(prestressed) and eigenfrequency

Table B.1: Summary of setup in COMSOL required for membrane mechanical simulation

The simulation of the mechanical mode essentially solves Eq.(2.2) of a complex geometry by splitting it into smaller blocks. Young's modulus(E), Poisson ratio(γ), and density(ρ) define the material for such a simulation. COMSOL lists several preset material options, including values for these parameters, but they do not necessarily agree with those listed in [21] and in actual fabrication. For comparison correctness, the following simulation takes E = 350 GPa,γ = 0.23,$\rho = 3100 kg/m^3$ from ref. [21].

The membrane geometry is 2D, requiring a shell interface to model correctly. The standard physics to simulate the mechanics of the block material is*the solid* interface. however, meshing the membrane, which is 100 nm thick but 1 mm long in 3D, requires a huge amount of resources for meshing blocks. Instead, the shell interface avoids the explosion of meshing by using 2D geometry with an additional rotating degree of freedom. The shell interface assumes the object to be layer-like so that it can twist and deflect. It requires a 3D study, but the input geometry needs to be 2D.

Modeling a multilayer membrane requires the layered shell interface. *layered shell* stitches several *shell* interfaces. Simulation in a layered shell solves mechanics in different layers together, resulting in precise intra-layer simulation. The stress mismatch induced buckling on layer materials and stress distribution through thickness can only be simulated using the layered shell interface

After setting up the physics interface, meshing defines the size for a finite element. The simulation result is closely related to the quality of the meshing. The mesh size must be small enough to enable precise capture of local geometry changes by mechanics. If a coarse mesh is applied, exponential decay at the edge of the membrane can be linearized. The mesh size cannot be too small to allow feasible computation. If a fine mesh is applied, the memory and time required to solve the problems will be unacceptable.

To find a balance, we use a suitable mesh shape and alter the mesh distribution. We can select Tetrahedral, triangular,free quad, and mapped to split the object. The tetrahedral pattern provides a good approximation to nearly all the motion of the membrane, from twisting to deflection, at the expense of the number of meshes. The mapped pattern reduces the required number of meshes while losing some ability to simulate torsional mode. The mapped pattern is rectangular, which confines the pointing direction more than the triangular one. This is suitable for deflection mode-dominant membranes but may not be a good mesh model for torsional membranes.

During metallization, the prestressed membrane is built in several steps in fabrication, so

it should be done in simulation. Metallization entails the simulation of the prestressed tension matrix. After that, the stress value was gradually increased to allow the solution to cover up. Otherwise, the eigenfrequency solver won't take the prestress into consideration. The solver behavior, including linearization setup, iteration limits, and error tolerance, can be set under each *study*. The default value is usually general enough for most membrane simulation cases.

Having the materials, physics, mesh, and studies set, we need to check if the simulation represents correct physics. This is usually done by comparing it with a ground truth, for example, a published paper result or a known formula. The simulation cannot be in complete agreement with the results of the experiment. Therefore, we aim for an agreement on the key properties. For membrane simulation, we want to make sure that the frequency and the mode shape of the same membrane undergoing the same configuration agree with the simulation done in the publication, or that the simulated capacitance agrees with the capacitance formula and the intuitive formula we had before.

B.2 The membrane modeling

We extract the membrane geometry using the OpenCV edge detection function to produce an edge only curve. With the curve, sketches are created to replicate the overall geometry. Following the membrane construction rule we learned in session 2, we convert the sketch dimensions to the closest values. Then we build the model in COMSOL parametrically.

B.2.1 Pure membrane simulation

Pure membrane simulation aims to simulate the mechanical motion of a single layer membrane with a physical structure. It takes membrane geometry as input and outputs the eigenfrequency, mode shape, and dilution factor. The setup of the COMSOL can be summarized with the table below.

material	Si_3N_4(E = 250GPa , $\rho = 3200$ kg/m^3, $\nu = 0.23$, prestressed force = 1GPa $\cdot$ 20 nm)
geometry	three-stages hierarchy membrane
physics	shell
mesh	mapped rectangle + tetrahedral for membrane joint
study	stationary + eigenfrequency (default)

Table B.2: Highlights for the setup in COMSOL for pure membrane simulation.

To prestress the membrane, we use *the initial stress* interface and *fixed edges*. *Initial stress* requires a two by two stress and strain tensor as input; we only need to specify the 11 and 22 positions of the stress and leave the other parts as zero. *Fixed edges* need to specify the edges that don't move. we assign the peripheral edges to be fixed.

The setup can be visualized in fig.B.1:

We verify the simulation by comparing it with the membrane result in [21]. Fig.B.2 shows the result. The left column illustrates the simulation result for the hierarchical structure membrane with its mode shape, dilution dissipation, and quality factor. The right column shows the simulation of the exact same geometry in COMSOL. Similar fundamental mode frequencies (101 kHz - 98 kHz), quality factor($8 \cdot 10^8$), bell-shaped deflection mode, and two steps of the deflection mode gradient prove the validity of our simulation setup to obtain the mechanical

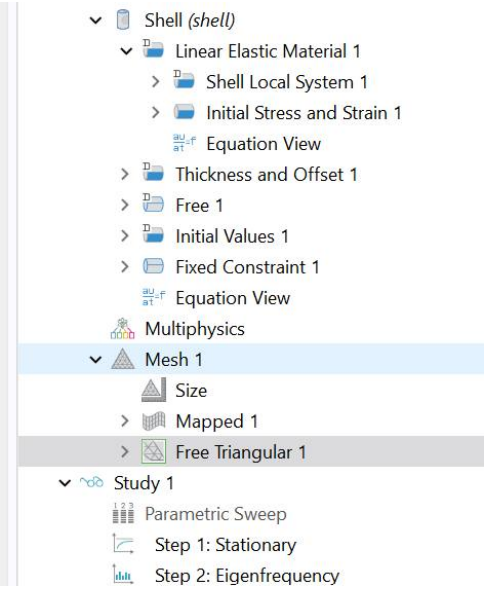

Figure B.1: The COMSOL setup for single membrane simulation

properties of the membrane.

It may be questioned whether these similar values are a result of fine-tuning the membrane geometry instead of actually capturing the mechanics. Properties such as eigenfrequency in a faulty setup can be tuned to be good by changing the length of the tethers.

To rule this out, We reduce the center pad size and soft-clamped tether lengths to simulate a soft-clamped 2D string model approaching the hard-clamped region. The hard-clamped 2D string mode has a frequency represented by equ.2.6. To convert the soft-clamped model to the hard-clamped one, we take the sum of the lengths of the tether from one fixed edge to another fixed edge of the hierarchical membrane as the length for the hard-clamped membrane. Given $\sigma = 1\text{GPa}$, $\rho = 3200\ \text{kg/m}^3$, L = 2.22 mm, the fundamental mode frequency is 125.9 kHz. As shown in fig.**??**, the soft-clamping condition is greatly suppressed. The simulation result gives 125.2 kHz, which is in agreement with the analytical result

Notice that the conversion of effective length to hard-clamped model is only applicable for short tethers, where the membrane is less soft-clamped. For large tethers, this conversion generates faulty results. This is because the mode shape of a soft-clamped membrane differs from a sinusoidal one. The new mode shape is no longer a solution for the 2D string model.

We can state that our configuration for this membrane seems valid. But this does not guaranty success with other complex geometries without checking. For example, if we apply the same meshing condition to a thinner membrane, fluctuations within a small range appear on the displacement plot of the membrane. This is because the size of the mesh is too large to capture the local structure where the motion changes greatly. The solver has to assign an extreme value to the large local mesh. To solve this, we need to redistribute the mesh size; otherwise, any displacement dependent result is no longer valid.

The mesh optimization is applied to all of our simulation results without special notice.

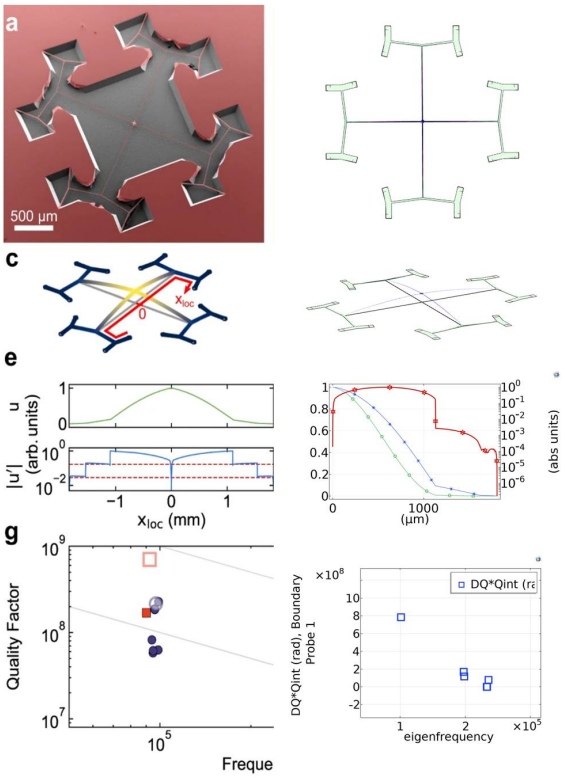

Figure B.2: Comparison between membrane in [21] and that in simulation.(a) left: the trampoline membrane right: the reconstructed membrane in COMSOL (c) left: the fundamental mode shape with the x value in (e) indicated by red line. right: the mode shape from simulation. (e) The deflection value and the gradient of it. (g) left: the red square is the simulated fundamental mode. the solid square is the experimental result. The circle shape represents other type of membrane. right: The blue square with the highest Q is the simulated fundamental mode in COMSOL. The other mode are the higer order mode. The Q factor and frequency for COMSOL simualtion and publication matches.

B.2.2 metallized membrane simulation

metallized membrane simulation targets the motions of multi-layer membranes made with different materials. It takes *layered material* and membrane geometry as input and outputs the mechanical motion of the membrane. The setup in COMSOL can be summarized in the table below:

The setting of the *layered shell* interface is key to properly simulating the metallized membrane. This includes setting up the *layered material*, applying initial stress and external stress separately under the *layered shell*, and adding one more static study step after the initial stress step.

The layered shell setup requires a globally assigned *layered material* with silicon nitride and a predefined aluminum layer. Connecting the layered material to the geometry is done through a layered material link under the *materials* in *the component*.

Under the *layered shell* interface, initial stress will be assigned to silicon nitride only. If all of the layers of the membrane are assigned different stresses at the beginning, a well constrained

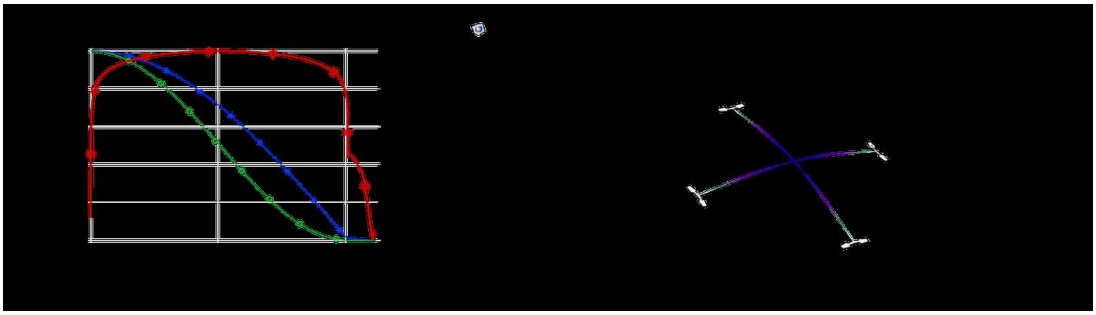

Figure B.3: The deflection along the tether and the mode shape for the soft-clamped membrane on the hard-clamped limits. The red curve shows the gradient of the deflection. The green line is the kinetic energe, the blue line is the normalized deflection.

material1	Si_3N_4(E = 250GPa +i0.1GPa, $\rho = 3200$ kg/m^3, $\nu = 0.23$, prestressed force = 0.9GPa $\cdot$ 50 nm)
material2	Al(E = 69GPa + i0.3GPa , $\rho = 2700$ kg/m^3, $\nu = 0.23$, prestressed force = -50MPa $\cdot$ 50 nm)
geometry	two-stages wheel membrane and square membrane
physics	layered shell
mesh	triangular
study	static(prestressed Si_3N_4) + static(gradual prestressed and equalize Al) + eigenfrequency

Table B.3: Setup for metallized membrane simulation

membrane, like a square membrane, is needed. Finding the static solution for the soft-clamping membrane is hard because not all of the edges are well confined. Buckling will occur because of the stress mismatch that causes the simulator not to converge.

To overcome the instability of the simulator, one more static step representing the deposition of aluminum is applied. We assign *external stress* with a value $step * \sigma$ to aluminum. We set the default value of the step to zero and activate the aluminum layer when the step is not zero. As a result, the first static study ignores the aluminum layer. In the second static study , we gradually raise the step value to 1 in an attempt to approach the accumulation of stress during deposition. We ramp up the stress in the study extension. It will automatically utilize the last solution to solve the next solution.

Sometimes, the buckling effect disturbs the solver stability severely. The remedy is to reduce the step to and to change the nonlinear methods. For the simulation of Al with residual stress -300 MPa, ordinary methods fail. We do the first thing: ramping up step by 0.01 from 0 to 1. Large steps could puzzle the simulator at some random step value. The second thing is to use Constant (Newton) nonlinear methods under full couple node in configurations of stationary solver. This decreases the sensitivity to weird buckling structure. With these two methods, the simulation successes.

The setup is summarized in Fig.B.4.

To validate our simulation, we simulate the same membrane made in [47] and compare it with their result. Specifically, [47] proposed an experimentally verified formula for the membrane frequency and quality factor:

$$Q_{mn} \sim \frac{1}{\lambda}\frac{E_1}{E_2}\left(\underbrace{1}_{\text{edge}} + \underbrace{\lambda\frac{(m^2+n^2)\pi^2}{4}}_{\text{antinode}}\right)^{-1}. \tag{B.1}$$

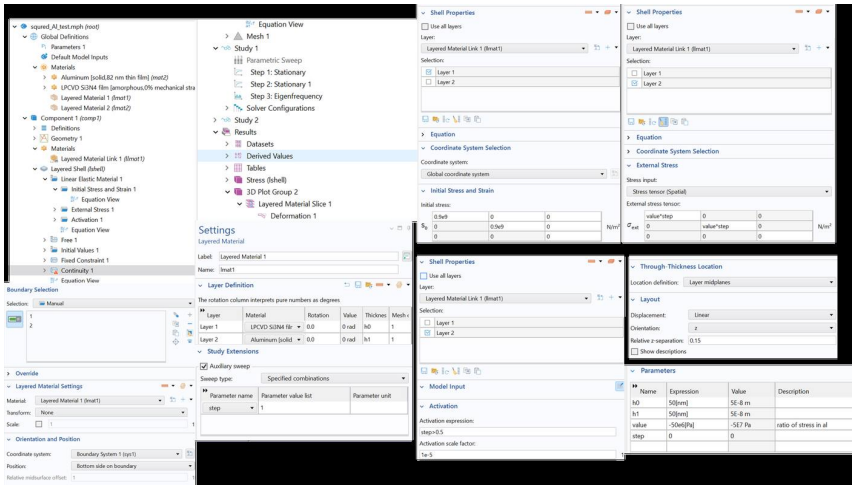

Figure B.4: Metallized membrane setup in COMSOL

$$f_{mn} \sim \sqrt{\sigma(m^2+n^2)/4\rho l^2} \tag{B.2}$$

where $\lambda = \sqrt{\frac{E_1}{(1-\nu)^2}(h_1+h_2)^2/3\sigma l^2}$. If our simulation could repeat the same physics, we would have an f-f and Q-f plot, where

1. The simulation frequency has a square root relationship with m^2+n^2, with a prefactor of$\sqrt{\sigma/4\rho l^2}$.
2. The quality factor of the membrane scales with frequency
3. If we have edged aluminum, we should see an increase in the quality factor, following equation B.1.

You may notice that the effective stress of our membrane is not defined initially. So fitting the deposition parameters is necessary to define it.

The left part of figure.B.5 shows the result that validates the frequency simulation. The frequency predicted by $\sqrt{\sigma N/4\rho l^2}$ compared to the actual simulated frequency is shown in the left panel, lower right part. A good fitting between the theoretical value and the simulated value is shown. We fit the effective stress to be 0.6 GPa, where the applied Al has an internal stress of -200 MPa.

The Q-f plot on the left shows that we have points 2 and 3 verified in trend, but they differ quantitatively. The blue curve representing the partially metallized membrane obtains a high quality factor, which is consistent with the publication. However, the fully metallized membrane, represented by the red curve, has a significant frequency dependence, differing from Eq. B.1. In addition, the absolute value of the quality factor does not match.

We attribute the mismatch of the quality factor between the publication and the simulation to the meshing setup, where the mesh is too coarse to capture the edge curvature. In equ.B.1, the edge contribution dominates the contributions from the other nodes. The effective length for which the edge curvature contribution is given by $\frac{\lambda l}{4}$ 0.2μm[47]. Only if we capture the movement of the edge at this value can we record the drastically changed curvature. The required meshing thus scales 4 orders of magnitude from tens of nanometers to hundreds of micrometers. Thus, it is computationally hard to model the edge contribution to loss accurately. The mesh size we

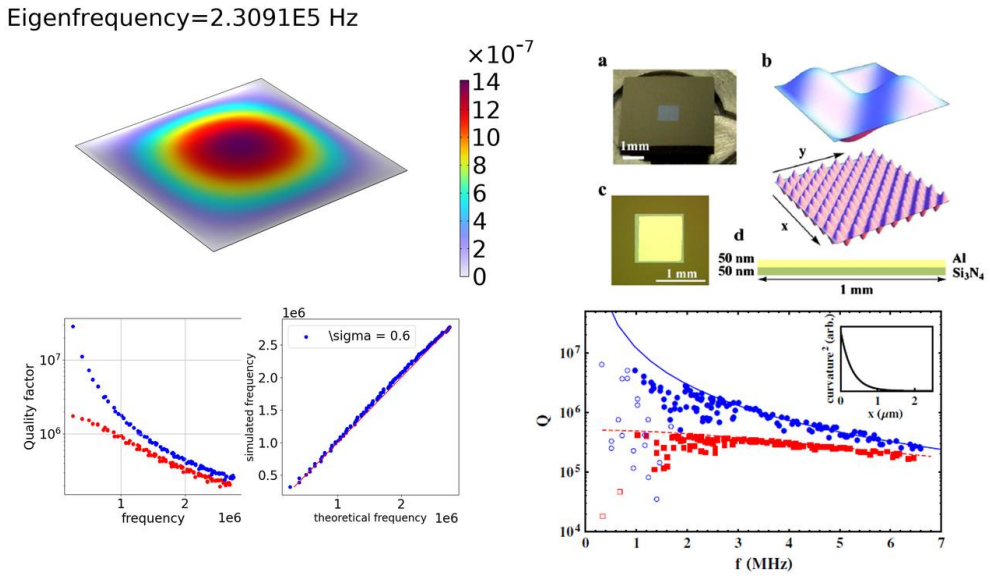

Figure B.5: Left: the COMSOL simulation on the exact same membrane of [47]. The red and blue line in Q-f plot represents the fully metallized membrane and partially metallized membrane. The fit line in the stress-frequency plot is the theoretical value predicted by $\sqrt{\sigma N/4\rho l^2}$. We retrieved the effective stress as 0.6 Gpa.

are currently using does not smooth the curvature at the edge and increases the curvature of the in-plane wave. So, we observe a higher quality factor at low frequencies and a larger gradient of descent for the quality factor.

To prove that considering the edge contribution will return the same publication result , we simulate a well meshed membrane indicated by a smooth displacement near the clamping point in order to capture the effective length $\frac{\lambda l}{4}$. The left part of the figure B.6 shows the improvement in the resolution of the membrane displacement around the hard-clamped edge by refining the mesh. The clamping point is at 0.15 mm. We set the mesh to distribute exponentially denser as it gets closer to the edge. From top to bottom, we increase the number of meshes. Only the finer mesh captures the curvature. The right part of the figure B.6 shows the same Q-f plot as before, using the finer mesh. The gradient of Q with respect to f now aligns with what was presented.

Notice that the effective length only limits the clamping capacity of the membranes. For the soft-clamping membrane that we are interested in, the dissipation dilution drastically reduces the change in curvature.

B.2.3 Electrostatic simulation

Electrostatic simulation is designed to estimate the capacitance between different pads. It takes the geometry of the membrane and qubit pads as input and outputs the capacitance matrix. The capacitance matrix can be used to estimate the qubit charging energy and the membrane coupling capacitance to qubit pads. The setup in COMSOL can be summarized in the table below:

Simulating capacitance requires a 3D volume that covers two pads to ensure that most of

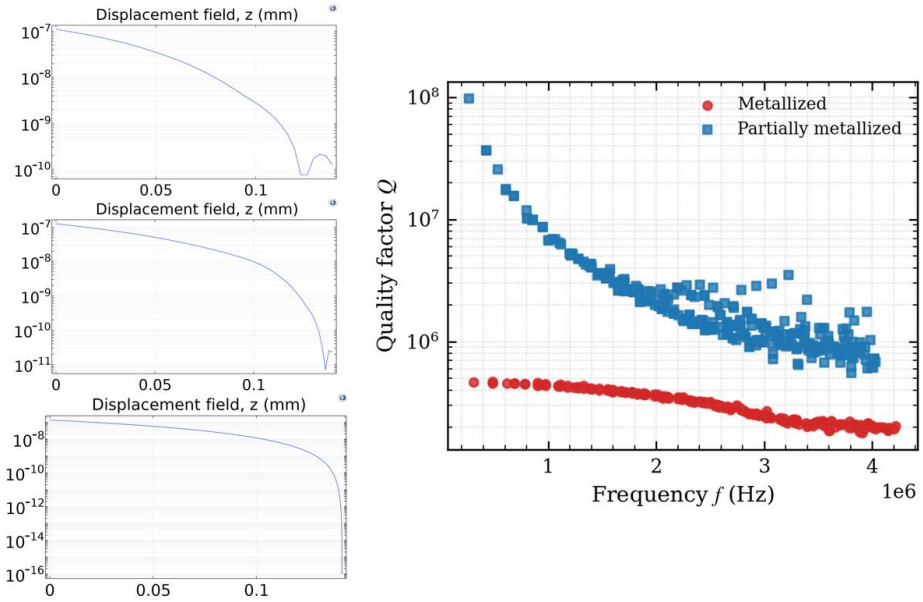

Figure B.6: left: displacement of square membrane at the edge with corase , norm, fine mesh. Right: Q-f plot with the fine mesh. For the fine mesh, the Q-f plot aligns with [47]

material1	$Al_2O_3(\epsilon = 10.3,\ \rho = 3200\ \mathrm{kg}/m^3,\ \nu = 0.23$, prestressed force $= 0.9\mathrm{GPa} \cdot 50\ \mathrm{nm})$
material2	AlN
material3	Vacuum
geometry	2D transmon qubit
physics	electrostatic
mesh	tetrahedral
study	stationary

Table B.4: Setup for electrostatic simulation

the electric field passing through the two pads is simulated. We distribute the mesh closer to the qubit pad more densely. *Terminals* and *ground* are applied to the pads to inform COMSOL which part to calculate the capacitance matrix. The setup can be viewed as follows:

We verify our COMSOL setup by comparing the parallel plate capacitance simulation with the analytical one $\frac{\epsilon_0 A}{d}$ and the simulated qubit capacitance matrix with the one simulated earlier. The right part of the figure B.8 shows a simulated analytical capacitance of a parallel plate capacitor that has a length of 400μm. The simulation agrees with the analytical result quite well. The left part shows a simulation of capacitance for a 2D circuit setup. The black figure shows a result obtained in ANSYS, while the brown figure shows the simulation done in COMSOL. Although the exact values do not match, considering the geometry is modeled by estimation of the original qubit, two values are close enough to state that the simulation can correctly model the capacitance matrix.

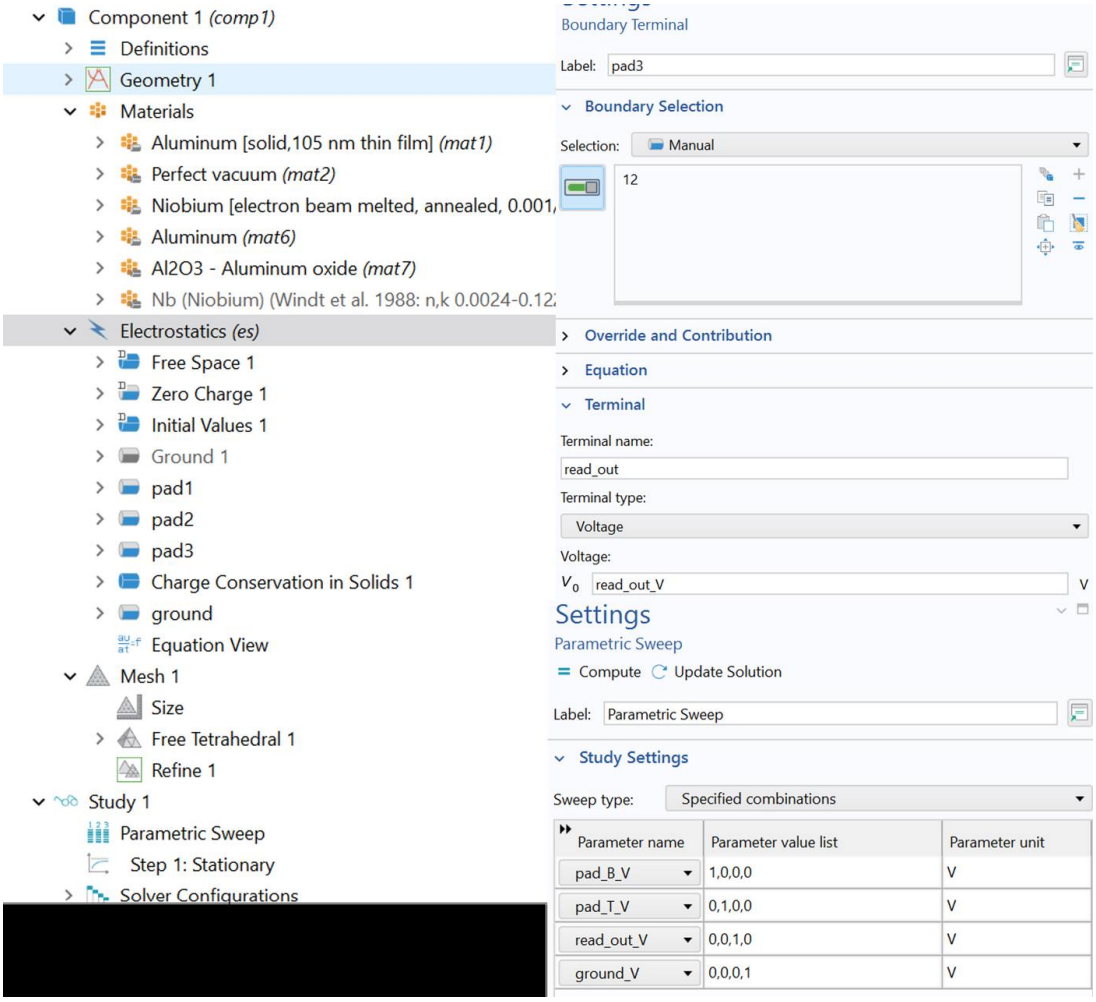

Figure B.7: Detailed COMSOL interface for electrostatic simulation

B.2.4 Coupling simulation

?? The coupling simulation serves to estimate the coupling constant g. Following Eq.(B.3), we need the effective mass m_{eff} and ω_m to estimate the zero point fluctuation of the membrane, the qubit frequency ω_q and anharmonicity E_c to obtain the charge number, and the distance d and the capacitance gradient $\frac{dC}{dx}$ to estimate the coupling prefactor. With those values ready, the coupling is the product of those.

$$\boxed{g = \frac{V_g}{e}\frac{\partial C_g}{\partial x}\sqrt{\frac{E_C\omega_q}{2m_{\text{eff}}\omega_m}}.} \tag{B.3}$$

Those values can be derived from the simulation mentioned before. The only non-trivial part to derive is $\frac{dC}{dx}$. Because the membrane has an approximately sinusoidal shape, The change in capacitance due to motion cannot be simply viewed as the movement of parallel plates. The contribution needs to be integrated. The detailed derivation of the value can be viewed in the appendix; the value we have is

$$C_1 = \frac{dC}{dq}|_{q=0} = \int_A \frac{\epsilon}{d_0^2}(-\phi_z)\, dA$$

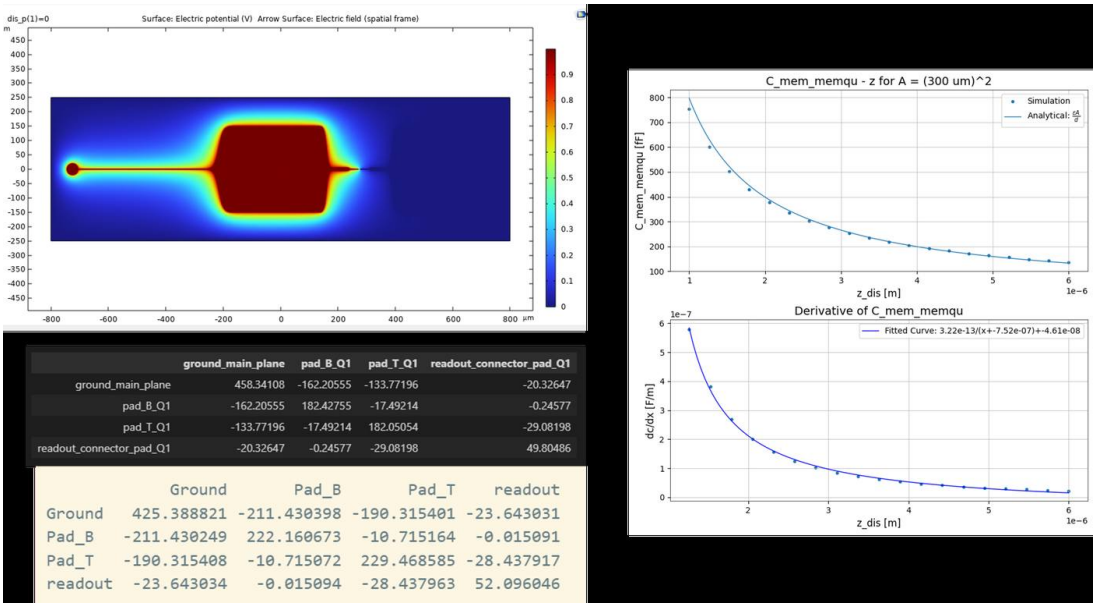

	ground_main_plane	pad_B_Q1	pad_T_Q1	readout_connector_pad_Q1
ground_main_plane	458.34108	-162.20555	-133.77196	-20.32647
pad_B_Q1	-162.20555	182.42755	-17.49214	-0.24577
pad_T_Q1	-133.77196	-17.49214	182.05054	-29.08198
readout_connector_pad_Q1	-20.32647	-0.24577	-29.08198	49.80486

	Ground	Pad_B	Pad_T	readout
Ground	425.388821	-211.430398	-190.315401	-23.643031
Pad_B	-211.430249	222.160673	-10.715164	-0.015091
Pad_T	-190.315408	-10.715072	229.468585	-28.437917
readout	-23.643034	-0.015094	-28.437963	52.096046

Figure B.8: Left: (top) the electric field distribution when a qubit pad is biased.(middle) The simulated capacitance matrix in ANSYS by Igor.(bottom) The simulated capacitance matrix in COMSOL. Right: The capacitance and gradient of capacitance of a simulated parallel plate capacitor and the theoretical one.

, where

$$\int_A \phi_z \, dA = \int_A \frac{sign(shell.w) shell.w^2}{max(shell.disp)^2} \, dA$$

.

Implementing integral and max in COMSOL requires the definition of operators and variables beforehand. We assign the expression

Effective mass

```
epsilon0_const*intop2(shell.w/maxop2(shell.disp))/(dis^2)
```

in *Variables* under *component* interface. Intop2 and maxop2 are *nonlocaling coupling* operators that return the integral and maximum of a value for a surface. The details of the setup can be viewed in the following figure.B.9

We calculate the quality factor by dividing the kinetic energy to the bending energy and integral over the surface:

Quality factor

```
Bending energy
lshell.Eequ*(h0+h1)^3*((dtang(dtang(w2,x),x)+dtang(dtang(w2,y),y))
   ^2+2*(1-lshell.nuequ)*(dtang(dtang(w2,x),y)^2-dtang(dtang(w2,x),x)*
   dtang(dtang(w2,y),y)))/(12*(1-lshell.nuequ^2))
kinedtic energy
(h0+h1)*lshell.rho*lshell.omega^2*lshell.disp^2
```

Note that there are multiple numerical methods to calculate $\frac{dC}{dx}$, as shown in Fig.B.9. Integration normalizes the displacement for $C1$, while C1_int normalizes the movement to the

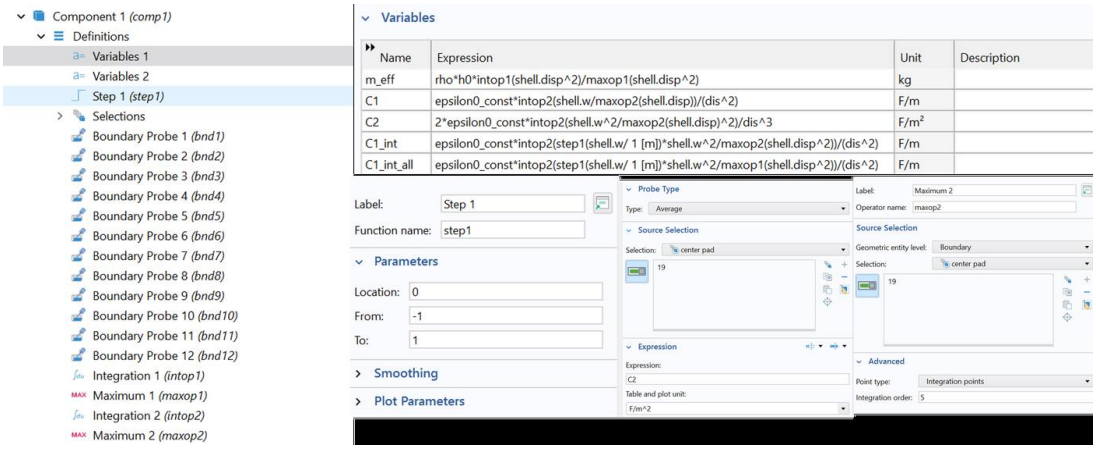

Figure B.9: Setup to calculate the dc/dx and effective mass.

square of the displacement. C1_int_all normalizes the movement to the global maximum of the membrane displacement, which is usually equal to the maximum of the center pad.

We would use C1_int to capture the mode because normalization should be related to the energy, which is the square of the displacement.

B.2.5 Bulking analysis

To rule out devices that are unstable and uncoolable, buckling analysis and thermal analysis calculate the mechanical stability and thermal conduction of the device. The setup can be summarized in the table below:

material1	Si_3N_4(E = 250 GPa, $\rho = 3200$ kg/m^3, $\nu = 0.23$, prestressed force = 0.9GPa $\cdot$ 50 nm)
geometry	membrane
physics	shell and heat conduction in shell
mesh	triangular + mapped
study	stationary + time dependent

Table B.5: Setup for buckling and membrane thermal simulation

Reliably simulating buckling remains a challenge, especially on hierarchical membranes [21]. COMSOL provides methods including buckling analysis and principal stress analysis, but none of them guaranties buckling-free conditions. Linear buckling analysis estimates the critical load factor and the corresponding buckling mode. A low critical load factor indicates that the mode is susceptible to small perturbations of compressive stress. However, the result is only valid for an idealized pre-buckling equilibrium state. The principal stress analysis reveals the stress distribution in the corresponding principal direction. A region with strong compressive stress implies a high possibility of buckling. However, the critical buckling stress cannot be inferred from the local stress alone.

To obtain results that can be compared to [21], we use principal stress analysis to locate the region with strongly compressive stress. The figure.B.10 indicates that the region with compressive stress is negative in both the simulation and the publication. The simulation agrees with [21], evidenced by the similar shape and position of the buckling region on the arm that does not connect to the frame. The mismatch of the buckling region on the arm that connects to the frame is due to the difference in width of the arm.

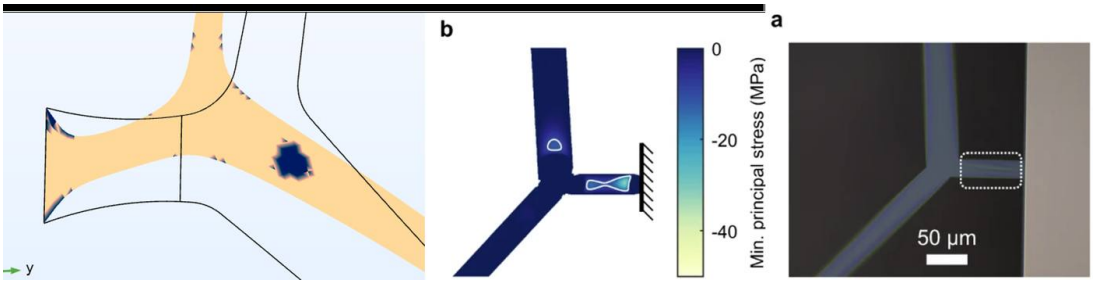

Figure B.10: Left: the buckling of the wheel membrane in COMSOL. Middle:in publication. Right: under a microscope. Those images are extracted from [21]

A major challenge in thermal simulation is to recreate the boundary conditions and the heat load of the actual device. Although COMSOL provides several heat-transfer interfaces, the availability of tools does not, by itself, ensure that the model represents the experimental system. Heat transfer in the shell analysis calculates the heat field of a 3D device with one dimension ignored. Time dependent simulation estimates the change of temperature. Faster transient temperature changes may indicate good thermal conductivity in the geometry. However, the thickness and cross-section of the membrane, convection conditions, and material oxidation can also significantly affect heat transfer. In addition, thermal contact resistance, convection, radiation, prescribed temperature, and all other factors change the transient response to temperature. A valid result relies on the precision with which the experimental conditions are represented in the simulation. Although we have methods to simulate the thermal conduction of the membrane, the lack of refrigeration operational conditions impedes the realistic simulation. More effort is required in defining the boundary conditions such as the thermal resistance of the fridge plate and the power of the heat source.

B.3 Optimization methods

To promote coupling to a greater extent, optimization of membrane mechanical properties, qubit frequency, and bonding distance is required, following the coupling formula. Optimization here indicates an iterative process to discover a set of parameters that defines geometry for higher coupling while considering buckling and thermal effects. COMSOl prepares two optimization methods: parameter sweeping and bayesian optimization. Parameter sweeping runs simulations with parameters from a pre-defined parameter list and generates a database. Analysis of the highest coupling candidate among the database reveals the sub-optimal design. However, the computational resources required for larger search spaces scale exponentially with the number of optimized parameters. To perform simulations efficiently, bayesian optimization is used. It predicts the highest coupling candidate, records the prediction and result error, and self-updates the gaussian distribution prior for the next prediction. Without simulating the less optimal candidate, hundreds of iterations could identify a sub-optimal design. Optimization is limited by the quality of the optimal candidate prediction. A High quality data set is required for reliable predictions.

Each session in the following orients around the challenges in optimization setup and how they are overcome. For parameter sweeping optimization, a geometry that is well defined on different geometry parameters is the hardest one to build. We used absolute parameter definitions to maintain the geometry definition. For bayesian optimization, building a mesh that avoids numerical issues with the geometry variation is the major challenge. We use a distributed mesh

and limit the search window to solve it.

B.3.1 Sweeping of parameters

The sweep of parameters can be defined in *the parametric sweep* under *the study* interface. In every simulation cycle, COMSOL regenerates geometry following the modeling steps with new parameters and completes the defined studies. The regeneration of geometry is sensitive to how the model is built. An error appears, particularly with some extreme geometry parameters, due to the absence of a geometry part number, non-singular solutions of constraints, and missing features to operate. Although COMSOL indicates the modeling steps that are problematic, resolving the error usually requires multiple changes in other modeling steps, which is not obvious. General practices like using parallel, coincident constraints in other CAD software like Onshape or SOLIDWORK greatly perturb the stability of geometry generation in COMSOL. It is not recommended to constrain sketches or components geometrically without complete consideration of the uniqueness of constrained geometry at different parameters.

The safest modeling method for enabling stable sweeping of parameters is parametric absolute position modeling. This method defines the shape, position, and size of the membrane by parameters, excluding the use of geometric constraints. Parameterization allows the reconstruction to be a purely mathematical recalculation without ambiguity. Thus, for the extreme geometry, there will be no geometry problems. To enable parameterization of a complex geometry, smaller blocks are modeled as components. The geometry parameters for assembling components are decoupled from the parameters that define the geometry, reducing the difficulties on modeling. However, the exact equation for every geometric position and shape remains a tedious calculation task for parametric modeling. For complex geometry defined by geometric constraints, converting the model to a parametric representation is a challenge.

The hierarchical rules facilitate parametric modeling through rotational symmetry. Only one eighth of the membrane involves calculation. The detailed setup is shown in the figure.

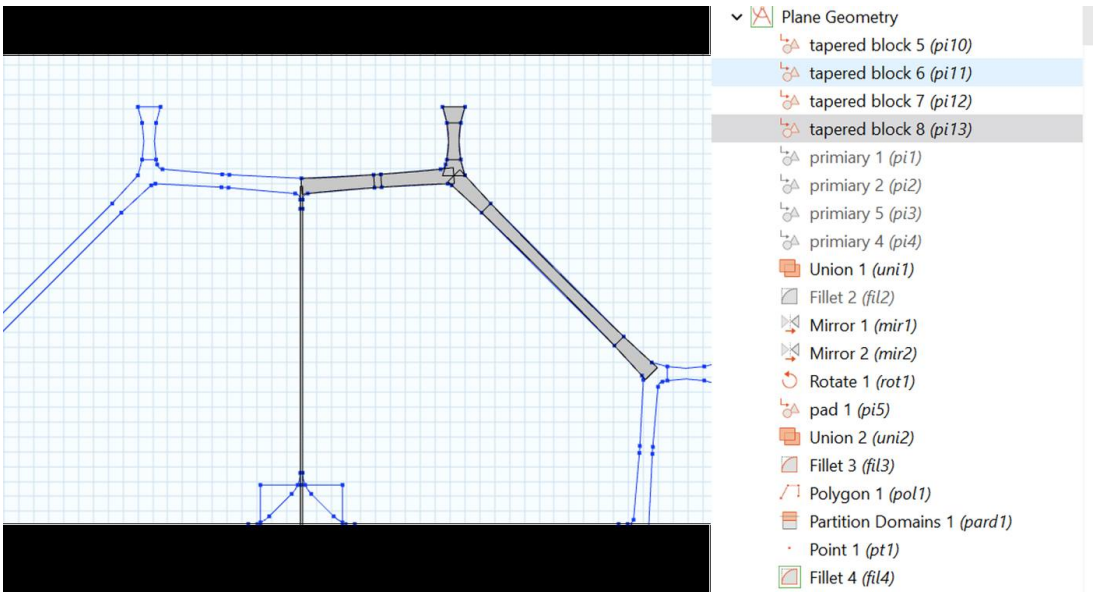

Figure B.11: Left: the one eighth of the wheel membrane. They are assemblied by blocks Right: The geometry interface in COMSOL.

The parameter sweeping results for the trampoline membrane are shown in fig.B.12. After

1185 samples in 5 sets of parameters, we were able to find a quality factor that exceeds 10^9. The simulation takes a day to complete.

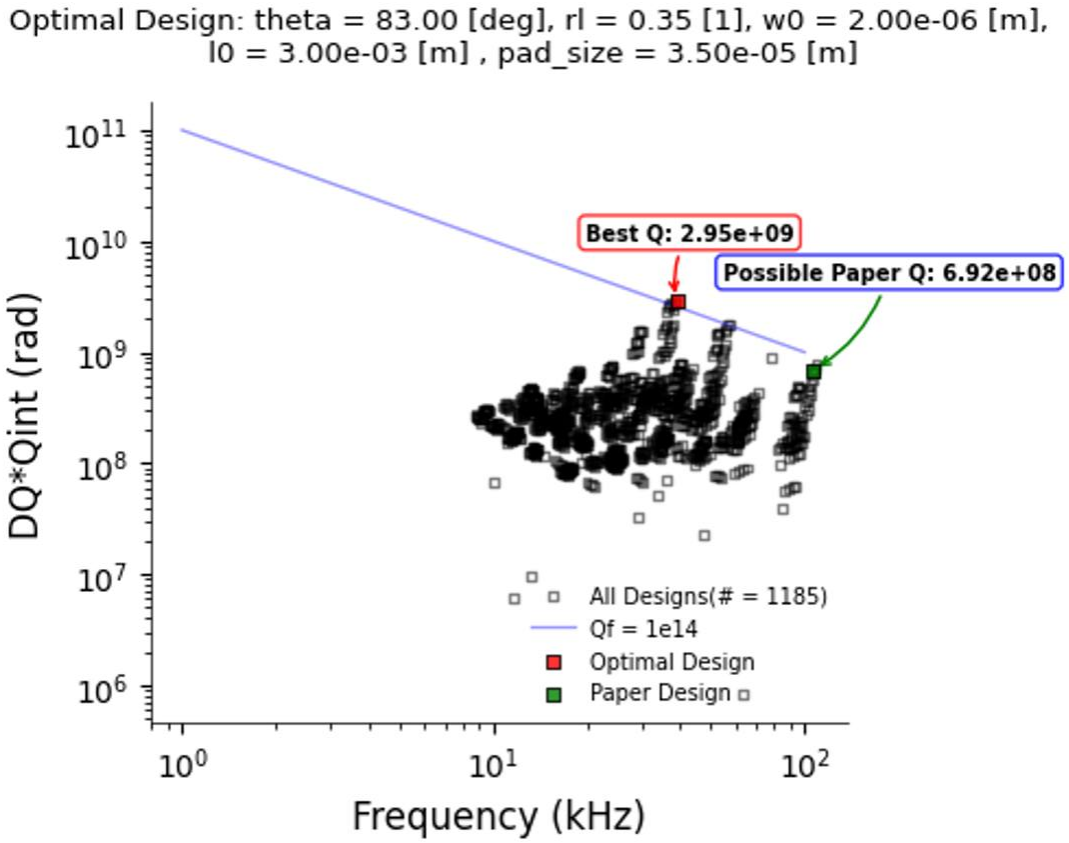

Figure B.12: Parameter sweeping result on trampoline membrane across: angle between tether θ, contraction ratio r_0, width of the first tetherw_0, length of the first tetherl_0, pad length size.

B.3.2 Bayesian optimization

Bayesian optimization is an exploration-exploitation balanced optimizer that consistently searches for the optimal solution and tests it. The original definition of bayesian optimization in COMSOL cannot accumulate knowledge over different rounds; therefore, we realize the same algorithm with the aid of codex. It takes the parameters and the value window for optimization, calling the COMSOL API to return an objective function. The objective function and the corresponding parameters together are mapped to a gaussian distribution. This distribution acts as a surrogate model to infer the next optimal point. With a sufficient number of data points to support the surrogate model, the ability to predict the optimal point emerges. Because the optimizer requires zero knowledge of the simulation conditions, it is named a black-box optimization method.

Although the optimizer is able to optimize many black box functions, reaching the optimal solution varies from one black box to another. The surrogate model and the optimization direction depend heavily on the objective function. An incorrect objective function will derail the optimization direction, resulting in an unreliable result.

The objective function we use is:

$$H = Qg = Q \cdot \frac{VC}{de}\sqrt{\frac{E_c\omega_q}{2m_{eff}\omega_m}} \tag{B.4}$$

The production of Qg encourages the system to discover geometries that have a higher quality factor without sacrificing the coupling strength. The value of the product is usually around 4 to 30.

The objective function can be wrong in two major ways. One is that the simulation is faulty and returns an objective function that does not reflect the current design. The simulator will overestimate the quality factor if the meshing causes a numerical error in curvature. Without changing the meshing conditions, the overestimation could occur during all the optimization steps. Although an increase in the objective value and a change in geometry are observed, the design could be even worse than the initial design.

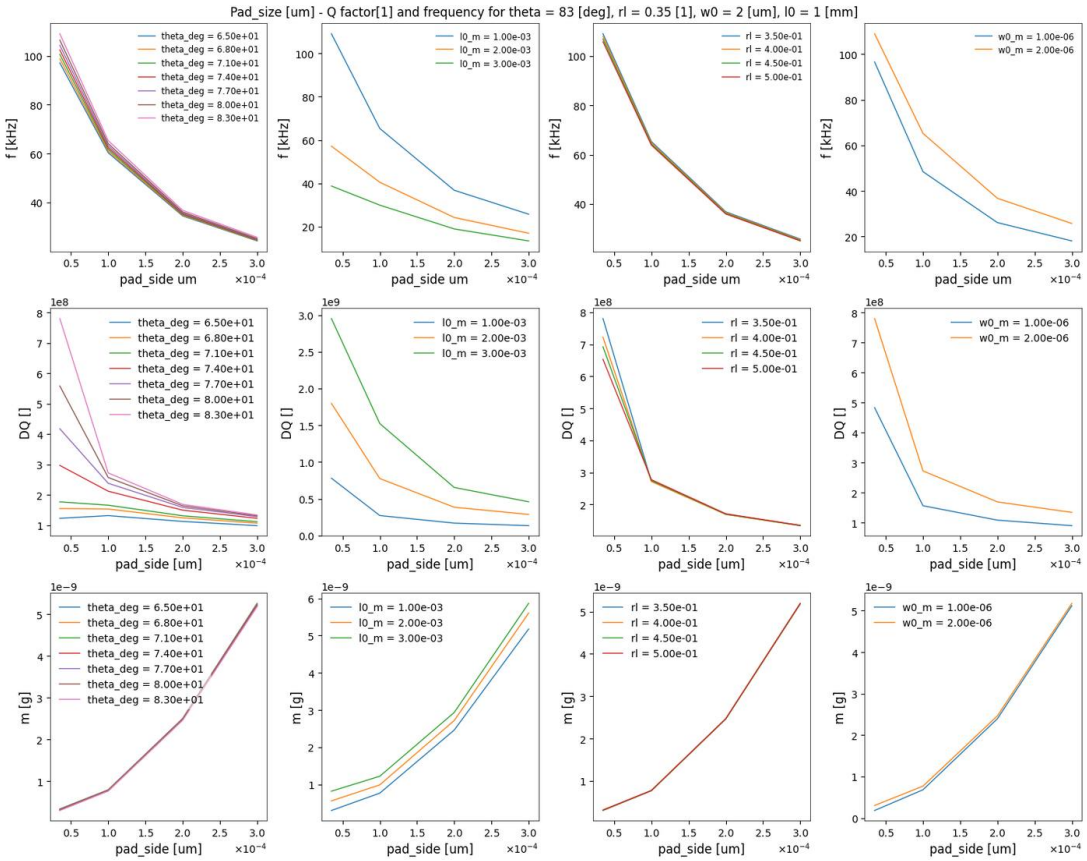

Figure B.13: Tendency plot of the parameter sweeping result shown in fig.B.12.

The other error is that the objective function itself poorly describes the optimization direction. Some of the geometry parameters, such as filet angle and thickness, do not relate to the objective value. The length of the tether at different levels requires a special ratio between each other to enhance the objective value. Simulators lose direction on the geometry parameters to optimize.

The simulation induced error can be detected by stability tests on the simulation. The test perturbs the meshing conditions and solver configurations to check the stability of the objective function value. For the purpose of checking the optimization direction, we examined

the optimized structure and compared the effective mass, frequency quality factor, and overall geometry to the original structure.

With the aim of selecting key parameters, an initial small scale of parameter sweeping is performed, and then we compute multiple optimizations to exclude some optimization parameters. We observe that the sensitivity of the parameter is related to the quality factor and frequency. The fig.B.13 shows this. We found that the angle and width of the filet of the membrane do not affect the quality factor and frequency. The width, ratio, angle, and pad size significantly change the system.

Appendix C

Simulation of other membrane

C.1 Parameters of the extreacted wheel membrane

Initial geometry of the wheel membrane		
Parameter	Description	Value
	Membrane	
-	Membrane geometry	wheel membrane
$r0$	Fillet length	2 μm and 50 μm
$w0$	First tether width	15 μm
$w1$	Second tether width	54 μm
w_b	Bridge tether width	84 μm
$l1$	First tether length	1.01 mm
$l2$	Second tether length	0.546 mm
$l3$	Third tether length	0.09 mm
A	Pad area	75 μm $\cdot$ 75 μm
θ	Angle	86.5^o

Table C.1: The geometry of the wheel membrane

Geometry of the wheel membrane before and after optimzation changed		
Parameter	Description	Value
	Membrane	
-	Membrane geometry	wheel membrane
$r0$	Fillet length	2 μm and 50 μm
$w0$	First tether width	15 μm
$w1$	Second tether width	/107.5 μm
$w2$	third width	/151.7 μm
w_b	Bridge tether width	/114.8 μm
$l0$	First tether length	**need to inspect**2/2.28 mm
$l1$	Second tether length	1.03 mm
$l2$	Third tether length	0.4782 mm
A	Pad area	400 μm $\cdot$ 400 μm
θ	Angle	86^o

Table C.2: The geometry of the wheel membrane

The device design extracted from [21] does not follow the membrane construction rules. The

lengths of the tethers at different stages do not share the same contraction ratio. The width does not meet the width requirement. We have written an email to the author to clarify these inconsistencies. It was stated that to avoid buckling and fabrication infeasibility, minor changes to the geometry were applied, including width and radius. The tethers are also tapered in shape.

To systematically study the membrane and enable parametric modeling, we approximate the deduction ratio of the tethers to be 0.45. The buckling free design is achieved by also introducing the tapered tether with a predefined geometry. We set the membrane length to be 2 mm, where the 2D string model gives the fundamental frequency as 71 kHz. This is the upper bound because the soft-clamping and center pad will increase the effective mass, thus decreasing the fundamental mode frequency. The length of the membrane $l0$ includes the contribution of the center pad; thus, it is larger than 2 mm.

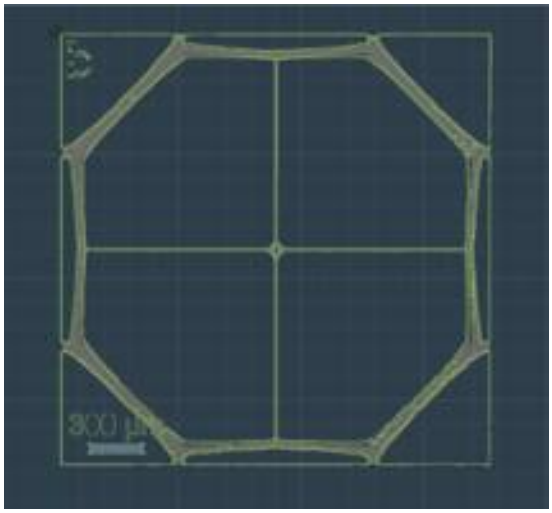

(a) The wheel membrane extracted from ref.[21] in CAD sketch. The geometry was resketched with dimension.

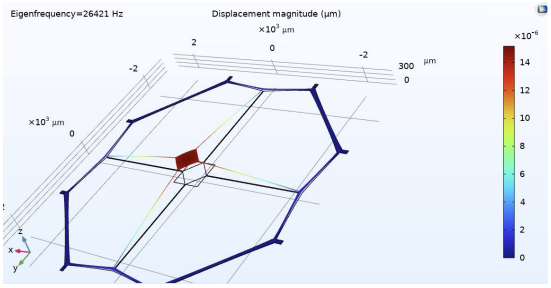

(b) The mode shape of fundamental mode of the edited membrane. The eigenfrequency differ slightly from the presented value 26.616 kHz, due to minor changed in fillet radius. The relative deflection value is presented with color gradient. The absolute displacement is not represented by the color.

Figure C.1

C.2 The diagonal membrane

We simulate a diagonal membrane because it has already been fabricated. The membrane is a hard-clamped diagonal silicon nitride membrane with a thickness of 100 nm. The geometry is illustrated in figure.C.2. The dimensions extracted using computer vision and remodeling are shown in table.C.3. The simulated frequency, quality factor, and effective mass of the fundamental mode are: 99.7 kHz, $4.7 \cdot 10^7$, and 67 ng.

C.3 The metallized diagonal membrane

In membrane metallization, we estimate the change in frequency, effective mass, and quality factor under different stress conditions. These changes lead to a change in the coupling strength at different temperatures. Metallization entails the stress condition of the membrane; therefore, we study the frequency changed by stress of a square membrane to calibrate the residual stress, shown in Figure.C.3. The influence of metallization on frequency, effective mass, and quality

Diagonal membrane geometry		
Parameter	Description	Value
	Membrane	
	Membrane geometry	diagonal membrane
	frequency	99.7 kHz
	quality factor	$4.7 \cdot 10^7$
	frame size	1983 μm
	membrane thickness	100 nm
	effective mass	67 ng
	fillet on frame	65 μm
	fillet on pad	200 μm
	first width	72.8 μm
	first tether length	0.972 mm
	pad area	$3.169 \cdot 10^5$ μm^2

Table C.3: Detailed geometry and mechanical properties of 100nm thick diagonal membrane. No.18 membrane from Antonius's collection in Degen's group.

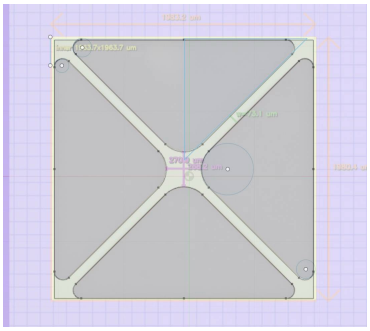

Figure C.2: The geometry overlook of the diagonal membrane with dimension on top.

factor on the diagonal membrane is shown in Figure.C.3 (A),(B) and (C).

Figure.C.3 (B) shows the frequency and effective mass change concerning the change in the thickness of the deposition on the 100 nm thick diagonal membrane. The stress we use is +250 MPa. The membrane mass increases from 67 ng to 103.8 ng, with deposition thicknesses ranging from 0 to 70 nm. The increment is 36.8 ng, which is similar to the value of 40.84 ng if we convert the added physical mass of Al to the effective mass, assuming the same effective to physical mass ratio $\frac{103.8}{713.9} = 0.145$. The frequency decreases from 96.7 to 84.5 kHz as a result of the increase in the effective mass.

Figure.C.3 (A) shows the variation of the spring constant ($m_{eff} \cdot \omega_m^2$) and the fluctuation of the zero point position ($\sqrt{\frac{\hbar}{2m_{eff}\omega_m}}$) with increasing membrane thickness. The zero point fluctuation distance decreases from 1.12 fm to 0.97 fm and the spring constant increases from 26.25 to 29.23 N/m. The increase in the spring constant is the result of the additional force contributed by the compressive stress of the aluminum layer.

Figure.C.3 (C) illustrates the change in the quality factor and the coupling correction factor based on the change in the thickness of the deposition. The correction factor, depicted in the dashed line, varies from 1 to 0.87. The original coupling constant, with a correction factor of 1, translates to 59.87% of the DSC threshold. The correction factor is normalized to the value of

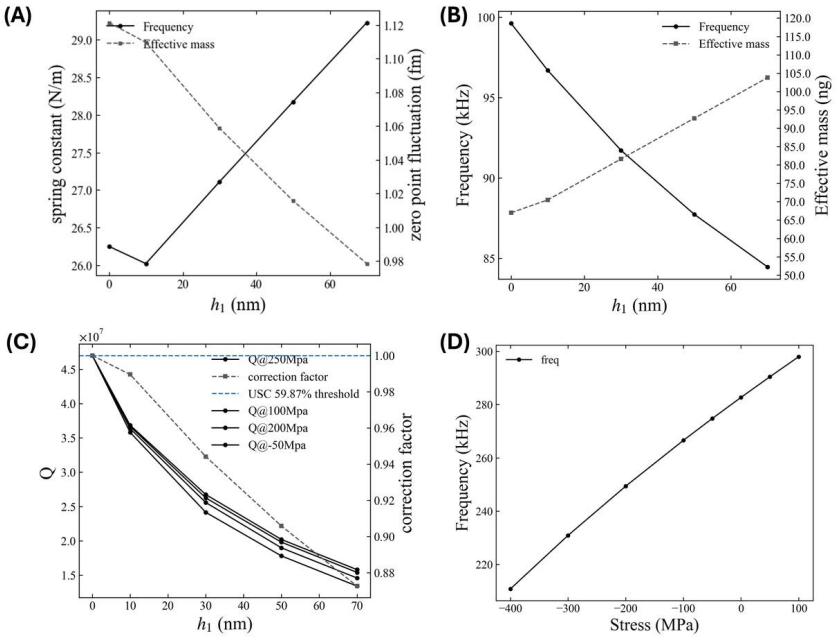

Figure C.3: metallized membrane plot for following parameters with the increase of the deposition thickness of the membrane (A) the effective spring constant and position zero point fluctuation of the membrane (B) the frequency and the effective mass (C) the quality factor and the correction factor for coupling strength of membrane without metalliztaion (D) the frequency - stress of Al plot.

the pure membrane and scaled according to $\sqrt{\frac{m_0\omega_0}{m_1\omega_1}}\frac{C_1'}{C_0'}$, representing the variation in the coupling constant due to metallization. For an Al layer of 30 nm, we obtain a correction factor of 0.94. The quality factor-thickness plot for stress conditions of 250 MPa, 200 MPa, 100 MPa, and -50 MPa is plotted as a solid line. The quality factor reduces by a factor of 3.5 from 4.7 $\cdot 10^7$ to 1.34 $\cdot 10^7$. Again, the meshing problem persists. The decrease factor should show a general trend of decrease, but the gradient could vary from the actual device.

Figure.C.3 (D) is the frequency-stress plot for a silicon nitride square membrane of 1 mm by 1 mm with a thickness of 100 nm. The membrane is also fabricated and ready for al deposition. The solid curve shows the linear relationship between the fundamental frequency and the deposition stress. Therefore, we can use frequency as a scale to read out the residual stress in the actual membrane, bridging the simulated stress conditions to the actual experimental value. Dedicated machines such as the Toho FLX-2320-S Thin Film Stress Measurement Systems measure the surface radius change and calculate the surface stress of the deposited layer. However, the availability of such machines is unknown.

The decrease in frequency can be understood using the formula $m_{eff}\omega_m^2 = k$. The deposition of Al increases the effective mass. Tensile stress in al increases the force of the tether, thus increasing the spring constant k. The mass growth exceeds the growth of the spring constant; therefore, the frequency decreases.

The decrease in the quality factor is related to the decrease in the dilution factor. The simulation presented here assumes that the intrinsic loss of the membrane is the same after deposition. Thus, the quality factor fully reflects the change in the dilution factor. The reason why the dilution factor decreased requires further investigation on the curvature and kinetic

energy distribution. Intuitively, the decrease in the frequency of the membrane means that the increase in tension does not match the increase in mass. The material needs to bend more to compensate.

Appendix D

Fridge vibration test

To check the vibration noise condition of the fridge, the vibration test is conducted using an inclination sensor(KAS091), fixed at two angles on the cold base. The test result does not fully reflect the vibration on stage because the inclination sensor has a vibration damping system inside. The objective is to qualitatively inspect the noise distribution at kHz for further investigation. All the data was collected within 2 hours for one fridge only. to assure the actual spectrum, repetitive measurements at different times and different fridges are required.

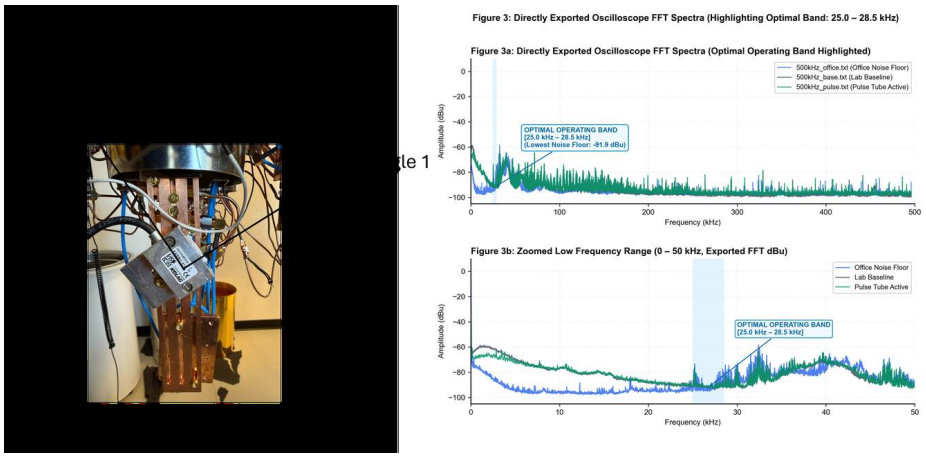

Figure D.1: Left: the directional inclination sensor on top of the fridge. Angle 1 and angle 2 indicates the sensing direction.Right: the PSD for membrane in angle 1 (base,pulse on) and angle 2(office) and the details of PSD at 0 - 60 kHz. The black curve represents the baseline. The green line is the PSD when the pulse tube is on of the fridge, overlaping with the baseline. The blue line is the base line in angle 2.

The vibration has a directional distribution. Figure.D.1 shows the schematic for the sensor and their spectrum for pump on, baseline at angle 1, and baseline at angle 2(office). At 0 - 20 kHz, vibration at angle 2 experiences significantly less noise than at angle one. After 20 kHz, the noise curve coincides for the two angles. The other difference is not observable.

The fridge seems to be immune to environmental disturbances. We perform the following actions around the fridge: walking heavily, touching the fridge, and slapping the door of the lab. The low frequency disturbance can be seen from the shape of the wave on the left plot. We perform a Fourier transform on the recorded frequency and capture the noise at 15 Hz for all three disturbances. However, for the high frequency difference, it is not distinguishable. However, this does not imply that there is no noise injected in the kHz bandwidth. The sensor intrinsic sensitivity to kHz noise could be weak.

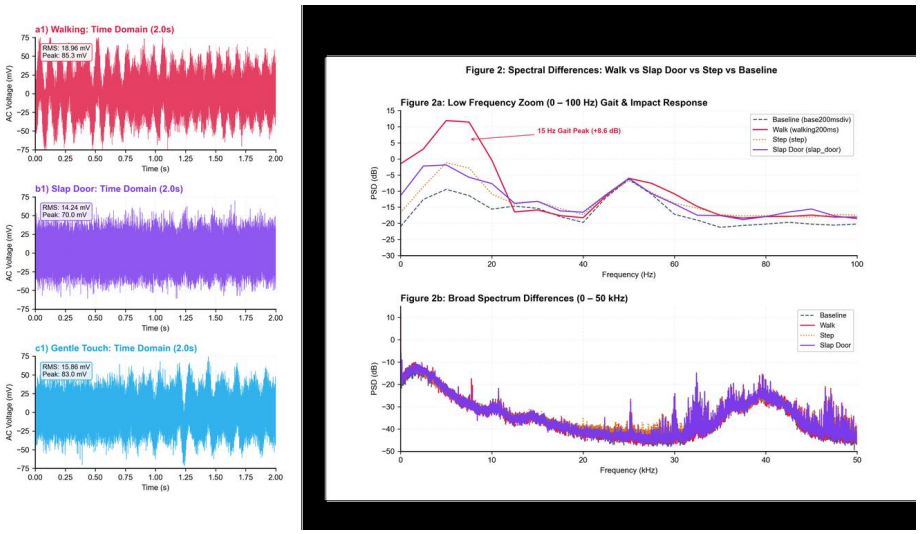

Figure D.2: Left: the signal captured by the sensor of three vibration disturbance: walking, slapping the door and touch. Right: the PSD of the signal on the left at different bandwidth. At low frequency we can observe the noise increase. For 1 - 60 kHz region, no significant resonance peak are observed.

Appendix E

Declaration for the use of Artificial Intelligence

I used AI tools(GPT sol 5.6) during the preparation of this thesis. Chapter 3 was developed through an iterative process of drafting and refinement between the AI tool and myself. Parts of the abstract and conclusion were generated by AI based on the content I wrote. For the remaining sections, AI was used only for language editing, primarily to correct grammar, without generating or altering the underlying scientific content.

AI is also used to review the consistency of the results.